Initial Energy Density in Heavy Ion Collisions from a Color Neutral Three-Dimensional Color Glass Condensate Model of QCD

A THESIS
SUBMITTED TO THE FACULTY OF THE GRADUATE SCHOOL
OF THE UNIVERSITY OF MINNESOTA
BY

Şener Özönder

IN PARTIAL FULFILLMENT OF THE REQUIREMENTS
FOR THE DEGREE OF
Doctor of Philosophy

Joseph I. Kapusta, Advisor

August, 2013

Acknowledgements

First, I would like to thank my advisor Joseph Kapusta for his continuous guidance and support. I also thank Rainer J. Fries, my collaborator, for the discussions we had at various stages of the work presented in this thesis. I am thankful to my friends and colleagues Evan Frodermann, Emir Gümrükçüoğlu, Todd Springer, Raju Venugopalan, Meng-Ru Wu and Clint Young for the good times we passed together as well as the scientific discussions we had. I thank the committee members Dan Cronin-Hennessy, Alex Kamenev and Yong-Zhong Qian for the good questions they asked. I also thank my wife Zuleyha and my son Ahmed Fehim, maybe future's physicist, for their understanding.

This work has been supported by the School of Physics and Astronomy at the University of Minnesota, the US Department of Energy (DOE) under Grant No. DE-FG02-87ER40328, and under the Hoff-Lu Fellowship.

Finally, all the praises and thanks be to Allah, who is the ultimate cause.

Dedication

Dedicated to my father Mehmet, my mother Sabahat and my grandmother Münibe.

Abstract

In the ultrarelativistic heavy-ion collisions at the Relativistic Heavy Ion Collider (RHIC), Brookhaven National Lab (BNL) and the Large Hadron Collider (LHC), Conseil Européen pour la Recherche Nucléaire (CERN), hot, dense and strongly interacting Quark Gluon Plasma has been created. After the Quark Gluon Plasma reaches local thermal equilibrium, the fireball expands rapidly. Relativistic hydrodynamics successfully captures this evolution given the initial energy and initial entropy densities, along with the equation of state. This is followed by freeze-out of the plasma into hadrons, which are finally recorded at the detectors. The final multiplicity of the detected particles as well as their distribution in transverse momentum and rapidity are determined by the initial conditions of the hydrodynamic evolution of the Quark Gluon Plasma.

In this thesis, the initial energy density of heavy-ion collisions is calculated in the framework of an effective model based on Quantum Chromodynamics. An overview of heavy ion collisions and Quark Gluon Plasma is given first. Then, the three-dimensional, color neutral McLerran-Venugopalan model is introduced and its parameters are fixed from the data on gluon distribution functions. Finally, we apply this model to Au-Au (at RHIC) and Pb-Pb (at LHC) collisions to calculate the initial energy density. The most important result of the work presented here is calculation of the rapidity profile of the initial energy density. Finally we compare our results on the energy density profile with that is used in hydrodynamic simulations.

Contents

List of Tables

List of Figures

List of Notations

In this section we provide a selection of notations and conventions that are used in the main text.

$$y = \frac{1}{2}\ln\left(\frac{E+p_z}{E-p_z}\right) \text{ (momentum rapidity).} \tag{1}$$

$$\eta_{\rm s} = \frac{1}{2}\ln\left(\frac{t+z}{t-z}\right) \text{ (space-time rapidity).} \tag{2}$$

$$x^+ = \frac{(t+z)}{\sqrt{2}} = \frac{\tau(\cosh\eta+\sinh\eta)}{\sqrt{2}},\ \ x^- = \frac{(t-z)}{\sqrt{2}} = \frac{\tau(\cosh\eta-\sinh\eta)}{\sqrt{2}}. \tag{3}$$

$$t = (x^+ + x^-)/\sqrt{2},\ \ z = (x^+ - x^-)/\sqrt{2}. \tag{4}$$

$$\tau = \sqrt{t^2-z^2} = \sqrt{2x^+x^-}. \tag{5}$$

$$\eta_{\rm s} = \frac{1}{2}\ln\frac{t+z}{t-z} = \frac{1}{2}\ln\frac{x^+}{x^-}. \tag{6}$$

$$t = \tau\cosh\eta,\ \ z = \tau\sinh\eta. \tag{7}$$

The metric in (t,x,y,z) coordinates

$$g_{\mu\nu} = \begin{pmatrix} 1 & 0 & 0 & 0 \\ 0 & -1 & 0 & 0 \\ 0 & 0 & -1 & 0 \\ 0 & 0 & 0 & -1 \end{pmatrix}. \tag{8}$$

The metric in $(+,-,\boldsymbol{x}_\perp)$ coordinates

$$g_{\mu\nu} = \begin{pmatrix} 0 & 1 & 0 & 0 \\ 1 & 0 & 0 & 0 \\ 0 & 0 & -1 & 0 \\ 0 & 0 & 0 & -1 \end{pmatrix}. \tag{9}$$

The metric in $(\tau, \eta, \boldsymbol{x}_\perp)$ coordinates

$$g_{\mu\nu} = \begin{pmatrix} 1 & 0 & 0 & 0 \\ 0 & -\tau^2 & 0 & 0 \\ 0 & 0 & -1 & 0 \\ 0 & 0 & 0 & -1 \end{pmatrix}, \quad g^{\mu\nu} = \begin{pmatrix} 1 & 0 & 0 & 0 \\ 0 & -1/\tau^2 & 0 & 0 \\ 0 & 0 & -1 & 0 \\ 0 & 0 & 0 & -1 \end{pmatrix}. \tag{10}$$

Other relations between different coordinate systems:

$$(d\tau)^2 = (dt)^2 - (dz)^2 = 2dx^+dx^-. \tag{11}$$

$$\begin{aligned} (ds)^2 &= (dt)^2 - (dz)^2 - (dx)^2 - (dy)^2 && (12) \\ &= 2dx^+dx^- - (dx)^2 - (dy)^2. && (13) \end{aligned}$$

$$x_+ = x^-, \;\; x_- = x^+. \tag{14}$$

$$\frac{\partial x^-}{\partial \eta} = -\frac{t-z}{\sqrt{2}} = -x^-, \;\; \frac{\partial x^+}{\partial \eta} = \frac{z+t}{\sqrt{2}} = x^+. \tag{15}$$

$$\frac{\partial \tau}{\partial x^+} = \frac{x^-}{\tau}, \;\; \frac{\partial \tau}{\partial x^-} = \frac{x^+}{\tau}, \;\; \frac{\partial \eta}{\partial x^+} = \frac{1}{2x^+}, \;\; \frac{\partial \eta}{\partial x^-} = \frac{-1}{2x^-}. \tag{16}$$

$$\begin{aligned} \partial^+ = \partial_- &= \frac{\partial}{\partial x_+} = \frac{\partial}{\partial x^-} = \frac{\partial \tau}{\partial x^-}\frac{\partial}{\partial \tau} + \frac{\partial \eta}{\partial x^-}\frac{\partial}{\partial \eta} && (17) \\ &= \frac{x^+}{\tau}\frac{\partial}{\partial \tau} - \frac{1}{2x^-}\frac{\partial}{\partial \eta}. && (18) \end{aligned}$$

$$\begin{aligned} \partial^- = \partial_+ &= \frac{\partial}{\partial x_-} = \frac{\partial}{\partial x^+} = \frac{\partial \tau}{\partial x^-}\frac{\partial}{\partial \tau} + \frac{\partial \eta}{\partial x^-}\frac{\partial}{\partial \eta} && (19) \\ &= \frac{x^-}{\tau}\frac{\partial}{\partial \tau} + \frac{1}{2x^+}\frac{\partial}{\partial \eta}. && (20) \end{aligned}$$

Covariant transformation

$$X'_a = \frac{\partial x^b}{\partial x'^a} X_b. \tag{21}$$

Contravariant transformation

$$X'^a = \frac{\partial x'^a}{\partial x^b} X^b. \tag{22}$$

Relations that are used in Appendix A

$$\lim_{\epsilon\to 0}\int_{-\epsilon}^{\epsilon} dx^+\theta(x^+) = 0. \tag{23}$$

$$\lim_{\epsilon\to 0}\int_{-\epsilon}^{\epsilon} dx^+ \underbrace{\frac{\partial}{\partial x^+}\theta(x^+)}_{\delta(x^+)} = 1. \tag{24}$$

$$\frac{\partial}{\partial x}\theta(-x) = -\delta(x). \tag{25}$$

The field strength is given as (Eq. (2.3) in [6] and Eq. (15.33) in [7])

$$F_{\mu\nu} = \partial_\mu A_\nu - \partial_\nu A_\mu - ig[A_\mu, A_\nu], \tag{26}$$

where $A_\mu = A^a_\mu t^a$ and t^a's are Gell-Mann matrices of $SU(3)$.

If the fields are not operators, we have

$$F^a_{\mu\nu}t^a = \partial_\mu A^a_\nu t^a - \partial_\nu A^a_\mu t^a - igA^b_\mu A^c_\nu [t^b, t^c]. \tag{27}$$

From Eq. (15.34) in [7]

$$[t^b, t^c] = if^{bca}t^a = if^{abc}t^a, \tag{28}$$

where $f^{bca} = f^{abc}$ due to the antisymmetric nature of the structure constant. Also,

$$f^{abc}f^{abc} = N_{\rm c}(N_{\rm c}^2 - 1). \tag{29}$$

Eq. (27) can also be written as (see Eq. (15.35) in [7])

$$F^a_{\mu\nu} = \partial_\mu A^a_\nu - \partial_\nu A^a_\mu + gf^{abc}A^b_\mu A^c_\nu. \tag{30}$$

From Eq. (15.38) in [7]

$$\mathcal{L} = -\frac{1}{2}{\rm Tr}[F^{\mu\nu}F_{\mu\nu}] = -\frac{1}{2}{\rm Tr}[F^a_{\mu\nu}t^a F^{b\mu\nu}t^b] \tag{31}$$

$$= -\frac{1}{2}F^a_{\mu\nu}F^{b\mu\nu}\underbrace{{\rm Tr}[t^a t^b]}_{\delta^{ab}/2} = -\frac{1}{4}F^a_{\mu\nu}F^{a\mu\nu}. \tag{32}$$

The covariant derivative is given by

$$D_\mu = \partial_\mu - igA_\mu = \partial_\mu - igA^a_\mu t^a. \tag{33}$$

The equation of motion can be written as

$$\mathcal{D}_\mu F^{\mu\nu} = \partial_\mu F^{\mu\nu} - ig[A_\mu, F^{\mu\nu}], \tag{34}$$

where $\mathcal{D}_\mu \equiv [D_\mu, F^{\mu\nu}]$.

Chapter 1

Introduction

The theory that describes the interactions of quarks and gluons, the building blocks of hadrons (proton, neutron, pion etc.), is called the Quantum Chromodynamics (QCD). The quantum character of the theory is due to quarks obeying wave mechanics. In addition, they are accompanied by gluons as well as virtual quark-antiquark pairs that are created by the quantum fluctuations of the ground state - vacuum. The charge that couples quarks to gluons and also gluons among themselves comes in a triple form as red, green and blue. Chromo (Greek, color) is an allusion to the feature of the primary colors (red, green, blue) that they become colorless (white) when combined. The dynamical degrees of freedom of QCD are quarks and gluons; however, individual quarks and gluons are not detected. Only hadrons, which are color singlets, reach the detectors as final particles.

Charge anti-screening is one of the most important features of QCD. For comparison, in Quantum Electrodynamics (QED) electric charge is screened by electron-positron pairs that fluctuate in the vacuum. When the electric charge is probed with increasing resolution, the effect of screening decreases and the amount of effective electric charge probed increases. Accordingly, the coupling constant $\alpha_{\mathrm{EM}} = e^2/4\pi$ increases, e being the electric charge. In QCD, the situation is the opposite. First of all, the force mediators in strong interactions (QCD), gluons, carry color charge whereas photons, the mediators of electromagnetic force, are chargeless. When a quark or gluon is probed with increasing resolution, more energetic fluctuations of the vacuum will be resolved as in QED. In QCD, however, the screening of color charge due to quark-antiquark pairs is overcome

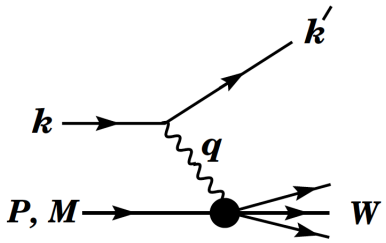

Figure 1.1: Deep inelastic scattering of a lepton with four-momentum $k' = (E', \boldsymbol{k'})$ with a nucleon with three-momentum $\boldsymbol{P}$ and mass M. The black blob represents the structure function (or the PDF) of the nucleon. The process is "deep" since the inner structure of the nucleon is resolved when $Q^2 \equiv -q^2 \gg M^2$. Also, the process is "inelastic" due to $W^2 \gg M^2$ where $W^2 = (P+q)^2$ is the invariant mass (or missing mass) of the produced particles and P is the four-momentum of the nucleon. In the text, proton and nucleon are used interchangeably; however, neutrons also participate in deep inelastic scattering. (Figure from [1])

by the anti-screening of gluons, hence the effective color charge g and the strength of the strong interactions[1], characterized by the coupling constant $\alpha_s = g^2/4\pi$, becomes weak at high resolution. This is called asymptotic freedom since quarks and gluons decouple and become free, noninteracting particles at asymptotically high energies. Quarks and gluons in hadrons behave almost freely when they are hit by an energetic particle during a collision, or at high temperatures/densities. The latter is realized in Quark Gluon Plasma (QGP).

Before we delve into the evolution of the strong coupling constant and the parton distribution functions, let us recall the variables in Deep Inelastic Scattering (DIS). The language of DIS permeates the entire field of small-x physics (QCD at high energy). Below, we will follow the definitions in the Particle Data Group [1].

Figure 1.1 shows a deep inelastic scattering process such as e+p or ν+p: a lepton (electron or neutrino) with four-momentum[2] $k = (E, \boldsymbol{k})$ is scattered from a nucleon with four-momentum P and mass M. The center-of-mass (CM) energy squared (or invariant energy squared) is given by $s = (k+P)^2$. The exchanged particle (photon, $W^\pm$ or Z) transfers four-momentum $q = k - k'$ to the nucleon, where $k' = (E', \boldsymbol{k'})$ is

[1] The interactions that QCD model is called strong interaction regardless of whether the coupling constant is weak or strong.

[2] Four-momentum is shown with normal font series as k and three-dimensional spatial momentum is shown in bold as $\boldsymbol{k}$.

the four-momentum of the scattered lepton. The internal structure of the nucleon is probed by the exchanged particle with the resolution

$$\begin{aligned} Q^2 \equiv -q^2 &= 2(EE' - \boldsymbol{k}\cdot\boldsymbol{k'}) - m_\ell^2 - m_{\ell'}^2 \\ &\approx 4EE'\sin^2(\theta/2), \end{aligned} \tag{1.1}$$

where m_ℓ ($m_{\ell'}$) is the mass of the initial (final) lepton. Here θ is the angle between the scattered lepton and the lepton beam direction. The scattering is called "deep" since the inner structure of the nucleon is probed, i.e., $Q^2 \gg M^2$. The exchanged particle strikes one of the constituents of the nucleon. The Bjorken-x variable is defined as

$$x_{\rm Bj} \equiv \frac{Q^2}{2q\cdot P} = \frac{Q^2}{2M(E-E')}, \tag{1.2}$$

where $0 < x_{\rm Bj} < 1$. In the leading order perturbative QCD (pQCD), $x_{\rm Bj}$ defined in Eq. (1.2) is equivalent to the longitudinal momentum fraction x of the struct constituent. Hence, the momentum of the struct constituent can be defined as $p \equiv x_{\rm Bj}P$ to leading order[3]. For a given Q^2 constituents with smaller values of $x_{\rm Bj}$ are accessed with increasing collision energy s since

$$x \sim \frac{Q^2}{s}. \tag{1.3}$$

This is why small-x physics is referred to also as the high-energy limit of QCD.

The momentum fraction x and resolution scale Q^2 will be used extensively in the following. We shall first discuss the evolution of $\alpha_{\rm s}$ with Q^2 and then we will investigate the parton distribution functions (PDFs), which depend on x and Q^2.

The evolution of the coupling constant with momentum (or energy) scale Q is given in Fig. 1.2 [1]. It is common practice to report the strong coupling constant at the scales of τ-lepton and Z-boson masses:

$$\alpha_{\rm s}(M_\tau = 1.78\,{\rm GeV}) \simeq 0.33, \tag{1.4}$$

$$\alpha_{\rm s}(M_Z = 91.2\ {\rm GeV}) \simeq 0.12. \tag{1.5}$$

[3] The equivalence between the momentum fraction x and $x_{\rm Bj}$ holds only at the leading order, i.e., in the case when radiative corrections are not included. In the next-to-leading order, the constituent radiates a gluon and lose some of its original momentum before it gets struck by the photon, hence $x \neq x_{\rm Bj}$. In other words, the definition of $x_{\rm Bj}$ in Eq. (1.2) holds in either case, but $x_{\rm Bj}$ can only be interpreted as the longitudinal momentum fraction of the struck constituent in the leading order pQCD. Also, the definition of x (without any subscript) as the momentum fraction holds in either case.

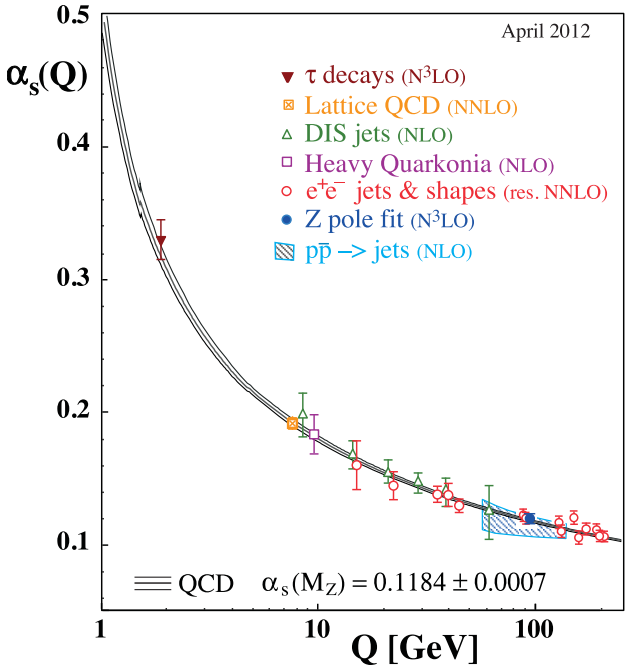

Figure 1.2: The strong coupling constant α_s at different momentum scales Q. In the DIS picture, this momentum scale corresponds to the momentum transferred by the exchanged particle (see Fig. 1.1). With increasing momentum, the interaction becomes weaker, hence perturbative techniques work better. In nucleus-nucleus collisions, the gluon density (color charge density) of a large nucleus sets another momentum scale in addition to Q^2. At this scale, one expects α_s to be weak at not so large energies, but still $Q^2 \gg \Lambda_{\rm QCD}$. This physics is not captured in this plot. (Figure from [1])

In an $e+p$ DIS process, the momentum transferred from an electron to the nucleon sets the momentum scale Q that $\alpha_s(Q)$ should be calculated at. Perturbative QCD is well-behaved only if the coupling constant is weak $\alpha_s \ll 1$. This condition is realized in the ultraviolet, i.e., at high energies. In the infrared sector of the theory ($\alpha_s \gtrsim 1$), the calculations based on pQCD become unreliable. Besides the energy scale, α_s depends also on the number of active quark flavors, renormalization scale and order in the perturbative calculations ((Next-to)^n-Leading-Order) [8]. The divergent behavior of α_s in the infrared can be seen at the one-loop (Leading Order-LO) calculation in the minimal substraction ($\overline{\rm MS}$) renormalization scheme:

$$\alpha_s(Q^2) = \frac{1}{\beta_0 \ln(Q^2/\Lambda^2_{\rm QCD})}, \tag{1.6}$$

where $\beta_0 = (33 - 2N_f)/12\pi$ and N_f is the number of active quarks at the scale Q^2. The $\Lambda_{\rm QCD}$ can be interpreted as the energy scale at which perturbation theory breaks down and the perturbative result for $\alpha_{\rm s}$ given in Eq. (1.6) diverges to infinity. By solving Eq. (1.6) for $\Lambda^2_{\rm QCD}$, one finds

$$\Lambda^2_{\rm QCD} = \frac{Q^2}{{\rm e}^{1/(\beta_0 \alpha_{\rm s}(Q^2))}}. \tag{1.7}$$

At $Q = M_\tau = 1.78$ GeV and $N_f = 3$, one finds $\Lambda_{\rm QCD} \approx 200$ MeV, which corresponds to the size of a nucleon ~ 1 fm. In contrast to the situation in DIS where one of the constituents of the nucleon is knocked out by a high momentum transfer $Q^2 \gg \Lambda^2_{\rm QCD}$, the typical momentum transfer between the constituents within a nucleon is soft ($\lesssim \Lambda_{\rm QCD}$) and the physics is completely nonperturbative. Despite the efforts spent on nonperturbative solutions such as instantons, QCD is not able describe the structure of a nucleon starting from gluons and quarks. Is this the end of the story? Not quite. Although the soft physics (nonperturbative phenomena) goes hand and hand with the strong coupling, in the case of a nucleus in heavy ion collisions, it may be possible to use weak coupling techniques (perturbation theory and Feynman diagrams) to describe the wave-function of a nucleus, which is a nonperturbative problem. This is the starting point of the saturation physics and the saturation scale $Q_{\rm s} \gg \Lambda_{\rm QCD}$. The new scale that emerges in the case of the nucleus is related to the density of the color charge in the nucleus. The density itself scales with the size of the nucleus. To emphasize, although the underlying physics of the nuclear wave-functions is still of strong interactions, we will show how the saturation scale emerges and $\alpha_{\rm s}$ becomes weak at that scale.

The coupling constant of strong interactions is not the only quantity that changes with the energy scale; the wave-function of a nucleon (and nucleus) also depends on the energy scale at which it is probed. The wave function of a proton is comprised of three valence quarks (uud) and gluons, and these are accompanied by the sea quarks/antiquarks and other gluons that arise from vacuum fluctuations. The wave-function becomes more and more dominated by the sea quarks and gluons at higher energies. Regardless of whether they are valence or sea, quarks/antiquarks and gluons are collectively called partons. The total number of partons grows with increasing beam energy. The momentum fraction x of the parton carrying momentum p in a nucleon with momentum P is given by $x = p/P$. The PDF of a nucleon/nucleus depends on the

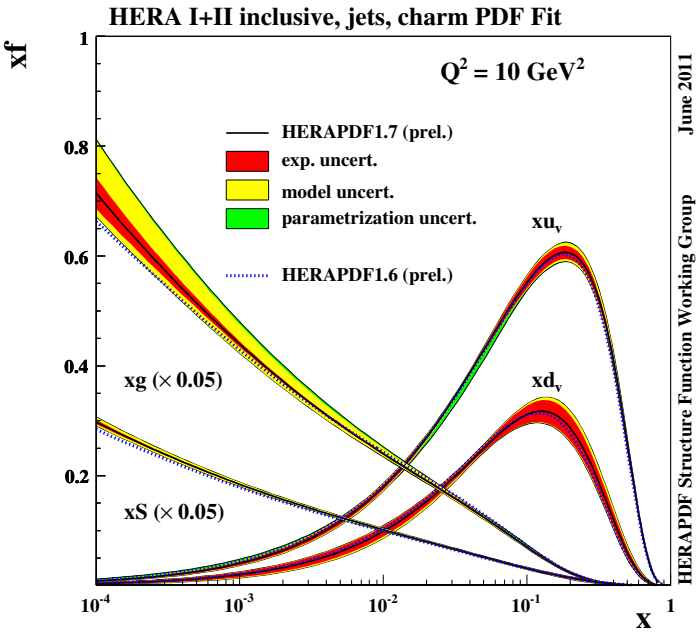

Figure 1.3: Momentum distribution functions (PDFs) of partons in the proton at $Q^2 = 10$ GeV^2. The curves xu_v and xd_v correspond to the distribution of valence u and v quarks. xS includes sea quarks with all six flavors and xg is for the gluons. At small-x (high beam energies for fixed Q^2) the wave function of a nucleon is dominated by gluons. (Figure from https://www.desy.de/h1zeus/combined_results/herapdftable/)

set of variables $\{x, Q^2\}$. For the definition of these variables, see Eqs. (1.1) and (1.2).

The momentum distribution function $xf(x, Q^2)$ is found by multiplying the parton distribution function $f(x, Q^2)$ with the momentum fraction x. Henceforth, we will refer to $xf(x, Q^2)$ as also the parton distribution function. In Fig. 1.3, the PDF of a proton at $Q^2 = 10$ GeV^2 is shown as a function of x. At low energies (small $\sqrt{s}$, large $x \sim 0.2$), the two valence u quarks carry approximately 2/3 of the total momentum and the d quark carries approximately 1/3 of the total momentum. However, with increasing energy (decreasing x), the population of the sea quarks (denoted as xS and it includes all six quark flavors) rises. The broadening of the two curves corresponding to the valence u and d quarks is due to the interactions of the constituents of the proton. Our main focus here is on the rapid rise of the gluon number with decreasing x.

The small-x partons are seen as radiation of the large-x partons that act as sources. The partons at small- and large-x are related to each our via renormalization group equations. As x gets smaller with increasing collision energy, the nucleon/nucleus gets packed more and more by gluons until they start to overlap. The interaction of gluons causes a reduction in the number of gluons. At a certain value of x for a fixed scale $Q^2 = Q_{\rm s}^2$, the rise in the gluon density due to the bremsstrahlung is equilibrated by the reduction due to the recombination of gluons. After that point in x, the density of gluons with transverse size $1/Q^2 = 1/Q_{\rm s}^2$ saturates and becomes maximal [9]. If the rise in the density of the gluons did not saturate at some scale $Q_{\rm s} \gg \Lambda_{\rm QCD}$, this would create a problem such that unitarity would be violated (violation of Froissart-Martin bound on cross sections [10, 11, 12].)

In addition to the emergence of a new scale $Q_{\rm s}$ at which $\alpha_{\rm s}$ is expected to be weak, the high occupation numbers of small-x (long wavelength) gluons justifies the use of classical Yang-Mills (CYM) equations instead of QCD. This is the main premise of the Color Glass Condensate model. This approach opens up a new regime where the non-perturbative, low-energy physics of the hadronic structure is not necessarily correlated with strong coupling: The coupling constant $\alpha_{\rm s}$ is expected to be weak because of the saturation scale that is set by the high density of the gluons, but on the other hand, since there are many of these weakly interacting gluons, the classical field they form becomes strong.

Once the wave-function of the nucleus is described in terms of classical glue fields, the model can be applied to heavy-ion collisions. In ultrarelativistic heavy-ion collisions, the two nuclei pass through each other without significant stopping and the kinetic energy of the nuclei is not significantly reduced during the collision. As the two nuclei pass through each other at high energies (or small-x since $x \sim Q/\sqrt{s}$), the interaction can be understood in terms of the interaction of the classical color fields of the colliding nuclei.

The non-Abelian character of the strong force allows interaction of the gluons among themselves even without the mediation of fermions (quarks). In the quantized theory (QCD), the non-Abelian term in the field strength

$$F_{\mu\nu} = \partial_\mu A_\nu - \partial_\nu A_\mu - ig[A_\mu, A_\nu], \tag{1.8}$$

gives rise to the three-gluon and four-gluon interaction vertices.

The nuclei in ultrarelativistic heavy-ion collisions are highly contracted in the longitudinal direction since the typical values of the Lorentz factor are $\gamma = 100$ ($\sqrt{s} = 200$ GeV per nucleon pair) at RHIC and $\gamma = 1350$ ($\sqrt{s} = 2.76$ TeV per nucleon pair) at LHC. The classical color fields before the collision are contracted in the longitudinal coordinate, hence they are transverse. When these initial transverse fields from each nuclei overlap and interact, they generate longitudinal chromo-electric E^a and chromo-magnetic B^a fields. These fields form color flux tubes stretching between the receding nuclei. The index $a = 1, \ldots, 8$ is for the $SU(3)$ color group.

The generation of longitudinal fields from the initial transverse fields during the collision and the evolution of these longitudinal fields are governed by CYM, which is given as

$$[D_\mu, F^{\mu\nu}] \equiv \partial_\mu F^{\mu\nu} - ig[A_\mu, F^{\mu\nu}] = gJ^\nu, \tag{1.9}$$

where $A_\mu = A^a_\mu t^a$ and t^a are the Gell-Mann matrices of $SU(3)$. The energy density of these longitudinal E^a and B^a fields stretched between the receding nuclei at proper time τ after the collision can be written in terms of E^2 and B^2 as it is done in classical electrodynamics.

The collision energy is deposited in the longitudinal color fields and it is a function of the transverse coordinates and space-time rapidity. Soon after the collision (in proper time $\tau < 1$ fm/$c \sim 3 \times 10^{-24}$ s), the color flux tubes stretched between the nuclei are expected to decay into quarks and gluons, which is followed by a rapid thermalization. At some time between 0.4 fm/$c < \tau < 1$ fm/c, the local thermal equilibrium of the very dense and hot system is established. After this time the expanding fireball is modeled by relativistic hydrodynamics. That the fluid model works better than the gas model for the evolution of QGP has been verified based on the comparison between the computed and measured spatial distribution of the momenta of the final hadrons [13]. The expansion lasts only a few fm/c, and as the temperature and energy density drop, confinement sets in and quarks and gluons combine to form hadrons. When the temperature drops below the freeze-out temperature, the hadrons expand as a noninteracting gas until the individual hadrons reach the detectors. It should be emphasized that the initial energy density, along with the initial entropy density, affects the multiplicy, transverse momentum and rapidity distributions of the detected particles. The main purpose of the work presented in this thesis is calculation of the initial energy density after the

collision. In the literature, the initial energy density is either calculated from the Color Glass Condensate, an effective theory based on QCD, in the midrapidity region ($y \approx 0$), or it is calculated from phenomenological Glauber-type models. What is new in this thesis is the rapidity profile of the initial energy density; this is achieved by applying the three-dimensional McLerran-Venugopalan model (3dMVn).

The outline of this thesis is as follows:

- Chapter 2 presents an introduction to heavy ion collisions and Quark Gluon Plasma.
- Chapter 3 gives an overview of the Color Glass Condensate framework and the 3dMVn model. Then it shows the results of comparing the 3dMVn model with a data parametrization on parton distribution functions.
- Chapter 4 includes calculation of the initial energy density and its rapidity dependence. It also demonstrates the results on the initial energy density for top RHIC and LHC energies.

Chapter 2

Heavy Ion Collisions

In this chapter, we give an introduction to heavy ion collisions and evolution of the Quark Gluon Plasma (QGP) to provide a context for our work that is presented in the following chapters. The overview here is kept brief since our work is mostly related to the wave functions of the colliding nuclei in the classical Yang-Mills approximation. In the following chapters, we calculate the initial energy density of the collision. The initial energy density and its dependence on rapidity, along with the transverse coordinate, determine the evolution of the QGP and consequently the final distribution of hadrons. We refer the reader who is interested in heavy ion collisions and QGP beyond the overview presented here to the reviews [14, 15] and books [16, 17, 2, 18, 19, 20, 21]

Reaching dense baryonic matter at high temperatures is the main goal of the heavy ion experiments. Heavy ion collisions provide an opportunity to explore the phase diagram of Quantum Chromodynamics (QCD). The phases are diverse due to the color $SU(3)_{\rm c}$ symmetry of the gluons, approximate flavor $SU(3)_{\rm f}$ symmetry and chiral $SU(3)_{\rm L} \times SU(3)_{\rm R}$ symmetry of the quarks that is realized at high temperature and baryon density.

Heavy ion collisions started with the BEVALAC, at Lawrence Berkeley Laboratory (LBL) at early 70's in US. The beam energy in this fixed target experiment was about 1 GeV per nucleon. This was followed by other facilities such as Joint Institute for Nuclear Research (JINR) in Dubna and the SIS heavy ion synchrotron at Gesellschaft für Schwerionenforschung (GSI) in Darmstadt. In the mid 80's, Super Proton Synchrotron (SPS) at CERN started fixed-target experiments with oxygen and sulpher beams at

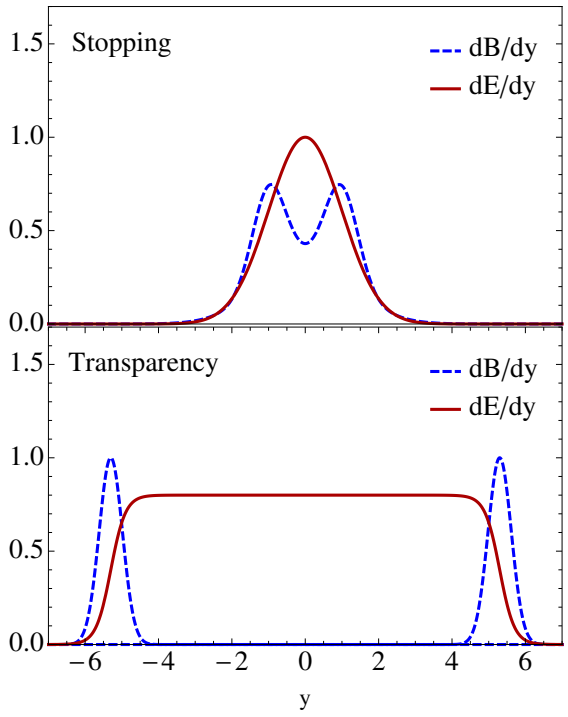

Figure 2.1: Stopping and transparency in heavy ion collisions. (Top) The target and projectile nuclei, which have larger initial rapidities than shown in the blue dashed curves, loses their rapidity due to the collision. Nucleus at the positive (negative) rapidity moves in the $+z$ ($-z$) direction. Blue dashed lines also show the baryon number per rapidity, dB/dy. Red curves show energy per rapidity, dE/dy. (Bottom) At extreme energies, two nuclei are expected to pass through each other by leaving energy in between, but no significant baryon density. After the collision, target and projectile nuclei preserve most of their kinetic energy (rapidity). (Figure adapted from [2]).

60 GeV per nucleon whereas Alternating Gradient Synchrotron (AGS) at BNL used silicon-ion beam. Currently, we have data available from RHIC for Au-Au ($A = 197$) collisions at $\sqrt{s} = 200$ GeV per nucleon pair and from LHC for Pb-Pb ($A = 208$) at $\sqrt{s} = 2.76$ TeV per nucleon pair. The rapidity is given by $y_{\rm max} = \ln[\sqrt{s}/m_{\rm nucleon}]$. Hence, the rapidity coverage at these top energies are $y = \pm 5.3$ (RHIC) and $y = \pm 8$ (LHC).

In Fig. 2.1, two scenarios for heavy ion collisions are shown; stopping and transparency. When two nuclei stop each other, high baryon number is observed around mid-rapidity, $y \approx 0$. The energy per rapidity (shown in red) is also peaked around

mid-rapidity. This is observed in fixed-target experiments at AGS for Au-Au collisions at beam energy 11.4 GeV. At extremely high energies, two nuclei are expected to pass through each other without a significant energy loss. This also means that the baryon chemical potential is practically zero in the central region between the receding nuclei. At top RHIC and LHC energies, the picture of transparent collisions are more relevant since the colliding nuclei preserve most of their initial kinetic energy after the collision. The energy density and hadrons produced in the central region are expected to have a flat distribution for a few units of rapidity. Flat distribution in rapidity brings boost invariance because observables would be invariant under Lorentz boosts $y \to y + \Delta y$. This symmetry was utilized by Bjorken to find an approximate solution to relativistic hydrodynamics. The energy density is usually calculated for mid-rapidity. In the following Chapters, we will calculate the rapidity dependence of the energy density and find a rapidity profile similar to the one shown in the bottom plot in Fig. 2.1.

It would be useful to introduce the definitions regarding the kinematics of heavy ion collisions. Rapidity is used both for target and projectile as well as for the produced hadrons after the collision. Rapidity is basically extending the limits of the relativistic velocity $-c \leq v \leq c$ to $-\infty \leq y \leq \infty$. Momentum space rapidity is defined as

$$y = \frac{1}{2} \ln \left(\frac{E + p_z}{E - p_z} \right). \tag{2.1}$$

The projectile (target) beam direction is taken to be in the $+z$ (-z) direction. For a particle with energy $E^2 = \boldsymbol{p}^2 + m^2$, where $\boldsymbol{p} = (\boldsymbol{p}_{\mathrm{T}}, p_z)$, the "transverse mass" is defined as

$$m_T^2 = m^2 + \boldsymbol{p}_{\mathrm{T}}^2. \tag{2.2}$$

From these definitions, one can write

$$E = m_{\mathrm{T}} \cosh y, \tag{2.3}$$

$$p_z = m_{\mathrm{T}} \sinh y. \tag{2.4}$$

The space-time picture of the heavy ion collisions is studied best in light-cone $(x^+, x^-, \boldsymbol{x}_\perp)$ and hyperbolic coordinates $(\tau, \eta_{\mathrm{s}}, \boldsymbol{x}_\perp)$. Also, the relativistic hydrodynamics is solved both analytically [22] and numerically [3] most conveniently in hyperbolic coordinates. The definitions we give below are in accordance with the $(t, \boldsymbol{x}_\perp, z)$ coordinate system

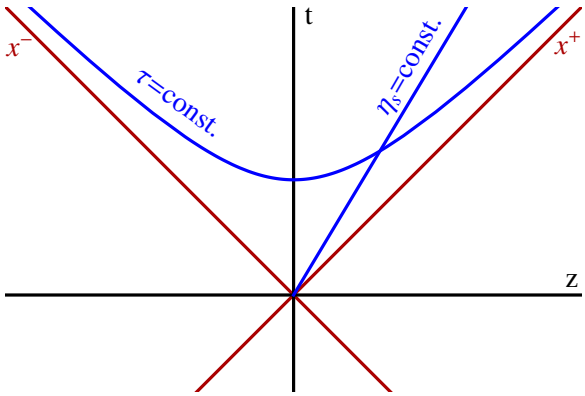

Figure 2.2: The cartesian, hyperbolic and light-cone coordinate systems. The transverse coordinate $\boldsymbol{x}_\perp$ is not shown here. In analogy to the polar coordinates (r, ϕ), τ and η_s can be considered as radius and angle, respectively, on a hyperbola. Hence, there is a coordinate singularity for η_s when $\tau = 0$. This makes it impossible to give an η_s dependence to any function at $\tau = 0$ when hyperbolic coordinates are used.

with the metric signature $g_{\mu\nu} = \mathrm{diag}(+,-,-,-)$. The light-cone coordinates are given as

$$x^\pm = \frac{t \pm z}{\sqrt{2}}. \tag{2.5}$$

The space-time rapidity is defined as

$$\eta_s = \frac{1}{2} \ln \left(\frac{t+z}{t-z} \right) = \frac{1}{2} \ln \left(\frac{x^+}{x^-} \right), \tag{2.6}$$

and the proper time is

$$\tau = \sqrt{t^2 - z^2} = \sqrt{2x^+x^-}. \tag{2.7}$$

Fig. 2.2 shows these coordinates.

Now we turn to the nucleus-nucleus collisions which are perceived as collisions of individual nucleons in the Glauber model[1] [23, 24, 25, 3]. The nucleon-nucleon (pp) inelastic cross section is known ($\sigma_{\mathrm{in}} \sim 40$ mb for a wide range of energy 3 GeV $< \sqrt{s} <$ 100 GeV). For nucleus-nucleus collisions, one defines a thickness function $T_{\mathrm{A}}(\boldsymbol{b})$ such that $\sigma_{\mathrm{in}} T_{\mathrm{A}}(\boldsymbol{b})$ gives the probability of having a nucleon-nucleon collision at impact parameter $\boldsymbol{b}$. The

[1] The initial conditions for energy density left in the central region after the collision can be calculated in this framework. The initial energy density calculated from this model is widely used by hydrodynamic simulations. In the following chapters, we will derive initial energy density based on the Color Glass Condensate where the collision is understood in terms of interaction of the classical, non-Abelian color fields E^a and B^a.

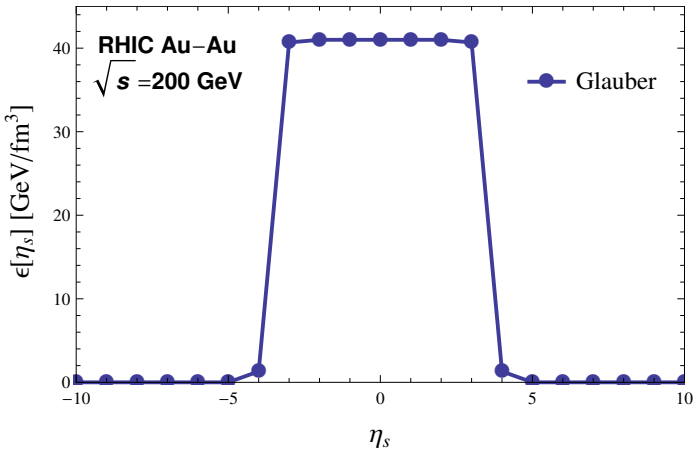

Figure 2.3: Energy density profile in space-time rapidity that is used by the MUSIC code. The energy density shown is for the center of the transverse coordinate for head-on collisions at zero impact parameter. In making this plot, we used the formulas in [65].

distribution of nucleons in a nucleus is modeled by Woods-Saxon or a step function, and this is used in defining the thickness function. The space-time rapidity profile of the initial energy density is modeled separately. In Fig. 2.3, we show the initial energy density profile in space-time rapidity that is used by the $3+1$ hydrodynamics code MUSIC (see [65] and the references therein). In the following chapters, we will compare our results with the one given in Fig. 2.3.

2.1 Quark Gluon Plasma

In QCD, the fundamental theory of the strong interactions, the fundamental degrees of freedom are quarks and gluons. However, quarks and gluons are not observed as separate particles. Since the real ground state of the theory is below than the ground state of free quarks and gluons, they are confined in hadrons due to the non-Abelian structure of the gauge group and number of quark flavors. The experimental searches of QGP is aimed to find deconfined quark matter. This can be achieved by increasing the temperature and/or baryon density.

Lattice results suggest that the transition from hadronic degrees of freedom to quark-gluon degrees of freedom takes places around the temperature $T_c \approx 170$ MeV at zero

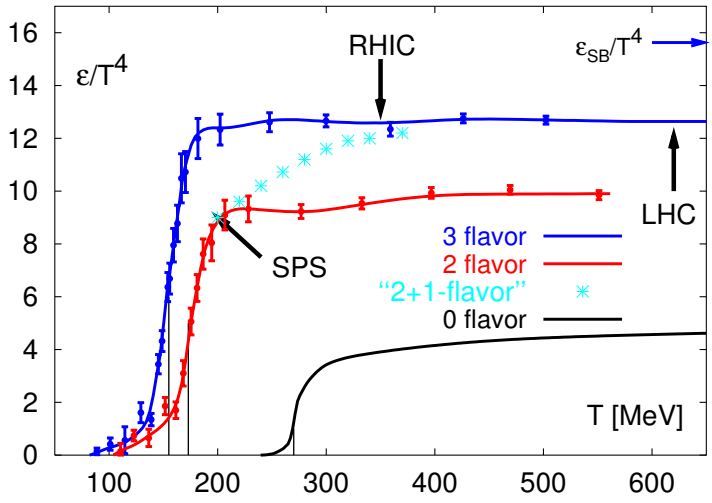

Figure 2.4: Lattice results showing the change in degrees of freedom around the temperature $T_c \approx 170$ MeV. Below T_c, we have free pion gas where degree of freedom is three. Above T_c, quarks and gluons are excited and become deconfined. Quarks come in two or three flavors, with three color charge and two spin states. There are also antiquarks. There are eight kinds of gluons and they come in two polarization states. The arrows show the typical temperatures that are reached at SPS, RHIC and LHC. At the top-right, Stefan-Boltzmann limit is shown. The pressure plots (not shown here) are continuous. (Figure from [4])

baryon chemical potential (See Fig. 2.4).

In the Color Glass Condensate (CGC) picture of the heavy ion collisions, two nuclei pass through each other while the classical strong chromo-electric and chromo-magnetic fields from each nuclei interact, and longitudinal color flux tubes[2] stretching between the receding nuclei form. These flux tubes are expected to decay into quarks and gluons at or earlier than $\tau \approx 0.1$ fm/c, where 1 fm/$c \approx 3 \times 10^{-24}$ sec. A rapid (local) thermalization of the quarks and gluons set in at this stage. This is followed by the strongly interacting QGP. The elliptical flow of the final state hadrons suggest that this new form of matter behaves like a very low-viscosity liquid rather than a gas. Hence, QGP is successfully described by relativistic hydrodynamics. As the QGP expands, it cools down and the baryon density decreases. At the freeze-out surface, the density drops to a critical value,

[2] The focus of the work presented in this thesis is calculation of the initial energy density of the longitudinal color fields and its rapidity dependence.

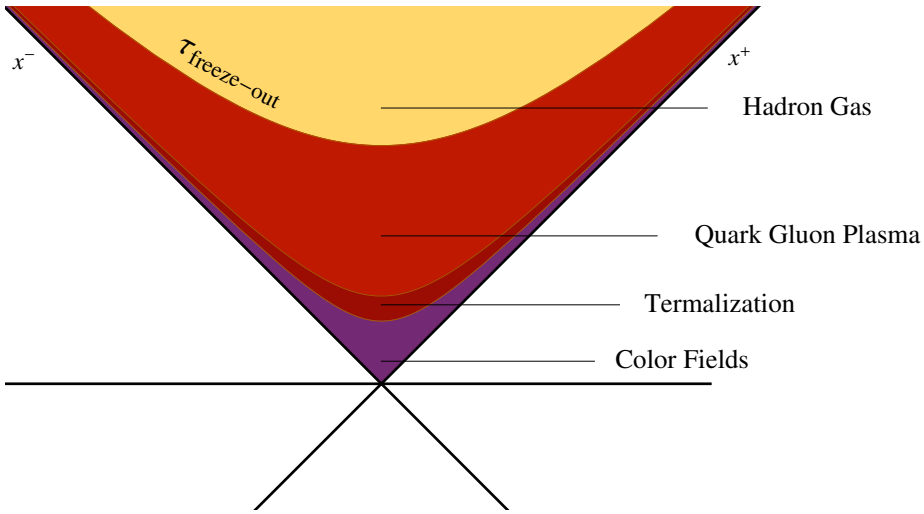

Figure 2.5: Formation and evolution of QGP. Collision of two nuclei occurs at the vertex where $x^+ = x^- = 0$. On the hyperbolic boundaries the proper time τ is constant.

the confinement sets in again and quarks and gluons combine to form hadrons. Later, this hadron gas expands until hadrons are casually disconnected, and then individual hadrons fly out to the detectors (See Fig 2.5).

In the next Chapter, we will delve into the CGC picture of the relativistic nuclei.

Chapter 3

Color Glass Condensate

In this chapter, we introduce the fundamental concepts of the Color Glass Condensate (CGC) and the implementation of these concepts in an effective model (McLerran-Venugopalan model) based on QCD. The applications of the saturation and CGC are not restricted to calculation of the initial energy density. In the overview presented below, however, we will take a quick look at the aspects of CGC that are relevant for calculation of the initial energy density. Interested readers are referred to the excellent reviews and books written on the subject [26, 27, 9, 28, 5].

The three-dimensional, color neutral McLerran-Venugopalan model (3dMVn) used in this work is different than the original McLerran-Venugopalan model (MV); the latter treats the colliding nuclei as two-dimensional, infinitely thin sheets. Also the 3dMVn is color neutral; it comes with a free parameter λ which sets the scale for the color neutrality on the nucleon level. The purpose of this chapter is to fix λ along with α_s. This has been done in our paper [29] by comparing the JR09 data parametrization[1] and the gluon distribution function calculated from 3dMVn. The application of 3dMVn to heavy ion collisions is made in Chapter 4.

The central idea in CGC is the saturation [31] which predates CGC. The saturation occurs when the gluons in a nucleon/nucleus start to overlap. Although gluons are bosons, they are charged and they interact directly when they overlap, which occur when the density of the gluons are high for a given x and Q^2. These concepts are

[1] JR09 [30] parametrization of the data provides PDF sets for proton. It is more convenient to use parametrized PDF sets rather using the raw data.

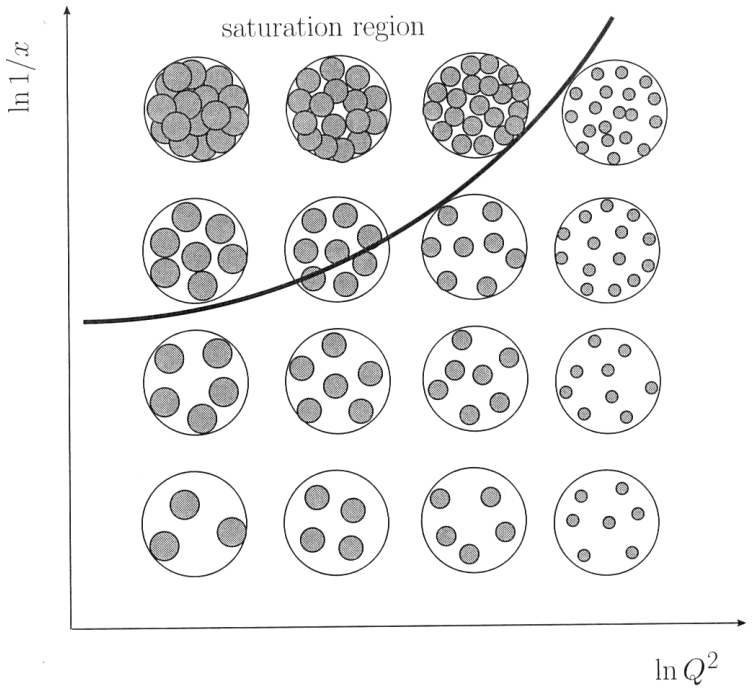

Figure 3.1: "Map of high energy QCD." Partons of a nucleon or nucleus with different sizes and at different densities are shown. The lower-left corner (small-x, low-Q^2) corresponds to low energy QCD where the wave function of the nucleon/nucleus is dominated by valence quarks. The parton density evolves in the horizontal direction with the DGLAP equation. For evolution in the vertical direction, BFKL, BK and JIMWLK equations are used. At small-x and low-Q^2, one enters the saturation region where gluon recombination and screening become important. Experimentally, small-x corresponds to high beam energies $\sqrt{s}$ for a given Q^2. (Figure from [5])

explained best throughout the landscape of QCD shown in Fig. 3.1. The variables x and Q^2 corresponds to the longitudinal and transverse momentum scales of a given parton (see the discussion of deep inelastic scattering in the Introduction).

The picture shown at the bottom-left corner of Fig. 3.1 is how a nucleon looks in a large-x, low-Q^2 DIS event. In this regime, the number of partons are low and they are mostly valence quarks along with some gluons. In other words, the nucleus is dominated by the "sources" rather than the "radiation." Other points on the (x, Q^2) plane can be accessed by renormalization group evolution equations. The Dokshitzer-Gribov-Lipatov-Altarelli- Parisi (DGLAP) equation evolves the parton distribution function

given at an initial energy Q_0^2 to a different energy. The Balitsky-Fadin-Kuraev-Lipatov (BFKL) equation, on the other hand, evolves partons in x.

The DGLAP equation for evolution of the gluon distribution function $g(x, Q^2)$ is given by [7]

$$\frac{d\, g(x,Q^2)}{d\log Q} = \frac{\alpha_{\rm s}(Q^2)}{\pi}\int_x^1 \frac{dz}{z}\left\{ P_{g\leftarrow q}(z)\sum_f \left[f_f\left(\frac{x}{z},Q^2\right) + f_{\bar f}\left(\frac{x}{z},Q^2\right)\right] + P_{g\leftarrow g}\; g\Big(\frac{x}{z},Q^2\Big)\right\}. \tag{3.1}$$

Here $f_f(x/z, Q^2)$ and $f_{\bar f}(x/z, Q^2)$ are quark and antiquark distribution functions and the index f runs over all six quark flavors. At large-x, only u and d quarks and gluons will contribute. The splitting functions $P_{g\leftarrow q}$ and $P_{g\leftarrow g}$ at a given longitudinal momentum fraction z give the probability (amplitude squared) of a gluon radiated from a quark ($g \leftarrow q$) or a gluon ($g \leftarrow g$). The splitting functions and the coupling constant $\alpha_{\rm s}$ should be calculated at the same order, e.g., LO, NLO, NNLO etc. During the evolution to a higher Q^2, the gluon radiation which dresses the quarks are seen with better resolution. The integration in Eq. (3.1) runs from x to 1. Hence, when the gluon distribution function is evolved from Q_0^2 to a higher Q^2 at a fixed x, all of the partons between x and 1 will contribute to the radiation at $\{x, Q^2\}$. The LHS of Eq. (3.1) includes a scaling operator, and the term in RHS can be interpreted as violation of this scaling. The PDFs do not scale with Q^2 since the structure functions of the nucleon change depending on Q^2 due to the splitting of partons. When the gluon PDF is evolved to higher energies, the nucleon becomes more and more dominated by partons with smaller transverse size $\sim 1/Q$, and consequently the nucleon becomes more dilute. This is the high Q^2 limit of the cartoon in Fig. 3.1.

It should be noted that the DGLAP equation for the gluon PDF uses splitting functions for processes such as $g \to g + g$ and $q \to q + g$, however, it does not take into account the gluon recombination processes $g + g \to g$. For recombination-type processes one needs a term that is nonlinear in $g(x, Q^2)$, whereas the RHS of Eq. (3.1) is linear in $g(x, Q^2)$. Gluon recombination becomes important at small-x, where the number of gluons with any transverse size rises (see top-left corner of the Fig. 3.1). Hence, the DGLAP equation becomes unreliable at small-x. Similarly, the BFKL equation is also linear and hence not able to penetrate the saturation region, where the nucleon is dense (top-left region of the Fig. 3.1 separated by the thick line). Both DGLAP and BFKL

equations work best at the bottom-right corner of Fig. 3.1, where the coupling constant is small (due to high Q^2) and parton overlap is minimal as the nucleon is dilute at large-x.

The top-left corner in Fig. 3.1 is the "high energy limit of QCD" since high beam energy $\sqrt{s}$ corresponds to small-x for a given Q^2. The saturation region (small-x) can be accessed via the Jalilian-Marian-Iancu-McLerran-Weigert-Leonidov-Kovner (JIMWLK) equation, or its large-N_c limit, the Balitsky-Kovchegov (BK) equation. In the saturation region, Q^2 is not necessarily high, however, the coupling constant is expected to be weak since it is to be calculated at the saturation scale $Q_\mathrm{s} \gg \Lambda_\mathrm{QCD}$ rather than the momentum scale Q^2. This new scale emerges from the high gluon density and it can be determined for a nucleus from

$$Q_\mathrm{s}^2 \sim \alpha_\mathrm{s}(Q_\mathrm{s}^2)\frac{A\,xg(x,Q_\mathrm{s}^2)}{\pi R_A^2}, \tag{3.2}$$

where A and R_A are the mass number and radius of the nucleus. The saturation scale increases as $A^{1/3}$ ($R_A = r_0 A^{1/3}$).

In the saturation regime, one has two advantages: i) The coupling constant is weak, hence weak coupling techniques becomes useful (perturbation theory and Feynman diagrams). ii) Due to the high occupation number of the long wavelength (small-x) gluons, one can utilize their coherence and use the classical Yang-Mills equation (CYM). In the framework of CGC, the nucleus at high energies (small-x) is seen as a "condensate" of gluons. The classical field can be thought of as the order parameter and it becomes very strong, $A_\mu^a \sim 1/\alpha_\mathrm{s}$. "Color" refers to the color charge of $SU(3)$ gauge group. The word "glass" is an allusion to glasses that are solid on short time scales and liquid on very long time scales. Similarly, the time evolution of the color charges at large-x (high momentum partons) is slow due to the time dilation. Hence, the color charge distribution of the nucleus $\rho^a(\boldsymbol{x})$ is frozen on the time scales of a typical collision mediated by strong interactions. Hence, the nucleus in heavy ion collisions are pictured in CGC as transverse, frozen ("glass"), strong ("condensate") and classical chromo ("color") -electric and -magnetic fields. The interaction of the classical glue field from the nuclei during the collision causes the formation of flux tubes to be created out of longitudinal chromo E^a and B^a fields (see Fig. 3.2). Quarks and gluons are produced by breaking

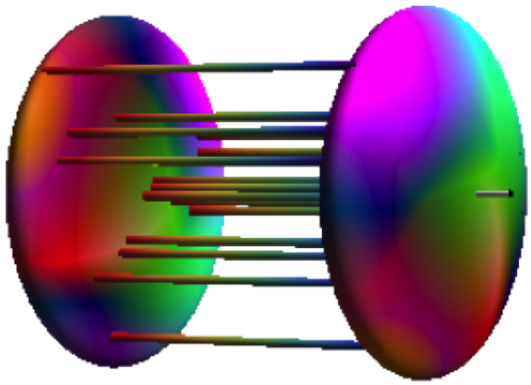

Figure 3.2: Caricature of heavy ion collisions. The nuclei are seen as SU(3) color fields traveling at high speed and the color flux tubes are formed between the two nuclei as a result of the interaction. It should be noted that the nuclei are not taken to be infinitely thin sheets in this work; they have a non-zero thickness in the longitudinal direction. This means that the gluons in the nuclei come with varying wavelengths, hence, the gluon distribution function is x_{Bj} dependent. Therefore, the results will be rapidity dependent.

of these flux tubes[2], hence, calculation of the energy stored in these longitudinal fields is important.

In the following section, we give an overview of the McLerran-Venugopalan (MV) model. As an implementation of the ideas of CGC, the MV model calculates the ensemble averaged correlation function of the classical glue fields $\langle A_i^a(\boldsymbol{x})A_i^b(\boldsymbol{x}')\rangle$. The Fourier transform of this correlator is related to the unintegrated gluon distribution and it is the main ingredient of the initial energy density and gluon number multiplicity calculations. The following sections are based on the work of the current author in [29].

3.1 The Original McLerran-Venugopalan Model

The energy deposited in the color flux tubes after the collision can be related to the two-point vector potential correlation function $\langle A_i^a(\boldsymbol{x})A_i^b(\boldsymbol{x}')\rangle_{1,2}$ in a given nucleus where

[2] In the color-flux-tube models, only longitudinal electric fields are considered. In CGC, longitudinal magnetic fields are as important as the longitudinal electric fields. For review on color-flux-tube models, see [20].

the indices refers to the nucleus 1 and 2. In symmetric nuclear collisions such as Au-Au and Pb-Pb, the index can be dropped because this ensemble averaged quantity will be the same for both nuclei, unless one is interested in event-by-event analysis. In the original MV model, the nuclei are taken to be infinitely thin two-dimensional sheets. However, the setup, in principle, may be two (transverse) or three-dimensional, depending on whether or not the Lorentz contracted nucleus is assumed to have a longitudinal thickness in the lab frame. This correlator can be derived analytically from the color charge density correlator $\langle \rho^a(\boldsymbol{x})\rho^b(\boldsymbol{x}')\rangle$ by using the classical Yang-Mills equations.

The philosophy behind the ensemble averaging is as follows. The color charge density of a nucleus $\rho^a(\boldsymbol{x})$ during a collision cannot be known precisely; on the other hand, the fluctuations in the color charge density can be studied in the effective field theory approach with ensemble averaging. In CGC, a framework for slowly evolving high density gluons within the ultrarelativistic nucleus, the fast partons are seen as sources of the small-x (soft) gluon radiation, where x is the fraction of the total longitudinal momentum carried by a parton. After integrating out the fast partons, the observables can be calculated by averaging them over the ensemble of all possible color charge configurations. Once the correlator[3] $\langle \rho^a(\boldsymbol{x})\rho^b(\boldsymbol{x}')\rangle$ is specified, it can be linked to the vector field correlator $\langle A_i^a(\boldsymbol{x})A_i^b(\boldsymbol{x}')\rangle$ from which the gluon distribution function $xg(x,Q^2)$ and other observables, such as the initial energy density, can be calculated. Here $\langle\cdots\rangle$ denotes the ensemble average. See Ref. [27] for a comprehensive review.

The ensemble averaging is tantamount to averaging over many collision events. Hence, the information coded in the event-by-event fluctuations in the positions of the quarks and gluons in a nucleus is lost during the color averaging. An alternative to the color averaging would be sampling $\rho^a(\boldsymbol{x})$ with Monte Carlo techniques, solving the CYM for each color charge configuration, calculating the observables such as energy density for each sample, and averaging the results at the end. An example of this line of research can be found in [32, 33]; however, we follow the former approach here.

In the original two-dimensional MV model, the ensemble averaging is implemented

[3] Note that both correlators $\langle \rho^a(\boldsymbol{x})\rho^b(\boldsymbol{x}')\rangle$ and $\langle A_i^a(\boldsymbol{x})A_i^b(\boldsymbol{x}')\rangle$ are for a given nucleus before the collision. Hence, the positions $\boldsymbol{x}$ and $\boldsymbol{x}'$ correspond to two points on the same nucleus.

by calculating any observable over all possible color configurations as follows

$$\langle \mathcal{O} \rangle = \int W[\rho] \mathcal{O}, \tag{3.3}$$

where the weight function is given by

$$\exp\left[-\frac{1}{\mu^2} \int d^2\boldsymbol{x}_\perp d^2\boldsymbol{x}'_\perp \mathrm{Tr}[\rho(\boldsymbol{x}_\perp)\delta(\boldsymbol{x}_\perp - \boldsymbol{x}'_\perp)\rho(\boldsymbol{x}'_\perp)] \right]. \tag{3.4}$$

Here μ^2 is the color charge density squared (see below Eq. (3.11)). The average and the fluctuations of the color charge density of a nucleus are given by

$$\langle \rho^a(\boldsymbol{x}_\perp) \rangle = 0, \tag{3.5}$$

$$\langle \rho^a(\boldsymbol{x}_\perp)\rho^b(\boldsymbol{x}'_\perp) \rangle = \delta^{ab}\mu_A^2 \, \mathcal{D}(\boldsymbol{x}_\perp - \boldsymbol{x}'_\perp), \tag{3.6}$$

where $\boldsymbol{x}_\perp$ is the transverse coordinate system for the infinitely thin nucleus, μ_A^2 is the average color charge density squared per unit (transverse) area for a nucleus, and $\langle \cdots \rangle$ denotes the ensemble average. The function $\mathcal{D}$ determines the spectrum of the fluctuations.

The weight function in Eq. (3.4) is Gaussian since the exponent is quadratic in $\rho(\boldsymbol{x}_\perp)$ (for the non-Gaussian "odderon" terms such as $\rho\rho\rho$ in the exponent, see [34]). The existence of the delta function implies white noise, which will be discussed later. Figure 3.3 shows some members of the ensemble constructed by the weight function in Eq. (3.4). The colored dots symbolize color charges (quarks or gluons) distributed over the nucleus. All these charge configurations contribute with a different weight in the averaging process. For example, the weight of the cartoon in (b) would be very small since it is less likely in a given event that a majority of the partons would be collected on one side of the nucleus. The partons in (e) looks evenly distributed over the nucleus, however, the three kinds of color are lumped at different locations in the nuclei; this configuration is also less likely. Note that, according to the picture shown in Fig. 3.3, the quarks and gluons are assumed to roam freely in the nucleus without being confined in nucleons, i.e., there is no correlation between quarks and gluons. In other words, $\rho(\boldsymbol{x}_\perp)$ is taken to be a random field with white noise. A more realistic picture will be shown in Fig. 3.4.

The white noise approximation creates infrared divergences. In the early formulation of the CGC by McLerran and Venugopalan [35, 36, 37, 38, 39], the spectrum of the

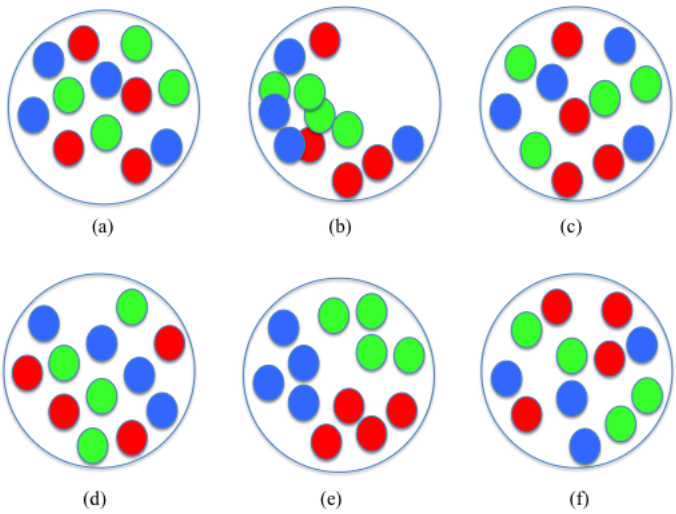

Figure 3.3: Some members of the charge configuration ensemble. In each collision, quarks with color red, green or blue in a nucleus are positioned differently. The positions of the color charges are encoded in the color charge density $\rho^a(\boldsymbol{x})$, however, it cannot be known for a particular collision. Therefore, a statistical approach using an ensemble averaged quantities becomes inevitable. The configuration in (b) does not contribute much to the weight function since it is very unlikely for quarks in a nucleus to gather on one side of the nucleus. The configuration in (e) is also unlikely since there is high order in the way colors gather in specific locations.

Gaussian color fluctuations was taken to be white noise[4]. This results in arbitrarily long wavelength fluctuations where $\langle A_i^a(\boldsymbol{x})A_i^b(\boldsymbol{x}')\rangle$ diverges in the infrared. This problem originates from the fact that confinement effects (color neutrality) have not been taken into account. Adding a gluon mass to the gluon propagator so as to bypass this problem breaks gauge invariance which is required later to convert the solution of the classical Yang-Mills equations from the axial gauge to the light-cone gauge by means of Wilson lines.

In the original MV model, the colliding nuclei are considered to be two-dimensional infinitely thin sheets traveling at the speed of light. In this approximation, the model does not depend on the longitidunal coordinate, hence there is no dependence on the

[4] Discussing the character of the gluon correlations, as determined by the weight function, in the language of white and colored noise is due to the current author [29].

momentum fraction x of a given parton. In other words, all of the partons in the nucleus have the same momentum fraction x. Being an artifact of the infinite momentum frame, the lack of x dependence in the model does not reflect the true nature of the x-dependent gluon distribution functions.

In what follows, we consider a color neutral three-dimensional McLerran-Venugopalan (3dMVn) model by Lam and Mahlon [40, 6], where the spectrum of the Gaussian fluctuations is taken to be infrared-safe colored noise. Colored noise creates a "correlation hole" in the correlation function on the size of a nucleon and this leads to color neutrality. (The term "colored noise" is not related to the color charge of QCD.) This model comes with another important feature that the incoming nuclei are not exactly on the light-cone. Longitudinal coordinate dependence produces an x-dependent gluon distribution function. This enables us to compare the model with the data parametrization of gluon distribution functions and therefore fix the parameters of the 3dMVn model. Once this is achieved, the 3dMVn model can be used to calculate the initial energy density distribution in heavy ion collisions.

The MV model provides a framework for calculating the vector field correlation function $\langle A_i^a(\boldsymbol{x}) A_i^b(\boldsymbol{x}')\rangle$ from which the gluon distribution function as well as the initial energy density distribution can be calculated. We emphasize that our ultimate goal is calculating the latter, which will be pursued in Chapter 4. In the present Chapter, we focus on the calculation of the gluon distribution function and its comparison with data for the purpose of fixing the free parameters in the 3dMVn model.

We proceed as follows. First, we give a brief overview of the color neutral and x-dependent version of the McLerran-Venugopalan model (3dMVn) given by Lam and Mahlon [40, 6]. Next, we calculate the gluon distribution function from the 3dMVn model. This model works at low-Q^2 where no data for the gluon distribution functions is available. For that reason, we evolve our results with the Dokshitzer-Gribov-Lipatov-Altarelli-Parisi (DGLAP) equation to higher momenta where data is available. This is followed by a discussion of the data parametrization that we use to compare with the 3dMVn model. Lastly, we compare the 3dMVn with the data parametrization.

3.2 The 3dMVn Model

In the previous section, the color charge density $\rho(\boldsymbol{x}_\perp)$ of a nucleus is assumed to be a Gaussian random field that fluctuates from event to event. Recall that the average and the fluctuations were given as

$$\langle \rho^a(\boldsymbol{x}_\perp)\rangle = 0, \tag{3.7}$$

$$\langle \rho^a(\boldsymbol{x}_\perp)\rho^b(\boldsymbol{x}'_\perp)\rangle = \delta^{ab}\mu_A^2\,\mathcal{D}(\boldsymbol{x}_\perp - \boldsymbol{x}'_\perp), \tag{3.8}$$

where $\boldsymbol{x}_\perp$ is the transverse coordinate system for the infinitely thin nucleus, μ_A^2 is the average color charge density squared per unit (transverse) area for a nucleus, and $\langle\cdots\rangle$ denotes the ensemble average. The function $\mathcal{D}$ determines the spectrum of the fluctuations. When white noise is assumed, $\mathcal{D}(\boldsymbol{x}_\perp - \boldsymbol{x}'_\perp) = \delta^2(\boldsymbol{x}_\perp - \boldsymbol{x}'_\perp)$, no correlation occurs between different points in a nucleus. This also means that fluctuations in each momentum mode, including the zero mode, are equally likely and there is no characteristic scale. In this case, even though the correlator $\langle A_i^a(\boldsymbol{x}_\perp)A_i^b(\boldsymbol{x}'_\perp)\rangle$ is calculated with an infrared cutoff Λ_{QCD} [41], it still diverges like $(\boldsymbol{x}_\perp^2)^{\boldsymbol{x}_\perp^2}$ in the infrared. Therefore, the Fourier transform of it, which is necessary to calculate the gluon distribution function, does not exist [40]. This cut-off can also be understood as a gluon mass in the gluon propagator in the form $(\boldsymbol{q}_\perp^2 + m_{\mathrm{gluon}}^2)^{-1}$. It explicitly breaks the gauge invariance that is needed to convert the solutions of classical Yang-Mills equations from the axial gauge to the light-cone gauge where Wilson lines are to be used.

In reality, a nucleus is color neutral on scales larger than a nucleon size. A color neutral correlation function can be derived from a simple model of a nucleus where nucleons are composed of quark and antiquark pairs [42]. If we consider a two-dimensional nucleus for a moment, the assumption that only the quark and antiquark pair from the same nucleon can interact with each other produces a correlator of the form [40]

$$\langle \rho^a(\boldsymbol{x}_\perp)\rho^b(\boldsymbol{x}'_\perp)\rangle = \delta^{ab}\mu_A^2\left[\delta^2(\boldsymbol{x}_\perp - \boldsymbol{x}'_\perp) - \frac{\exp\left[-|\boldsymbol{x}_\perp - \boldsymbol{x}'_\perp|^2/4\lambda^2\right]}{4\pi\lambda^2}\right]. \tag{3.9}$$

Here the parameter λ, which we will refer to as a correlation length, is of the order of a nucleon size $\sim 1\,\mathrm{fm}$. This parameter takes away the need for a sharp infrared cutoff as it is used in the original MV treatment. Moreover, it makes the Fourier transform of the vector field correlation function well-defined and it renders the model infrared

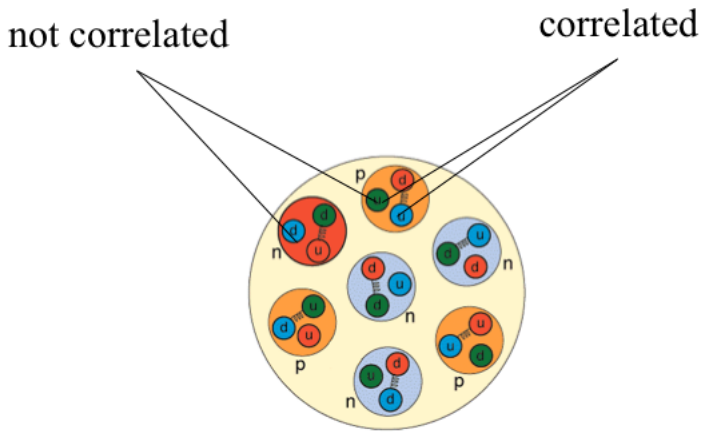

Figure 3.4: A more realistic picture of the nucleus. Quarks separated with large distances are not correlated and on that scale the charge density can be approximated with a random field. For scales comparable to the nucleon's size, the interaction among quarks become important, therefore, at small distances, the quark density cannot be taken as a random field.

safe. In Eq. (3.9), decorrelation due to the white noise $\mathcal{D}(\boldsymbol{x}_\perp - \boldsymbol{x}'_\perp) = \delta^2(\boldsymbol{x}_\perp - \boldsymbol{x}'_\perp)$ is modified by the last term for distances $|\boldsymbol{x}_\perp - \boldsymbol{x}'_\perp| \lesssim \lambda$, reflecting the assumption that there is a correlation between the partons confined to a region smaller than the nucleon size. The second part in Eq. (3.9) removes the zero mode $|\boldsymbol{q}_\perp| = 0$ from the white noise spectrum, hence colored noise. The Fourier transform of the correlator in Eq. (3.9) is proportional to $1 - \exp[-\lambda^2 \boldsymbol{q}_\perp^2]$, which vanishes as $|\boldsymbol{q}_\perp| \to 0$. This makes the model infrared safe.

A more realistic picture of the nucleus where quarks and gluons are confined in nucleons, is shown in Fig. 3.4. For large distances ($r \gg 1$ fm), the correlator $\langle \rho^a(\boldsymbol{x}_\perp)\rho^b(\boldsymbol{x}'_\perp)\rangle$ acts as a decorrelation function (white noise). This behavior is mimicked by $\delta(\boldsymbol{x}_\perp - \boldsymbol{x}'_\perp)$ in Eq. (3.9). For small separations ($r \lesssim 1$ fm), also the exponential term in Eq. (3.9) becomes important and it colors the spectrum of the fluctuations. In other words, the second term subtracts the fluctuations with long wavelengths (small momenta) which exists in the white noise spectrum due to the delta function. This is physical because

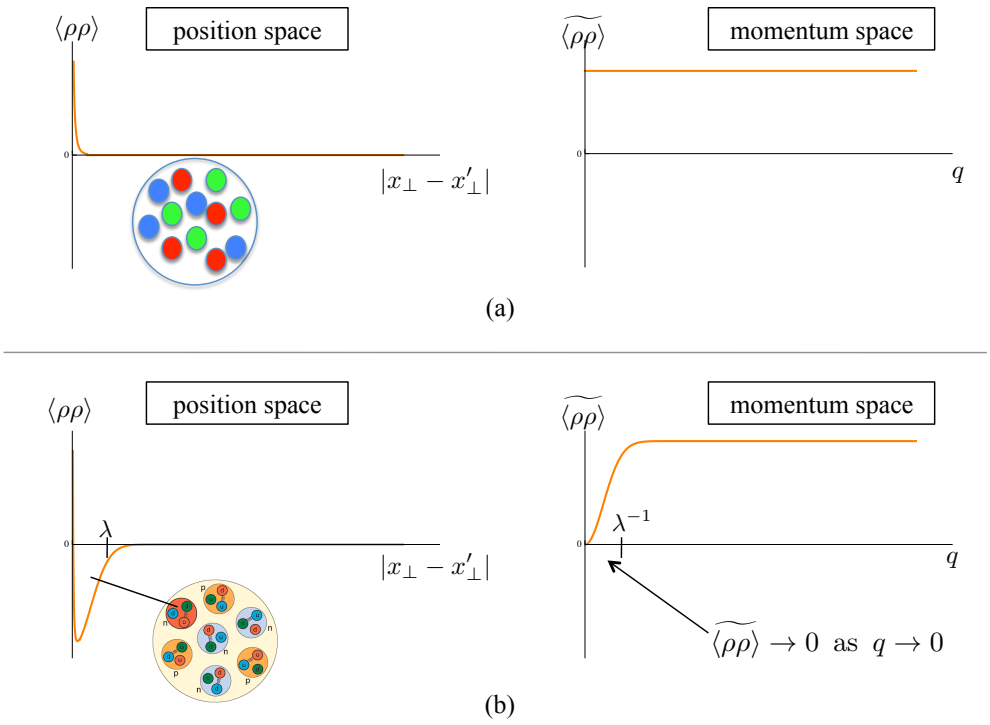

Figure 3.5: Spectrum of the (a) white and (b) colored noise. White noise corresponds to decorrelation between quarks at all scales, thus no confinement. Colored noise brings about the effect of quark confinement on the nucleon scale.

the quarks at short distances are indeed correlated and the color charge density cannot be modeled with a random stochastic field. Figure 3.5 shows the spectrum of (a) white and (b) colored noise. In the case of (a) the white noise, the correlator has only the delta function. In momentum space this corresponds to a situation where all the momentum modes contributes to the spectrum equally, including the problematic infrared modes ($|\boldsymbol{q}_\perp| \to 0$). As for the colored noise in (b), the modes in the infrared ($|\boldsymbol{q}_\perp| \lesssim \lambda^{-1}$) are removed from the spectrum due to the exponential term in Eq. (3.9).

In this work, we adopt a three-dimensional correlator

$$\langle \rho^a(0,0)\rho^b(\boldsymbol{x})\rangle = \delta^{ab}\kappa_A^3\left[\delta^3(\boldsymbol{x}) - \frac{3}{4\pi\lambda^2}\frac{\exp\left(-\sqrt{3}|\boldsymbol{x}|/\lambda\right)}{|\boldsymbol{x}|}\right], \tag{3.10}$$

where κ_A^3 is the average color charge squared per unit volume

$$\kappa_A^3 = \frac{N_{\rm c}C_{\rm F}A}{N_{\rm c}^2-1}\frac{1}{V} = \frac{A}{2}\frac{1}{V}. \tag{3.11}$$

Here $N_{\rm c}$ is the number of colors, V is the volume of a nucleus and the color factor is defined as $C_{\rm F} = (N_{\rm c}^2-1)/(2N_{\rm c})$. Since we are dealing with fluctuations of the form $\langle\rho\rho\rangle$, we need the average charge-squared density. Equation (3.11) can be found as follows. A quark in a nucleon carries a charge of gt^a, where t^a's are 3×3 SU(3) matrices. Charge-squared for a nucleon is given by

$$g^2{\rm tr}(t^at^a) = g^2N_{\rm c}C_{\rm F}, \tag{3.12}$$

where the trace is over the i,j components of the 3×3 matrix $(t^a)_{ij}$ and $C_{\rm F} = (N_{\rm c}^2-1)/2N_{\rm c}$. The total color charge squared for a nucleus is found by multiplying Eq. (3.12) with A, the number of nucleons in a nucleus. The charge squared density which is proportional to $\langle\rho^a\rho^a\rangle$ then becomes $g^2N_{\rm c}C_{\rm F}A/V$. By using the identity, ${\rm tr}[t^at^b] = \delta^{ab}/2$ and $\delta^{ab}\delta^{ab} = N_{\rm c}^2-1$, we can write

$$\langle\rho^a\rho^b\rangle = \frac{\delta^{ab}}{N_{\rm c}^2-1}\langle\rho^a\rho^a\rangle. \tag{3.13}$$

Hence, $\langle\rho^a\rho^b\rangle$ will be proportional to κ_A^3 given in Eq. (3.11). In writing Eq. (3.11), we have omitted the term g^2 since we write it explicitly in CYM equation as $[D_\mu, F^{\mu\nu}] = gJ^\nu$ (see Eq. (1.9)).

We write $d^3\boldsymbol{x} = dx_\parallel d^2\boldsymbol{x}_\perp$ where $x_\parallel$ is the longitudinal coordinate in the direction of the beam axis, and $\boldsymbol{x}_\perp$ is the coordinate on the transverse plane. The Fourier transform of the corralator (3.10) is given by [6]

$$\widetilde{\langle\rho^a\rho^b\rangle} = \delta^{ab}\kappa_A^3\left[1 - \frac{1}{1+\lambda^2\boldsymbol{q}^2/3}\right]. \tag{3.14}$$

Despite the slight difference between the correlators in Eqs. (3.9) and (3.10), they produce similar results. It can be readily seen from Eq. (3.14) that the zero mode does not exist in the spectrum since $\widetilde{\langle\rho^a\rho^b\rangle} \to 0$ as $|\boldsymbol{q}| \to 0$.

In ultrarelativistic heavy ion collisions, the infinite momentum frame provides a good starting point for the parton picture of the nucleus. However, the nucleus becomes infinitely thin when it is exactly on the light-cone ($\beta \equiv v/c = 1$) and the gluon distribution function calculated from the MV model turns out to be independent of x. Here we review the formulation by Lam and Mahlon [6] for the case where the nucleus is boosted to speed $\beta < 1$. In the lab frame, the thickness of a nucleus of radius R becomes of the order of R/γ.

The current for a nucleus moving in the $+z$ direction is given by

$$J_r^0 = \rho(-z, \boldsymbol{x}_{\perp r}); \quad \boldsymbol{J}_r = 0, \tag{3.15}$$

where the subscript r stands for the rest frame and the negative sign in front of the z is for later convenience. With the redefinition $x^{\pm} = -x_{\mp} = (t \pm z)/\sqrt{2}$, the current can be rewritten in the light-cone coordinates (still in the rest frame),

$$J_r^+ = J_r^- = \frac{1}{\sqrt{2}}\rho\left(\frac{1}{\sqrt{2}}(x_r^- - x_r^+), \boldsymbol{x}_{\perp r}\right); \quad \boldsymbol{J}_{\perp r} = 0. \tag{3.16}$$

When we go from the rest frame to the lab frame where the nucleus moves with speed β, the current in Eq. (3.16) becomes

$$J^+ = \frac{1}{\varepsilon}\rho\left(\frac{1}{\varepsilon}x^- - \frac{\varepsilon}{2}x^+, \boldsymbol{x}_\perp\right); \quad J^- = \frac{\varepsilon}{2}J^+; \quad \boldsymbol{J}_\perp = 0, \tag{3.17}$$

where

$$\varepsilon = \sqrt{\frac{2(1-\beta)}{1+\beta}}. \tag{3.18}$$

Here we can define a new longitudinal coordinate

$$x_\parallel \equiv \frac{1}{\varepsilon}x^- - \frac{\varepsilon}{2}x^+, \tag{3.19}$$

which is essentially the Lorentz tranformation of $-z = (x^- - x^+)/\sqrt{2}$ (see the definition below Eq. (3.15)). The Eq. (3.17) can be contrasted with the commonly used current in the infinite momentum frame (imf) where the nucleus is infinitely thin,

$$J^+_{\text{imf}} = \delta(x^-)\rho(\boldsymbol{x}_\perp); \quad J^-_{\text{imf}} = 0; \quad \boldsymbol{J}_{\perp\text{imf}} = 0. \tag{3.20}$$

3.3 Gluon Distribution Functions

We now turn to the calculation of the gluon distribution function from the 3dMVn model. Later we will compare it with data in order to fix the parameters $\alpha_{\rm s}$ and λ. The gluon distribution function of a nucleus with a baryon number A can be expressed as an integral of the gluon number density over the transverse momenta,

$$g_A(x,Q^2) \equiv \int_{|\boldsymbol{q}_\perp|\leqslant Q} d^2\boldsymbol{q}_\perp \frac{dN}{dxd^2\boldsymbol{q}_\perp}. \tag{3.21}$$

The gluon number density in the lab frame for a nucleus moving with speed β is given as a Fourier transform of the two-point vector field correlation function [6]

$$\frac{dN}{dq_\parallel d^2\boldsymbol{q}_\perp} \equiv \frac{q_\parallel}{4\pi^3}\int d^3\boldsymbol{x}\int d^3\boldsymbol{x}\,' e^{i\boldsymbol{q}\cdot(\boldsymbol{x}-\boldsymbol{x}\,')}\langle A_i^a(\boldsymbol{x})A_i^a(\boldsymbol{x}\,')\rangle. \tag{3.22}$$

Here $q_\parallel$ is the momentum conjugate to the coordinate defined in Eq. (3.19). The Eq. (3.22) can be related to $dN/dxd^2\boldsymbol{q}_\perp$ by using the relation $x \equiv q_\parallel/m$, which itself can be derived from the definition $x \equiv q^+/Q^+ = \varepsilon q^+/m$. Here m is the nucleon mass, q^+ and Q^+ are the momenta of the gluon and the nucleon. The gluon number density is also referred to as the unintegrated gluon distribution (UGD) $\phi(x,\boldsymbol{q}_\perp^2)$

$$\phi(x,\boldsymbol{q}_\perp^2) \equiv x\frac{dN}{dxd^2\boldsymbol{q}_\perp} = \frac{m^2x^2}{4\pi^3}\langle A_i^a(\boldsymbol{q})A_i^a(-\boldsymbol{q})\rangle. \tag{3.23}$$

The vector fields are calculated in the Weizsäcker-Williams approximation (see [43, 44]). Throughout this work, we will not distinguish the position space and momentum space vector fields $A(\boldsymbol{x})$ and $A(\boldsymbol{q})$; it it understood from the argument $\boldsymbol{x}$ or $\boldsymbol{q}$.

Solving the classical Yang-Mills equations for the source in Eq. (3.16) in the covariant gauge and transforming the solution into the light-cone gauge by using Wilson lines, one can express the correlator $\langle A_i^a(\boldsymbol{x})A_i^a(\boldsymbol{x}\,')\rangle$ in Eq. (3.22) in terms of the color charge density correlator $\langle\rho^a(\boldsymbol{x})\rho^a(\boldsymbol{x}\,')\rangle$. We skip the details of this calculation here and refer the reader to the original paper [6]. Using the correlator in Eq. (3.10), the gluon number density can be written as

$$\frac{dN}{dxd^2\boldsymbol{q}_\perp} = \frac{8A\alpha_{\rm s}}{\pi^2}\frac{1}{x}\int d^2\boldsymbol{\Delta}_\perp e^{i\boldsymbol{q}_\perp\cdot\boldsymbol{\Delta}_\perp}\mathcal{L}(x;\boldsymbol{\Delta}_\perp)\mathcal{E}(v^2L(\boldsymbol{\Delta}_\perp)). \tag{3.24}$$

Here the integration is over the transverse coordinate $\boldsymbol{\Delta}_\perp = \boldsymbol{x}_\perp - \boldsymbol{x}'_\perp$. The functions $\mathcal{L}$ and L are convolutions of the two gluon propagators at two different points in the same

nucleus connected by the three-dimensional noise term $\mathcal{D}(\boldsymbol{x}-\boldsymbol{x}')$. These two functions can be seen as pair distribution functions. The nuclear correction factor $\mathcal{E}$ takes into account the nuclear geometry and v^2 controls the strength of the dependence on this geometry.

The functions used in Eq. (3.24) are given as [6]

$$\begin{aligned}\mathcal{L}(x;\boldsymbol{\Delta}_\perp) = -\frac{1}{12\pi}\Big[&(xm\lambda)^2 K_0(xm\Delta_\perp) \\ &- \Big(3+(xm\lambda)^2\Big)K_0(\Delta_\perp\sqrt{3+(xm\lambda)^2}/\lambda)\Big],\end{aligned} \tag{3.25}$$

and

$$L(\boldsymbol{\Delta}_\perp) = -\frac{\lambda^2}{6\pi}\left[K_0\left(\frac{\sqrt{3}\Delta_\perp}{\lambda}\right)+\ln\left(\frac{\sqrt{3}\Delta_\perp}{2\lambda}\right)+\gamma_{\mathrm{E}}\right], \tag{3.26}$$

where $\Delta_\perp = |\boldsymbol{\Delta}_\perp|$. In the calculations of Lam and Mahlon [6], the nuclear matter density is taken to be uniform. The nuclear correction factor $\mathcal{E}$ is determined by the geometry of the nucleus. For cylindrical and spherical nuclei it is given by

$$\mathcal{E}(z) = \begin{cases} \dfrac{1}{z}(e^z-1) & \text{(cylindrical)}, \\ \\ \dfrac{3}{z^3}[1-\dfrac{1}{2}z^2+e^z(z-1)] & \text{(spherical)}. \end{cases} \tag{3.27}$$

This function appears in Eq. (3.24) as $\mathcal{E}(v^2L(\Delta_\perp))$. The v^2 controls how much the results depend on the nuclear geometry; it is given by

$$v^2 = \begin{cases} \dfrac{3Ag^4}{2\pi R_A^2} \approx 24\pi\alpha_{\mathrm{s}}^2 A^{1/3} r_0^{-2} & \text{(cylindrical)}, \\ \\ \dfrac{9Ag^4}{4\pi R_A^2} \approx 36\pi\alpha_{\mathrm{s}}^2 A^{1/3} r_0^{-2} & \text{(spherical)}. \end{cases} \tag{3.28}$$

Here $R_A = r_0 A^{1/3}$ and we take $r_0 = 1\,\mathrm{fm}$. The difference between the spherical and cylindrical nuclei is negligibly small. In our calculations, we use the formulae for a cylindrical nucleus.

Now we are ready to calculate the gluon distribution function $xg_A(x,Q^2)$ for a nucleus by substituting Eq. (3.24) in Eq. (3.21)

$$xg_A(x,Q^2) = \frac{8A\alpha_{\mathrm{s}}}{\pi^2}\int_{|\boldsymbol{q}_\perp|\leqslant Q} d^2\boldsymbol{q}_\perp \int d^2\boldsymbol{\Delta}_\perp e^{i\boldsymbol{q}_\perp\cdot\boldsymbol{\Delta}_\perp}\mathcal{L}(x;\boldsymbol{\Delta}_\perp)\mathcal{E}(v^2L(\boldsymbol{\Delta}_\perp)). \tag{3.29}$$

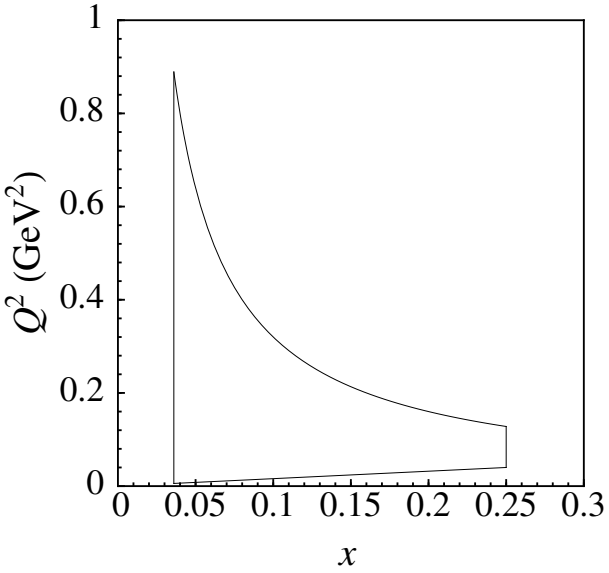

Figure 3.6: Approximate region of validity of the 3dMVn model for a gold nucleus (A=197).

The momentum integration in the equation above is trivial. Owing to the longitudinal coordinate $x_\parallel$, the fractional momentum distribution function $xg_A(x, Q^2)$ in Eq. (3.29) is x-dependent, in contrast to the results of the original two-dimensional MV model. This is the most important feature of 3dMVn, and the x-dependence will allow us to calculate the rapidity dependence of the initial energy density.

The region of validity of the 3dMVn model within the two-dimensional parameter space (x, Q^2), likewise the original MV model, is restricted by the assumptions made regarding the weak coupling limit, color coherence and color averaging [6].

The lower limit of x is set for a gold nucleus by

$$x \sim \frac{A^{-1/3}}{mr_0} \simeq 0.035, \tag{3.30}$$

where r_0 is the nucleon size $\sim 1\,\mathrm{fm}$. This is the longitudinal momentum fraction at which the gluons start to resolve the Lorentz contracted thickness of the nucleus.

The weak coupling limit imposes an upper limit on x such that

$$x \lesssim \frac{4}{\pi mr_0} \simeq 0.25. \tag{3.31}$$

For very large Q^2, not enough color charge would be seen, hence the Gaussian approximation for the color charge fluctuations $\langle \rho^a(\boldsymbol{x})\rho^b(\boldsymbol{x}')\rangle$ would not be valid. Similarly, at the scale of color neutral nucleons where Q^2 is very small, again there would not be enough color charge to average over. These considerations put limits on the momentum scale

$$\frac{\pi m}{4r_0}x \lesssim Q^2 \lesssim \frac{4}{mr_0^3}\frac{1}{x}. \tag{3.32}$$

For $r_0 = 1\,\mathrm{fm}$, Eq. (3.32) becomes

$$0.16\,x \lesssim Q^2 \lesssim \frac{0.032}{x}. \tag{3.33}$$

In our calculations, we will take $Q^2 = 0.55\,\mathrm{GeV}^2$. The reason for this choice is that it is at the upper limit of validity of the 3dMVn model and at the lower limit of the parton distribution function to which we will compare. While the model spans a larger range in x for $Q^2 < 0.55\,\mathrm{GeV}^2$ (see Figure 3.6), no data is available at those scales. At the energy scale $Q^2 = 0.55\,\mathrm{GeV}^2$, x is restricted to the range

$$0.035 < x < 0.060. \tag{3.34}$$

Figure 3.6 shows the approximate validity region of the 3dMVn model for a gold nucleus. We consider gold because it provides for the greatest range of validity of the model as represented by Eq. (3.30). The results for lead would be indistinguishable.

The parameters of the 3dMVn model need to be fixed before performing the numerical integration in Eq. (3.29). We take the nucleon mass $m = 0.94\,\mathrm{GeV}$, $r_0 = 1\,\mathrm{fm}$ and $A = 197$. The coupling constant α_s and the correlation length λ are treated as free parameters. We evaluate $xg_A(x, Q^2)$ numerically at $Q^2 = 0.55\,\mathrm{GeV}^2$ in the range $0.035 < x < 0.060$ for several values of α_s and λ in increments of 0.1 in the range

$$\begin{aligned} 0.1 \leq &\alpha_\mathrm{s} \leq 1, \\ 0.2\,\mathrm{fm} \leq &\lambda \leq 2.6\,\mathrm{fm}. \end{aligned} \tag{3.35}$$

Then we fit $xg_A(x, Q^2)$ to a form

$$xg_A(x, Q^2) = b\,x^c\,(1-x)^d, \tag{3.36}$$

and find the set $\{b, c, d\}$ for each set of $\{\alpha_\mathrm{s}, \lambda\}$. After the numerical integration, we obtain $xg_{197}(x, Q^2)$ for the whole nucleus for several points in the parameter space

$\{\alpha_s, \lambda\}$. The scale $Q^2 = 0.55\,\mathrm{GeV}^2$ at which we calculated $xg_A(x, Q^2)$ is the lower limit of the JR09 data parametrization for the parton distribution functions. For this reason, we compare JR09 with the gluon distribution functions that are calculated and evolved to $Q^2 = 100\,\mathrm{GeV}^2$.

Gluon distribution functions are evolved to different energy scales with the DGLAP equation [45, 46, 47, 48]. For this purpose, we employ the code QCDNUM17 [49]. We will assume that a nucleus is a dilute system of nucleons and take the nuclear modification factor $R = 1$ [50]. Hence,

$$xg_{p/A}(x, Q^2) \equiv \frac{1}{A} xg_A(x, Q^2), \tag{3.37}$$

where the subscript p/A refers to a nucleon in a nuclear environment. Henceforth, we will use the gluon distribution function for a single nucleon in a gold nucleus. It should be kept in mind that $g_{p/A}(x, Q^2)$ is in principle different than a gluon distribution function for an isolated proton $g_p(x, Q^2)$ since the nuclear effects introduce enhancement or shadowing depending on the energy scale Q^2.

We run QCDNUM in the variable-flavor number scheme (VFNS) and at the next-to-next-to-leading order (NNLO($\overline{\mathrm{MS}}$)). At the initial scale $Q^2 = 0.55\,\mathrm{GeV}^2$, the calculated gluon distribution function is the main input to QCDNUM. For the complete DGLAP evolution of the gluons, also the valence and sea quark distributions at the initial scale should be provided to the evolution code. However, only the gluon distribution function is calculated. For the valence and sea quark distributions, the JR09 [30] data parametrization is utilized. Therefore, the inputs to the DGLAP evolution at $Q^2 = 0.55\,\mathrm{GeV}^2$ are the calculated gluon distribution function and PDFs for the quarks from JR09. The output of the DGLAP evolution is the gluon distribution function at a higher Q^2. This will be compared with the gluon PDF from JR09. The evolution is repeated for several values of α_s and λ in the range given in Eq. (3.35).

We will compare our results with the parametrization of data by JR09 [30]. We use the PDFs that work in the VFNS scheme and at the NNLO($\overline{\mathrm{MS}}$) order. The JR09 is valid in the ranges

$$\begin{aligned} 0.55 \lesssim & Q^2 \lesssim 10^8\,\mathrm{GeV}^2, \\ 10^{-9} \lesssim & x \lesssim 1. \end{aligned} \tag{3.38}$$

The JR09 provides PDFs for separate nucleons $xg_p(x, Q^2)$ but it does not contain

any information about the nuclear modification factor R. Our results, on the other hand, are for a nucleon in a nuclear environment $xg_{p/A}(x, Q^2)$; therefore, R should be, in principle, taken into account. However, the nuclear PDFs (for example nCTEQ [51]) are available only for $Q^2 > 1\,\mathrm{GeV}^2$. As pointed out earlier, since the DGLAP equation mixes quarks and gluons during the evolution, we need the valence and sea quark distribution functions at the initial energy scale so that the gluon distribution function calculated from the model can be evolved to the higher energies. Hence, for consistency, we will utilize the quark PDFs provided by JR09 at $Q^2 = 0.55\,\mathrm{GeV}^2$ as an input to the DGLAP evolution. The discrepancy between JR09 and nCTEQ [51], encoded in the nuclear modification factor, is at most 5% at $Q^2 = 25\,\mathrm{GeV}^2$. At $Q^2 = 100$ and $1000\,\mathrm{GeV}^2$ the discrepancy is negligibly small. For that reason, we think the lack of information regarding R will not cause a significant error in our analysis.

3.4 Fixing the Parameters of the 3dMVn Model

Now we seek the sets of parameters $\{\alpha_\mathrm{s}, \lambda\}$ that produce the best fits. For this reason, we compare the gluon distribution functions, calculated and evolved to $Q^2 = 100\,\mathrm{GeV}^2$, with JR09 at the same energy.

In the DGLAP evolution to higher energies, the contribution to the radiation at a particular value of x always comes from the sources from the larger x region. Hence, the effect of gluons calculated from 3dMVn in the range $0.035 < x < 0.060$ at $Q^2 = 0.55$ GeV^2 will be more prominent at smaller x values at $Q^2 = 100$ GeV^2. For this purpose, we will compare the evolved model with JR09 in the range

$$0.015 < x < 0.04. \tag{3.39}$$

The gluons from $x < 0.015$ do not enter the DGLAP evolution and hence they do not contribute to the region in Eq. (3.39). The gluons from $0.015 < x < 1$ will enter the DGLAP evolution. We argue that the parametrization in Eq. (3.36) is a good approximation for the large-x gluons.

Our analysis shows that the best fit occurs for the values $\alpha_\mathrm{s} = 0.5$ and $\lambda = 1.8\,\mathrm{fm}$. In Fig. 3.7 we show a comparison between the JR09 data parametrization and 3dMVn model at $Q^2 = 100\,\mathrm{GeV}^2$ for $\alpha_\mathrm{s} = 0.5$ and $\lambda = 1.8\,\mathrm{fm}$. We find almost identical plots at other Q^2 values in the range $0.015 < x < 0.04$.

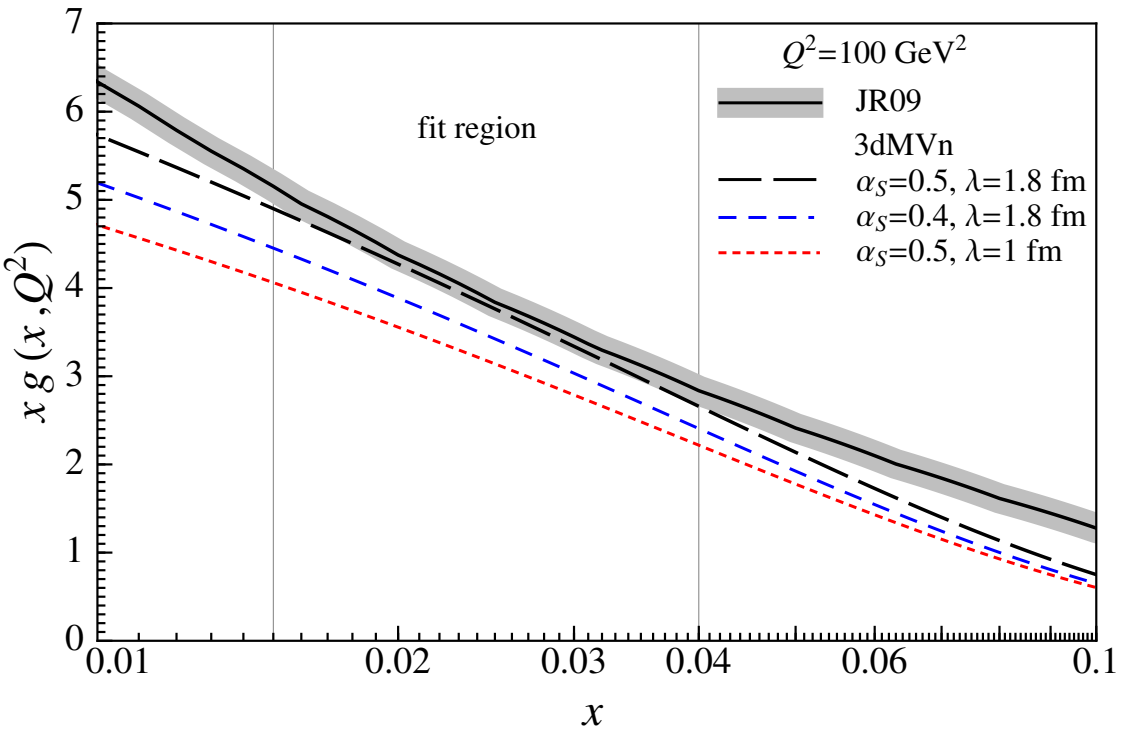

Figure 3.7: Comparison of the gluon distribution function of a nucleon from the 3dMVn model for various values of $\{\alpha_s, \lambda\}$ with the JR09 data parametrization at $Q^2 = 100\,\mathrm{GeV}^2$. The horizontal axis is in logarithmic scale. For distances larger than the correlation length λ, gluons are not correlated and hence the color neutrality condition is satisfied. The model is reliable in the fit region bounded by the two vertical lines. The uncertainty in JR09 is shown with an error band and it is about 5%. The discrepancy between the best fit curve ($\alpha_s = 0.5$ and $\lambda = 1.8\,\mathrm{fm}$) and the JR09 in the fit region is only 2%.

At other values of α_s and λ, we find that the model underestimates the data. As α_s increases, the 3dMVn curve increases and the disagreement between the model and JR09 decreases. For values $\alpha_s \geq 0.5$ the model does not change significantly. Hence, we take $\alpha_s = 0.5$ since this is the smallest value of α_s for which a good fit can be obtained. Interestingly, this freezing behavior of the strong coupling constant, particularly at $\alpha_s = 0.5$, which is imposed in other approaches by hand (see [52, 53]), arises naturally in the 3dMVn model. Adjusting λ changes the model curve only slightly. For $\alpha_s = 0.4$ and values of λ greater than 1.8 fm, we do not find a fit as good as the one for $\alpha_s = 0.5$

and $\lambda = 1.8\,\mathrm{fm}$.

There are various sources of uncertainty in the MV model which are shared with the 3dMVn model. In the paradigm of strong classical color fields, one wishes to employ solutions of the classical Yang-Mills equation which is given in covariant gauge by

$$(\boldsymbol{\nabla}_\perp^2 + \partial_\parallel^2)A^\nu = gJ^\nu + 2ig[A^\mu, \partial_\mu A^\nu] - ig[A_\mu, \partial^\nu A^\mu] + g^2[A_\mu, [A^\mu, A^\nu]], \tag{3.40}$$

where $\partial_\parallel^2 = -2\partial_+\partial_-$. The second and third terms on the right hand side of Eq. (3.40) are responsible for the three gluon interaction vertex, and the last term is for the four gluon interaction vertex in the quantized theory. In the framework of Color Glass Condensate, only the linearized version of Eq. (3.40) is used. The nonabelian feature of the model sets in when the solutions of the linearized equation in the covariant gauge are transformed to the light-cone gauge by means of the full gauge transformation including the nonabelian term [40]

$$A^\mu_{\mathrm{LC}}(x) = \mathrm{U}(x)A^\mu_{\mathrm{cov}}\mathrm{U}^{-1}(x) - \frac{i}{g}[\partial^\mu \mathrm{U}(x)]\mathrm{U}^{-1}(x). \tag{3.41}$$

The reason why the nonlinear terms in Eq. (3.40) are omitted is simply because the solutions of the fully nonlinear theory are not known. In addition, the Green's function for gluons, which is essential in the calculation of $\langle A_i^a(\boldsymbol{x})A_i^b(\boldsymbol{x}')\rangle$ from $\langle \rho^a(\boldsymbol{x})\rho^b(\boldsymbol{x}')\rangle$, can only be defined in the linear theory. The gluon propagator is calculated from

$$(\boldsymbol{\nabla}_\perp^2 + \partial_\parallel^2)G(\boldsymbol{x}) = \delta^3(\boldsymbol{x}). \tag{3.42}$$

The origin of the infrared divergences in the MV model lies here and this is also why confinement effects need to be introduced by hand by using colored noise. In principle, the correlation function with colored noise in Eq. (3.10) should be calculable from the fully nonlinear theory.

The linear approximation can only be justified if $g \ll 1$ so that the nonlinear terms can be neglected. However, the strong coupling constant is not expected to be so small and nonlinear terms are as important as the source term. Hence, the linear approximation of Eq. (3.40) is the main source of the uncertainty in any realistic analysis.

Another source of uncertainty may be the assumption that the nucleus is taken to be much larger than a nucleon, $R \gg r_0$. For a gold nucleus, the corrections may be as

large as 17% since $r_0/R \sim A^{-1/3} \sim 0.17$. Also quantum corrections at smaller values of x may be important even in the weak coupling limit. These corrections are of the form $\alpha_s \ln(1/x)$ and discussed in references [38, 39, 6]. Lastly, although we estimate that the error due to neglecting the nuclear effects should be small, it would be worth of repeating the analysis presented in this work by using nuclear PDFs once they are available for $Q^2 \sim 0.55\,\mathrm{GeV}^2$.

3.5 Summary

The framework of Color Glass Condensate allows one to calculate the vector field correlation function. It can be used to calculate the gluon distribution function of ultrarelativistic nuclei and the initial energy density distribution due to the interacting classical color fields produced by the colliding nuclei in heavy ion collisions.

In this Chapter, we have examined a three-dimensional color neutral version of the McLerran-Venugopalan model. The 3dMVn model is finite in the infrared and therefore an infrared cutoff is not needed. In addition, the results of this model are x dependent due to the intrinsic three-dimensional treatment of the nucleus in contrast to the approximation of infinitely thin nucleus.

In order to explore the parameter space of these two variables, we have calculated the gluon distribution function for several values of α_s and λ. The originality of this work is to compare our calculations directly with parametrization of the data to determine the free parameters of the model. We have found the best fit between the gluon distribution function from the JR09 parametrization and the one calculated from the 3dMVn model occurs at $\alpha_s = 0.5$ and $\lambda = 1.8\,\mathrm{fm}$. At other values of these two parameters the model underestimates the data. This may be due to the uncertainty in the assumptions made during the construction of the model as well as the other uncertainties discussed in the previous section. We have also found that the 3dMVn model had an intrinsic freezing behavior that the gluon distribution function froze at $\alpha_s = 0.5$ and remained unchanged for $\alpha_s > 0.5$.

The assumption that the color charge is normally distributed throughout the nucleus lies at the heart of the MV and 3dMVn models. Besides the normal (Gaussian) distribution of the color charge, the nucleonic inner structure of the nucleus is implemented

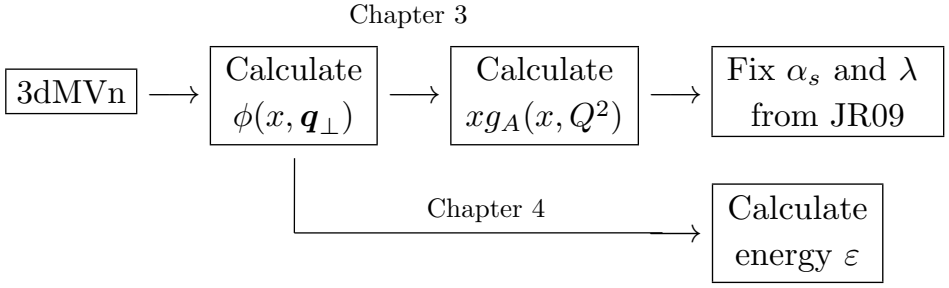

Figure 3.8: Procedures in Chapter 3 and Chapter 4.

via colored noise by introducing correlations for distances smaller than a nucleon size. In this manner, the fluctuations in the positions of nucleons in a nucleus have not been treated separately from the dynamical color charge fluctuations. In other words, the effect of confinement is realized through short range correlations in $\langle \rho^a(\boldsymbol{x})\rho^b(\boldsymbol{x}')\rangle$ by colored noise rather than considering the nucleus as a collection of individual nucleons. An alternative to this might be an event-by-event Monte Carlo sampling of the distribution of nucleons [3, 54, 32, 33]. For a finite nucleus, the results from event-by-event fluctuations in positions of the sampled nucleons may differ from the analytical calculations presented in this work. For a very large nucleus, we expect the results from both approaches to agree.

The final product of this Chapter is the unintegrated gluon distribution given in Eq. (3.24) with parameters fixed from the data. This three-dimensional quantity is the main ingredient for various applications of the CGC concept. It can be used by the practitioners of CGC and in realistic calculations other than calculation of the gluon distribution function.

In this Chapter, we calculated the gluon distribution function since it was a quantity that could be easily compared with data. However, the ultimate goal was not calculating the gluon distribution function *per se*, but to attain a working model for further use, particularly in the calculation of the initial energy density distribution in heavy ion collisions. In Chapter 4, we calculate the initial energy density in heavy ion collision in the framework of the 3dMVn model. The procedure in this Chapter and Chapter 4 are summarized in the flowchart in Fig. 3.8.

Chapter 4

Results: Rapidity Profile of the Initial Energy Density

In this chapter, the rapidity dependence of the initial energy density in heavy ion collisions is calculated from a three-dimensional McLerran-Venugopalan model (3dMVn). In this non-boost-invariant framework, the colliding nuclei have nonzero thickness in the longitudinal direction. This results in x dependent unintegrated gluon distribution functions before the collision which leads to a rapidity-dependent initial energy density after the collision. The initial energy density and its rapidity dependence are important initial conditions for the hydrodynamics simulations of the collisions.

The work presented in this work is based on the joint paper of the author and Rainer J. Fries [55].

4.1 Classical Glue Fields

Let us review the context of the classical glue fields. The classical glue field A^a_μ is a solution of the classical Yang-Mills equation (CYM). From A^a_μ, one can calculate the unintegrated gluon distribution (UGD) of the nucleus, also called the gluon number density. This quantity is the main ingredient that enters in the calculations of the initial energy density of the QGP and gluon production from classical color fields.

In CGC, the interaction of two nuclei are seen as the interaction of transverse non-Abelian classical color fields E^a and B^a which are initially localized on the Lorentz

contracted nuclei. During the interaction of these transverse fields from colliding nuclei, longitudinal fields are formed and the energy of the interaction is deposited in these longitudinal fields after the collision. Later, quarks and gluons are produced by breaking of these color flux tubes, and subsequently local thermalization of the quarks and gluons leads to the QGP.

Event-by-event and averaged energy density has been calculated before in different implementations of the CGC approach [56, 32, 33]. In this work, we calculate the initial energy density $\varepsilon(\tau = 0)$ as a function of rapidity. Here $\varepsilon(\tau = 0)$ is ensemble averaged over all possible configurations of the color charge density of a nucleus. The color charge density fluctuates on event-by-event basis. The averaging here corresponds to averaging over multiple events. We work in a three-dimensional McLerran-Venugopalan model (3dMVn) where the nuclei have a longitudinal extent [40, 6]. This allows one to calculate the rapidity dependence of the initial energy density. This is different than the earlier works where the initial energy density was independent of the rapidity since the initial fields had been taken to be rapidity-independent as a consequence of the nuclei moving at the speed of light. In addition to the fully three-dimensional treatment, the 3dMVn model comes with color neutrality built-in on the nucleon scale, which makes the model well-behaved in the infrared. The 3dMVn model has two free parameters, the strong coupling constant $\alpha_{\rm s}$ and the length scale of the color neutrality $\lambda \sim 1.8$ fm. The parameter space of the model has been explored in [29] through a comparison between the gluon distribution function calculated from the model and JR09 parametrization of the data.

The parton distribution functions (PDFs) have the feature that at very high energies (small-x for fixed Q^2) the number quarks becomes very small in comparison to the number of gluons. This has two very important consequences: First, gluons at very high occupation numbers become coherent and they can be treated with CYM. Second, the color charge density in the nucleus becomes large due to the charged gluons and this sets a new energy scale, the saturation scale for gluons, such that $Q_{\rm s} \gg \Lambda_{\rm QCD}$. At $Q_{\rm s}$, $\alpha_{\rm s}$ is expected to be weak. However, this does not mean the interaction is weak; on the contrary, the classical fields are very strong due to the coherence of many small-x gluons. This opens up a new direction where weak coupling techniques become feasible for the intrinsically nonperturbative nature of the structure of the nucleus.

The equation of motion is given by

$$[D_\mu, F^{\mu\nu}] \equiv \partial_\mu F^{\mu\nu} - ig[A_\mu, F^{\mu\nu}] = J^\nu, \tag{4.1}$$

where the field strength is defined by

$$F_{\mu\nu} \equiv \partial_\mu A_\nu - \partial_\nu A_\mu - ig[A_\mu, A_\nu]. \tag{4.2}$$

Here $A_\mu = A^a_\mu t^a$ and $a = 1 \ldots 8$ for $SU(3)$. The last term in Eq. (4.2) is responsible for the direct interaction of the color fields. As two nuclei pass through each other, the transverse fields from the colliding nuclei interact. The result of this interaction is generation of the longitudinal chromo-electric E^a and chromo-magnetic B^a fields stretching between the two nuclei. In heavy-ion collisions at very high energies, as the nuclei pass through each other (transparency rather than stopping), the interaction energy is deposited in the classical color fields. This initial energy density as a function of the transverse spatial coordinates as well as rapidity, affect the multiplicity, transverse momentum and rapidity distribution of the final particles that reach the detector.

The initial energy density can be calculated from E^a and B^a in analogy to classical electromagnetism where the energy density is given by $\mathcal{H} = 1/2(E^2 + B^2)$. These fields can be written in terms of the vector potential A^a_μ, which is created by the color charge density $\rho^a(\boldsymbol{x})$ of a nucleus (see Eq. (4.1)). The color charge configuration of the nucleus, namely, the positions of the valence quarks, cannot be known *a priori* and they fluctuate from event-to-event. At this step, one can sample the initial color charge density $\rho^a(\boldsymbol{x})$ from a Glauber-type phenomenological model and use it in Eq. (4.1) to find the color fields for each charge configuration $\rho^a(\boldsymbol{x})$. Then the energy density can be calculated for each sample and the average can be taken at the end. This approach is important if one is particularly interested in the effects of the fluctuations on observables [32, 33, 29]. However, we shall use averaged quantities as done in the original McLerran-Venugopalan (MV) model.

The main ingredient of our calculations is the UGD (see Eq. (3.23))

$$\phi(x, \boldsymbol{q}_\perp^2) \equiv x\frac{dN}{dxd^2\boldsymbol{q}_\perp} = \frac{m^2x^2}{4\pi^3}\langle A^a_i(\boldsymbol{q})A^a_i(-\boldsymbol{q})\rangle, \tag{4.3}$$

where $dN/dxd^2\boldsymbol{q}_\perp$ is given in Eq. (3.24). Here $\phi(x, \boldsymbol{q}_\perp^2)$ can also be expressed in terms of the longitudinal momentum fraction by using $x = p_\parallel/m$. In the next section, we will find the energy density in terms of $\phi(x, \boldsymbol{q}_\perp^2)$.

4.2 Rapidity-Dependent Energy Density

The aim in this section is to express the energy density of the longitudinal fields, which form after the collision, in terms of the UGD $\phi(x, \boldsymbol{q}_\perp^2)$ of the nuclei before the collision. The longitudinal fields are generated by interaction of the vector fields $A^i_{1,2}(x_\parallel, \boldsymbol{x}_\perp)$ from each nucleus during the collision, where the indices refer to nucleus 1 and 2. Henceforth, we will refer to $A^i_{1,2}(x_\parallel, \boldsymbol{x}_\perp)$ as before-fields, and we shall refer to the emerging longitudinal fields as after-fields. The UGD of the nucleus introduced in Eq. (4.3) is expressed in terms of the before-fields, and it is related to the correlation function of the vector potentials $\langle A^a_i(\boldsymbol{q}) A^a_i(-\boldsymbol{q})\rangle$ on a given nucleus before the collision.

The first goal is finding a relationship between the after-fields and the before-fields. Below, we give a short overview of the boost-invariant framework where this goal is achieved. Then we shall argue that this framework can also be used along with the non-boost-invariant 3dMVn UGDs, which depend on the longitudinal coordinate $x_\parallel$.

In [57, 58], the authors start with a boost-invariant ansatz

$$A^\pm = \pm\theta(x^+)\theta(x^-)\, x^\pm A(\tau, \boldsymbol{x}_\perp), \tag{4.4}$$

$$A^i = \theta(x^-)\theta(-x^+)A^i_1(\boldsymbol{x}_\perp) + \theta(x^+)\theta(-x^-)A^i_2(\boldsymbol{x}_\perp) + \theta(x^+)\theta(x^-)A^i_\perp(\tau, \boldsymbol{x}_\perp). \tag{4.5}$$

where $\tau = \sqrt{2x^+x^-}$ and $x^\pm = (t \pm z)/\sqrt{2}$. Here $A(\tau, \boldsymbol{x}_\perp)$ and $A^i_\perp(\tau, \boldsymbol{x}_\perp)$ are the after-fields whereas $A^i_{1,2}(\boldsymbol{x}_\perp)$ are the before-fields for nucleus 1 and 2. The vector strength $F^{\mu\nu}$ is written in terms of $A^\pm$ and A^i, which combine before- and after-fields.

The CYM should be regular when before- and after-fields interact at the hypersurface $\tau = \sqrt{2x^+x^-} = 0$

$$\lim_{\substack{\epsilon\to 0\\ \delta\to 0}} \int_{-\epsilon}^{\epsilon} dx^+ \int_{-\delta}^{\delta} dx^- \Big\{ [D_\mu, F^{\mu\nu}] = J^\nu \Big\}. \tag{4.6}$$

For $\nu = 0$ in Eq. (4.6), one obtains (see Appendix A)

$$A^i_\perp(\tau, \boldsymbol{x}_\perp)\Big|_{\tau=0} = A^i_1(\boldsymbol{x}_\perp) + A^i_2(\boldsymbol{x}_\perp). \tag{4.7}$$

Similarly, for $\nu = \pm$, Eq. (4.6) gives rise to

$$A(\tau, \boldsymbol{x}_\perp)\Big|_{\tau=0} = \frac{ig}{2}[A^i_1(\boldsymbol{x}_\perp), A^i_2(\boldsymbol{x}_\perp)]. \tag{4.8}$$

These two boundary conditions in Eqs. (4.7) and (4.8) are used to express the energy density at $\tau = 0$ after the collision in terms of before-fields $A^i_{1,2}(\boldsymbol{x}_\perp)$, which themselves can be written in terms of $\phi(x, \boldsymbol{q}^2_\perp)$ for nuclei 1 and 2.

The two boundary conditions Eqs. (4.7) and (4.8) were originally derived for boost-invariant fields. Boost invariance implies that the fields or the energy density calculated from the fields is independent of the space-time rapidity η_s. This is due to the assumption that there is no longitudinal extent of the incoming nuclei, hence the nuclei are infinitely thin and they travel at the speed of light. In reality, this is only true around mid-rapidity (see Fig. 2.3). This also implies that the fields E^a and B^a are restricted to the surface of the infinitely thin nucleus, hence there is no space-time rapidity dependence. In this framework, only the wave functions (UGDs) that look like plane waves can be used; the wave function of the nucleus cannot be composed of partons with varying momenta. This means that the results will be independent of x and the momentum space rapidity y in the boost-invariant case.

The 3dMVn UGD given in Eq. (4.3) is x-dependent. In this framework, the nucleus is seen as a wave packet of gluons with varying momentum and consequently it has a longitudinal extent. Dependence of the initial wave packets on x also brings dependence of the final results on rapidity.

In the non-boost-invariant case, the interaction cannot be defined on the sharp hyper-surface $\tau = 0$ due to the longitudinal extent of the nuclei. In that case, the limiting procedure in Eq. (4.6) is much more complicated. In our case, the hyper-surface $\tau = 0$ will be smeared for the amount of the interaction time which is $\Delta\tau \approx 0.1$ fm/c at the top RHIC energy and correspondingly smaller at the LHC. For practical purposes, we will adopt the hyper-surface $\tau = 0$ as an approximate interaction surface, and use the boundary conditions in Eqs. (4.7) and (4.8) for the $x_\parallel$-dependent initial fields (see Appendix A).

When the before-fields are boost-invariant, the initial energy density $\varepsilon(\tau = 0)$ can be written as [59, 60, 61, 62] (see Appendix B)

$$\varepsilon(\tau = 0) = \frac{1}{2}\mathrm{Tr}\, F_{ij}F_{ij} + \mathrm{Tr}(E^\eta)^2, \tag{4.9}$$

where F_{ij} is constructed from $A^i_\perp(\tau, x_\parallel, \boldsymbol{x}_\perp)$ and $E^\eta = -2A(\tau, x_\parallel, \boldsymbol{x}_\perp)$ (see Eqs. (4.4) and (4.5)). By using the boundary conditions in Eqs. (4.7) and (4.8), Eq. (4.9) can be

written in terms of the before-fields $A_1(x_\parallel, \boldsymbol{x}_\perp)$ and $A_2(x_\parallel, \boldsymbol{x}_\perp)$ (see Appendix B)

$$\begin{aligned}\varepsilon(\tau=0) = \frac{1}{2}g^2 f^{abc}f^{ade}[&\langle A_i^b A_i^d\rangle\langle A_j^c A_j^e\rangle \\ &+ \langle A_i^b A_j^e\rangle\langle A_j^c A_i^d\rangle + \langle A_i^b A_j^d\rangle\langle A_i^c A_j^e\rangle],\end{aligned} \tag{4.10}$$

where the nuclear index 1 and 2 have been dropped because the averaged fields will be the same for both nuclei when they have the same mass number. In the calculation of Eq. (4.10), we used the fact that the correlation between before-fields from nucleus 1 and 2 in the form $\langle A_1 A_2\rangle$ is zero. Equation (4.10) produces the result in [61] where the energy density is given in terms of integral of the two-dimensional MV UGD.

Now we are ready to express $\varepsilon(\tau=0)$ in Eq. (4.10) in terms of the 3dMVn UGD given in Eq. (4.3). For that purpose, we start with an ansatz which employs the color neutral, x-dependent (hence rapidity-dependent) UGD (Our ansatz here is a generalization of the one in [61] for the three-dimensional color neutral case):

$$\langle A_i^a(\boldsymbol{q})A_j^b(\boldsymbol{p})\rangle = \frac{\delta^{ab}}{N_c^2-1}\delta_{\boldsymbol{p},-\boldsymbol{q}}\langle A_i^a(\boldsymbol{q})A_i^a(-\boldsymbol{q})\rangle\frac{\boldsymbol{p}_{\perp i}\boldsymbol{p}_{\perp j}}{\boldsymbol{p}_\perp^2}. \tag{4.11}$$

Again, $\boldsymbol{q} = (q_\parallel, \boldsymbol{q}_\perp)$. Using $\delta^3(\boldsymbol{p}-\boldsymbol{q}) \Leftrightarrow V\delta_{\boldsymbol{p},\boldsymbol{q}}/(2\pi)^3$ and substituting $\langle A_i^a(\boldsymbol{q})A_i^a(-\boldsymbol{q})\rangle$ from Eq. (4.3), we find the final form of our ansatz (see Appendix C)

$$\begin{aligned}\langle A_i^a(\boldsymbol{q})A_j^b(\boldsymbol{p})\rangle = (2\pi)^3\frac{1}{V}&\delta(p_\parallel+q_\parallel)\delta^2(\boldsymbol{p}_\perp+\boldsymbol{q}_\perp) \\ &\times\frac{\delta^{ab}}{N_c^2-1}\frac{\boldsymbol{p}_{\perp i}\boldsymbol{p}_{\perp j}}{\boldsymbol{p}_\perp^2}\frac{4\pi^3}{m^2x^2}\phi(x,\boldsymbol{p}_\perp^2).\end{aligned} \tag{4.12}$$

Apart from being three-dimensional and x-dependent, our ansatz includes a $1/V$ term that the ansatz in [61] does not. This is because the UGD in [61] is defined as the UGD per unit area, and it is multiplied by the area of nucleus when calculating the gluon distribution function, unlike the definition we use in Eq. (3.21).

Now we are ready to use our ansatz in Eq. (4.12). By writing the fields in Eq. (4.10) in momentum space and substituting our ansatz gives

$$\begin{aligned}\varepsilon(\tau=0) = &\frac{g^2}{2}\frac{N_c}{(N_c^2-1)}\frac{1}{V^2} \\ &\times\int^{\Lambda_{\rm UV}}\frac{d^3\boldsymbol{p}}{(2\pi)^3}\frac{d^3\boldsymbol{q}}{(2\pi)^3}\frac{4\pi^3}{p_\parallel^2}\phi(p_\parallel,\boldsymbol{p}_\perp^2)\frac{4\pi^3}{q_\parallel^2}\phi(q_\parallel,\boldsymbol{q}_\perp^2).\end{aligned} \tag{4.13}$$

Here we go from the longitudinal momenta $(p_\parallel, q_\parallel)$ to the momentum rapidity y. The rapidity and momentum fraction for nucleus 1 and 2 are related via

$$x_{1,2} = \frac{\langle m_{\rm T}\rangle}{\sqrt{s}} e^{\pm y}, \tag{4.14}$$

where $\langle m_{\rm T}\rangle$ is the average transverse momentum of the produced gluons and $\sqrt{s}$ is the center of mass energy per nucleon pair.

By using the definition $p_\parallel = xm$ and Eq. (4.14) together with Eq. (4.13), we find (see Appendix D)

$$\begin{aligned}\frac{d\varepsilon(\tau=0)}{dy} = \frac{g^2}{2}\frac{N_{\rm c}}{(N_{\rm c}^2-1)}\frac{(2\pi^2)^2}{V^2}\left(\frac{\sqrt{s}}{\langle m_{\rm T}\rangle m}\right)^2 \\ \times \int^{\Lambda_{\rm UV}} \frac{d^2\boldsymbol{p}_\perp}{(2\pi)^2}\frac{d^2\boldsymbol{q}_\perp}{(2\pi)^2}\phi(x_1,\boldsymbol{p}_\perp)\phi(x_2,\boldsymbol{q}_\perp).\end{aligned} \tag{4.15}$$

The integral in Eq. (4.15) needs to be integrated numerically; the details of it are given in Appendix E.

In the next section, we present our numerical estimates for $d\varepsilon/dy$.

4.3 Energy Density and Its Rapidity Dependence

In order to calculate $d\varepsilon/dy$ given in Eq. (4.15) numerically, we take these parameters fixed: $N_{\rm c} = 3$, $m = 1$ GeV, $\Lambda_{\rm QCD} = 0.2$ GeV. Also, we take $\alpha_{\rm s} = 0.4$ and $\lambda = 1.8$ fm as a result of the comparison done in [29] between 3dMVn and the JR09 parametrization of the gluon distribution function. We parametrize the volume of the cylindrical nucleus (in its rest frame) with mass number A as $V = \pi R_A^2 h$ where the nuclear radius is $R_A = r_0 A^{1/3}$ and the longitudinal length (in the rest frame of nucleus) is taken to be $h = R$. For Au and Pb, we take $r_0 = 1.1$ fm and $r_0 = 1.3$ fm, respectively.

We first carry out the $d^2\boldsymbol{p}_\perp$ and $d^2\boldsymbol{q}_\perp$ integrations analytically with a ultraviolet cut-off $\Lambda_{\rm UV}$. For Pb-Pb ($A = 207$) at LHC at $\sqrt{s} = 2.7$ TeV, we use $\Lambda_{\rm UV} \sim Q_{\rm sat} \sim 2.5$ GeV for the upper limit of the integral in Eq. (4.13). For Au-Au ($A = 197$) at RHIC at $\sqrt{s} = 200$ GeV, we use $\Lambda_{\rm UV} \sim Q_{\rm sat} \sim 2$ GeV. Then, we carry out the spatial integration in Eq. (3.24) numerically in the limits $0 \le \Delta_\perp \le 2$ fm; increasing the upper limit of integration does not visibly alter the results. The transverse momentum of the produced gluons is assumed to be $\langle m_{\rm T}\rangle = 0.7$ GeV for RHIC and $\langle m_{\rm T}\rangle = 1.3$ GeV for LHC. The

details of the numerical integration can be found in Appendix E. Our results are shown in Fig. 4.1.

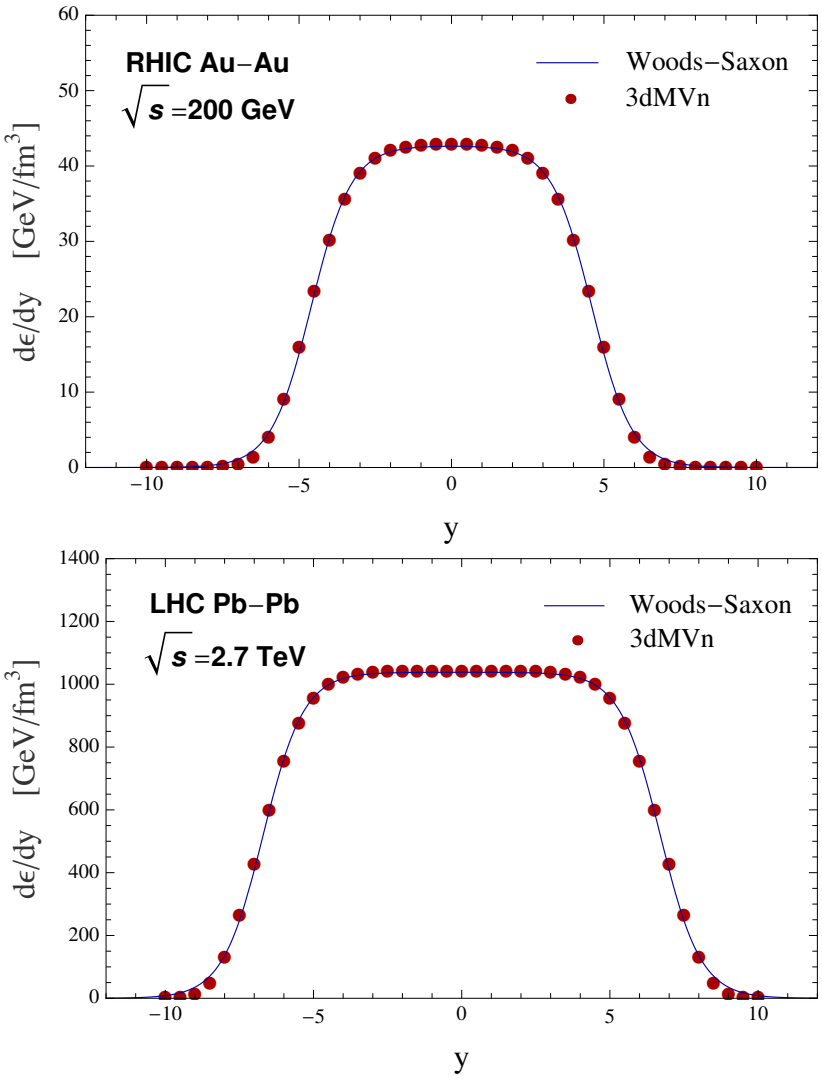

Figure 4.1: Initial energy density for LHC. See the text for the parameters used.

The momentum space rapidity y dependence of $d\varepsilon/dy$ shows the division of energy density to the momentum (y) modes of the partons. The initial energy density used in the hydrodynamics codes is, however, parametrized in terms of the space-time rapidity, η_s (see Fig. 2.3 on page 14). Figure 4.1 can also be seen as $\varepsilon[y]$ vs. y (up to some scaling

factor Δy) since

$$\varepsilon[y] \propto \varepsilon[y, y+\Delta y] = \frac{\Delta\varepsilon[y]}{\Delta y}\Delta y. \tag{4.16}$$

As $d\varepsilon[y]/dy$ follows the Woods-Saxon profile, $\varepsilon[y]$ should also be of the same form up to some absolute normalization Δy. Finally, with the assumption $y \approx \eta_s$ (see [63, 64]), we can write

$$d\varepsilon[y]/dy \propto \varepsilon[y] \propto \varepsilon[\eta_s]. \tag{4.17}$$

Our numerical calculations fit well to the Woods-Saxon profile (see Table 4.1 for the coefficients)

$$\frac{c_1}{1+\exp[(|\eta_s|-c_2)/c_3]}. \tag{4.18}$$

Our results are slightly different than the parametrization of the energy density used by the MUSIC code (see [65]) where the $\varepsilon[\eta_s]$ profile is similar to a step-function that is cut at the target and projectile rapidities ($|\eta_s| \approx 5$ for $\sqrt{s} = 200$ GeV and $|\eta_s| \approx 8$ for $\sqrt{s} = 2.76$ TeV; see Fig. 2.3 on page 14). We note that the uncertainty at high $|y|$ is largely due to these approximations and the uncertainties of UGD at high $|y|$.

The $\Lambda_{\rm UV}$ dependence of results for RHIC are given in Fig. 4.2.

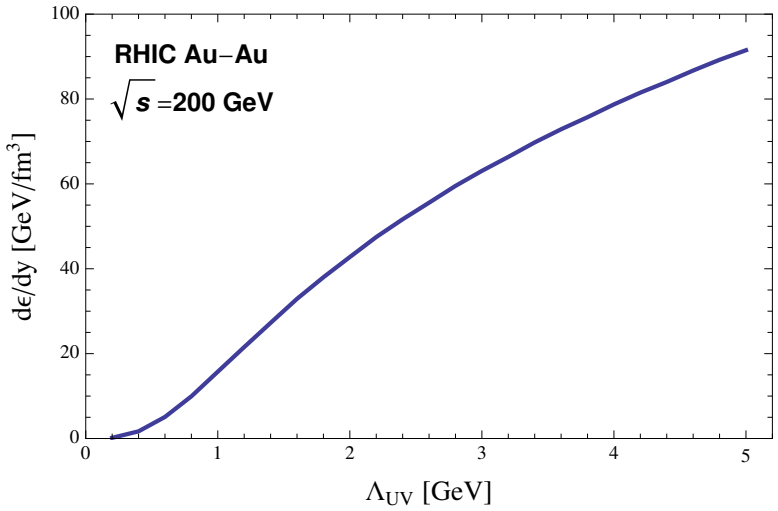

Figure 4.2: $\Lambda_{\rm UV}$ dependence of $d\varepsilon/dy$ at $\tau = 0$ for RHIC. All the other parameters are as specified in the text.

The α_s dependence for RHIC is shown in Fig. 4.3.

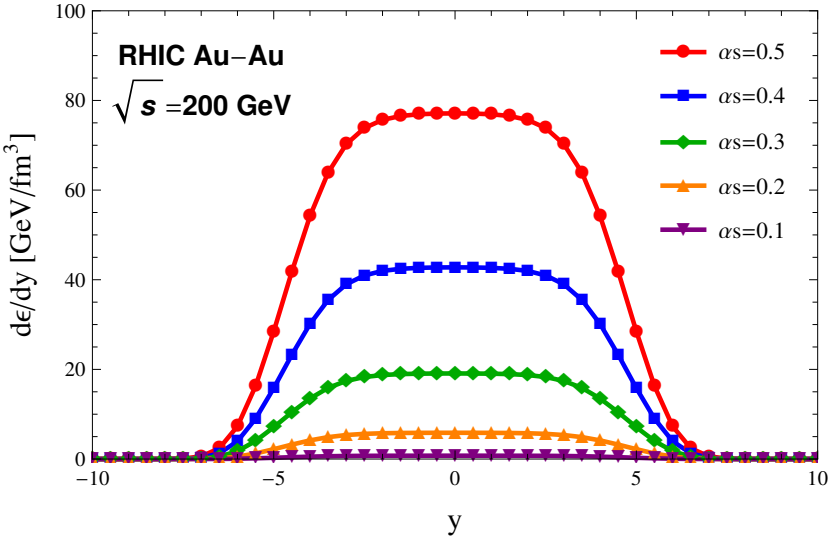

Figure 4.3: α_s dependence for RHIC. See Table 4.1 for the parameters.

The correlation length λ dependence for RHIC is shown in Fig. 4.4.

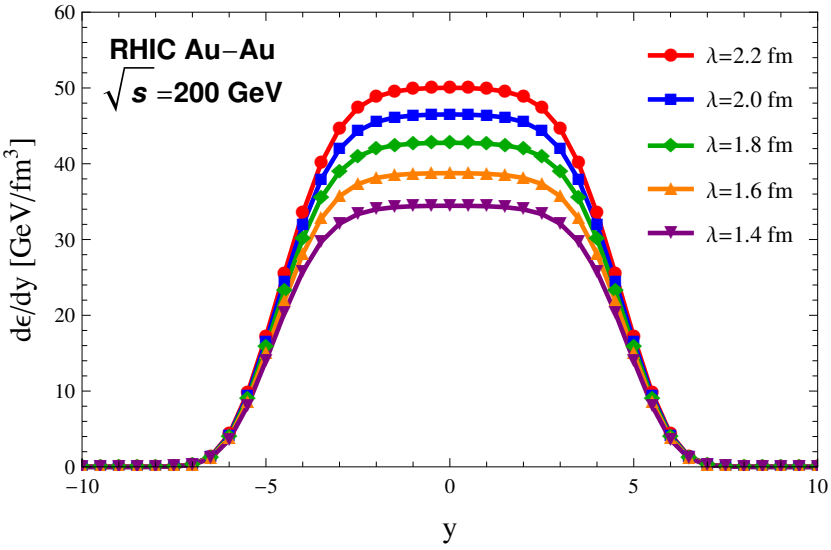

Figure 4.4: λ dependence for RHIC. See Table 4.1 for the parameters.

The transverse mass $\langle m_{\mathrm{T}} \rangle$ dependence for RHIC is shown in Fig. 4.5.

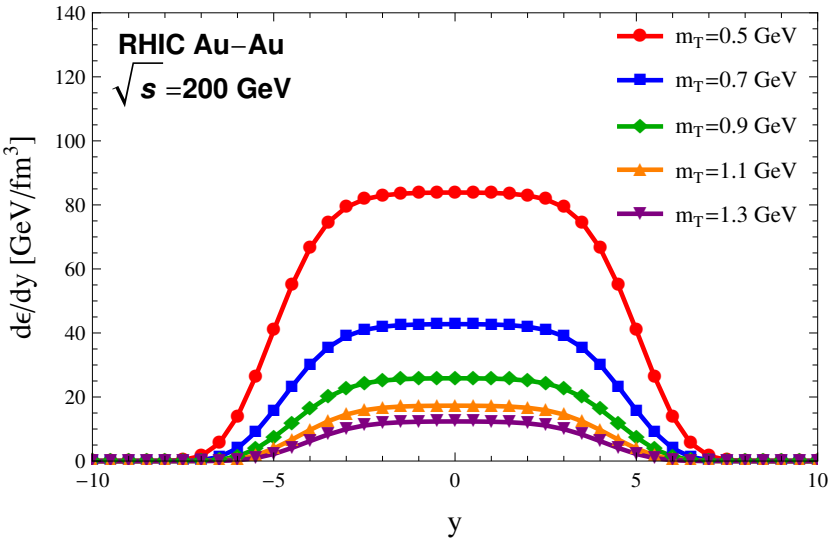

Figure 4.5: $\langle m_{\mathrm{T}} \rangle$ dependence for RHIC. See Table 4.1 for the parameters.

The Λ_{UV} dependence of results for LHC are given in Fig. 4.6.

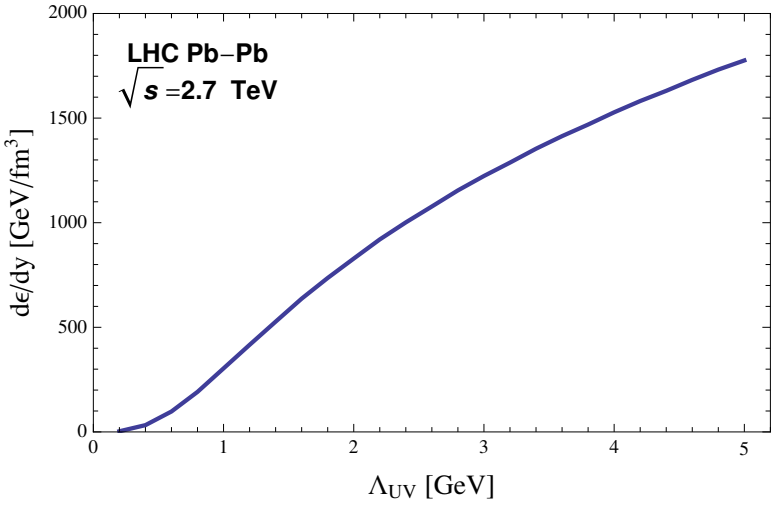

Figure 4.6: Λ_{UV} dependence of $d\varepsilon/dy$ at $\tau = 0$ for LHC. All the other parameters are as specified in the text.

The α_s dependence for LHC is shown in Fig. 4.7.

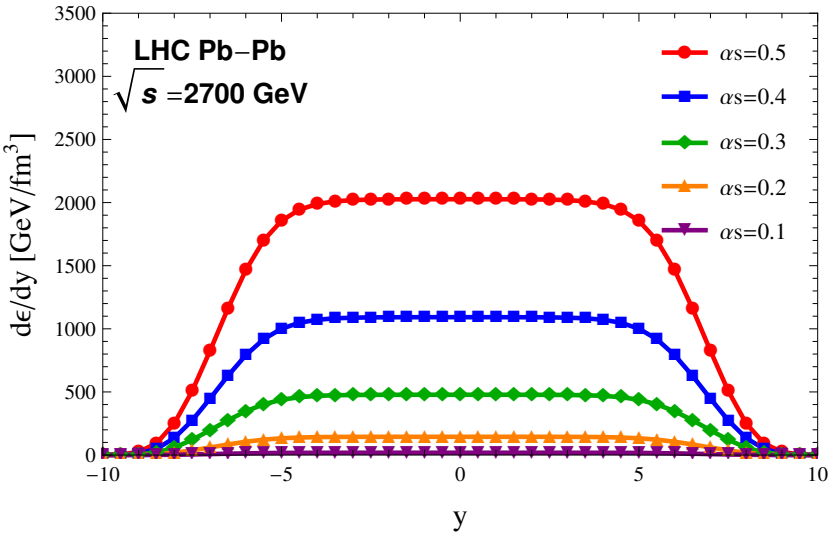

Figure 4.7: α_s dependence for LHC. See Table 4.1 for the parameters.

The correlation length λ dependence for LHC is shown in Fig. 4.8.

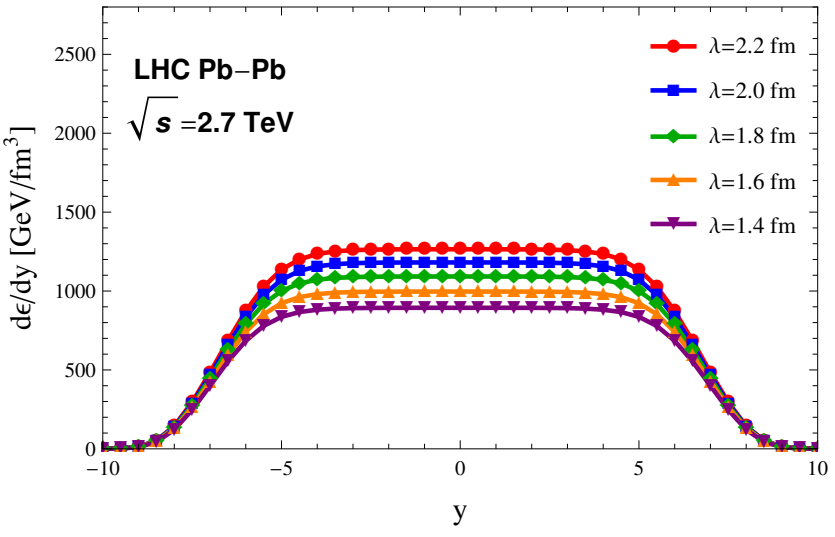

Figure 4.8: λ dependence for LHC. See Table 4.1 for the parameters.

The transverse mass $\langle m_{\mathrm{T}} \rangle$ dependence for LHC is shown in Fig. 4.9.

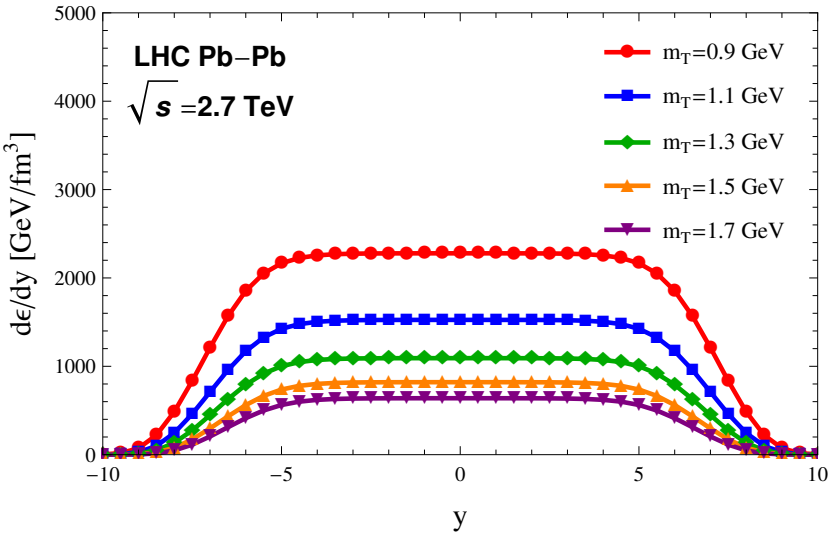

Figure 4.9: $\langle m_{\mathrm{T}} \rangle$ dependence for LHC. See Table 4.1 for the parameters.

In order to put these into context, Fig. 2.3 on page 14 can be compared with our results here. Our results show a Woods-Saxon profile for the initial energy density while the phenomenological model that the MUSIC code employs has a profile that resembles the step function.

4.4 Summary

We have calculated the initial energy density per momentum space rapidity $d\varepsilon/dy$ as a function of y at $\tau = 0$ by using the three-dimensional, color neutral MV model (3dMVn). We have made an absolute prediction for $d\varepsilon/dy$ based on the comparison with parametrized gluon distribution functions. Our results follow the Woods-Saxon profile. Up to some scaling factor, our plots can be seen as $\varepsilon[\eta_s]$ vs. η_s. Our results based on Color Glass Condensate suggest the Woods-Saxon profile for initial energy density for hydro codes rather than a short cut-off at the target and projectile rapidities.

Table 4.1: The list of parameters for the plots in Figs. 4.3, 4.4, 4.5, 4.7, 4.8, 4.9 for Woods-Saxon form $c_1/[1+\exp[(|\eta_s|-c_2)/c_3]]$. While varying one of the parameters $\alpha_{\rm s}$, λ and $\langle m_{\rm T}\rangle$, we keep the other two fixed to $\alpha_{\rm s}=0.4$, $\lambda=1.8$ and $\langle m_{\rm T}\rangle=0.7$ for RHIC, and $\alpha_{\rm s}=0.4$, $\lambda=1.8$ and $\langle m_{\rm T}\rangle=1.3$ for LHC.

		RHIC			LHC		
		c_1	c_2	c_3	c_1	c_2	c_3
$\alpha_{\rm s}$	0.2	5.8	4.6	0.7			
	0.3	19	4.6	0.7	477	6.7	0.7
	0.4	43	4.6	0.7	1091	6.7	0.7
	0.5	77	4.6	0.7	2024	6.7	0.7
λ	1.4	34	4.7	0.6	892	6.8	0.7
	1.6	39	4.7	0.6	995	6.8	0.7
	1.8	43	4.6	0.7	1091	6.7	0.7
	2.0	46	4.6	0.7	1180	6.6	0.7
	2.2	50	4.5	0.7	1264	6.6	0.7
$\langle m_{\rm T}\rangle$	0.5	84	4.9	0.7			
	0.7	43	4.6	0.7			
	0.9	26	4.4	0.7	2276	7.1	0.7
	1.1	17	4.2	0.7	1524	6.9	0.7
	1.3	12	4	0.7	1091	6.7	0.7
	1.5				819	6.6	0.7
	1.7				638	6.4	0.7

Chapter 5

Conclusion

The main focus of this thesis was calculation of the initial energy density and its rapidity profile for the ultrarelativistic heavy ion collisions at RHIC, BNL and LHC, CERN. At high energies, smaller x values are accessed. At sufficiently small-x, the gluon number rises and gluons in the nucleon/nucleus are expected to overlap with each other. It has been proposed that in a given nucleon/nucleus this tight packing of gluons may result in interactions at a scale larger than Λ_{QCD}. The scale of these interactions is set by the color charge density per transverse area. This emergent new scale, the saturation scale, opens the door for weak coupling techniques for an intrinsically non-perturbative regime of nucleon/nucleus. In Chapter 2, we presented an overview of heavy ion collisions starting from the color glass condensate state of the nucleus before the collisions to the final state hadrons flying out to detectors.

In Chapter 3, we first reviewed the original McLerran-Venugopalan (MV) model as well as its three-dimensional, color neutral extension (3dMVn). The original MV model has no x dependence, hence all the results based on it are given for around the mid-rapidity, $y \approx 0$. The 3dMVn model has x dependence; this follows from the fact that the nucleus has a longitudinal thickness, in contradistinction to the case of infinitely thin nucleus in the original MV model. The x-dependence of the unintegrated gluon distribution allowed us to find the rapidity dependence of the initial energy density right after the collision. In the same Chapter, we also showed our earlier work where the parameters of the 3dMVn model have been fixed by using the data on parton distribution functions. This allowed us to make an absolute prediction of the rapidity

profile of the initial energy density, in Chapter 4, directly based on the data. As for the normalization of the energy density, it depends on the parameters such as $\Lambda_{\rm UV}$, $m_{\rm T}$ and $\alpha_{\rm s}$, however, our results were within the known uncertainties of the energy density for the reasonable values of the parameters.

In Chapter 4, we presented the details of our calculations and our results for the initial energy density and its rapidity profile. We also provided plots demonstrating how curves changed as the parameters were varied. Our results suggest a Woods-Saxon type profile for rapidity rather than a step function as it is realized in the Glauber model.

The x-dependent, color neutral UGD of the 3dMVn model is the main ingredient of our calculations. This quantity may now be used in other studies of the color glass condensate framework.

In this thesis, we left out the calculation of the initial energy density for nonzero times such as $\tau \gtrsim 0.1$ fm/c. The evolution of the after-fields for the boost-invariant case is known in the literature. However, we work with non-boost-invariant initial fields. In order to find the time evolution of the initial fields, one needs to solve the classical Yang-Mills equation for the case that fields depend on the longitudinal coordinate. This line of research will be pursued in the future.

References

[1] J. Beringer and *et al.* (Particle Data Group). Review of particle physics. *Phys. Rev. D*, 86:010001, Jul 2012.

[2] J. Letessier and J. Rafelski. *Hadrons and Quark-Gluon Plasma*. Cambridge Monographs on Particle Physics, Nuclear Physics and Cosmology. Cambridge University Press, 2002.

[3] Bjorn Schenke, Sangyong Jeon, and Charles Gale. Elliptic and triangular flow in event-by-event (3+1)D viscous hydrodynamics. *Phys.Rev.Lett.*, 106:042301, 2011, 1009.3244.

[4] Miklos Gyulassy and Larry McLerran. New forms of QCD matter discovered at RHIC. *Nucl.Phys.*, A750:30–63, 2005, nucl-th/0405013.

[5] Yuri V. Kovchegov and Eugene Levin. Quantum chromodynamics at high energy. 2012.

[6] C.S. Lam and Gregory Mahlon. Longitudinal resolution in a large relativistic nucleus: Adding a dimension to the McLerran-Venugopalan model. *Phys.Rev.*, D62:114023, 2000, hep-ph/0007133.

[7] Michael E. Peskin and Daniel V. Schroeder. An Introduction to quantum field theory. 1995.

[8] Siegfried Bethke. The 2009 World Average of alpha(s). *Eur.Phys.J.*, C64:689–703, 2009, 0908.1135.

[9] Debasish Banerjee, Jajati K. Nayak, and Raju Venugopalan. Two introductory lectures on high energy QCD and heavy ion collisions. *Lect.Notes Phys.*, 785:105–137, 2010, 0810.3553.

[10] Marcel Froissart. Asymptotic behavior and subtractions in the Mandelstam representation. *Phys.Rev.*, 123:1053–1057, 1961.

[11] Andre Martin. Extension of the axiomatic analyticity domain of scattering amplitudes by unitarity. 1. *Nuovo Cim.*, A42:930–953, 1965.

[12] L. Lukaszuk and A. Martin. Absolute upper bounds for pi pi scattering. *Nuovo Cim.*, A52:122–145, 1967.

[13] Ulrich W. Heinz. 'RHIC serves the perfect fluid': Hydrodynamic flow of the QGP. pages 3–12, 2005, nucl-th/0512051.

[14] Sergei A. Voloshin, Arthur M. Poskanzer, and Raimond Snellings. Collective phenomena in non-central nuclear collisions. 2008, 0809.2949.

[15] Barbara V. Jacak and Berndt Muller. The exploration of hot nuclear matter. *Science*, 337:310–314, 2012.

[16] B. Müller. *The physics of the quark-gluon plasma.* Lecture notes in physics. Springer-Verlag, 1985.

[17] C.Y. Wong. Introduction to high-energy heavy ion collisions. 1995.

[18] J.B. Kogut and M.A. Stephanov. *The Phases of Quantum Chromodynamics: From Confinement to Extreme Environments.* Cambridge Monographs on Particle Physics, Nuclear Physics and Cosmology. Cambridge University Press, 2004.

[19] J.I. Kapusta and Charles Gale. Finite-temperature field theory: Principles and applications. 2006.

[20] Wojciech Florkowski. Phenomenology of Ultra-Relativistic Heavy-Ion Collisions. 2010.

[21] Sourav Sarkar, Helmut Satz, and Bikash Sinha. The physics of the quark-gluon plasma. *Lect.Notes Phys.*, 785:1–369, 2010.

[22] J.D. Bjorken. Highly Relativistic Nucleus-Nucleus Collisions: The Central Rapidity Region. *Phys.Rev.*, D27:140–151, 1983.

[23] R.J. Glauber. HIGH-ENERGY COLLISION THEORY. 1987.

[24] Roy J. Glauber. Quantum Optics and Heavy Ion Physics. *Nucl.Phys.*, A774:3–13, 2006, nucl-th/0604021.

[25] Michael L. Miller, Klaus Reygers, Stephen J. Sanders, and Peter Steinberg. Glauber modeling in high energy nuclear collisions. *Ann.Rev.Nucl.Part.Sci.*, 57:205–243, 2007, nucl-ex/0701025.

[26] Larry McLerran. RHIC physics: The Quark gluon plasma and the color glass condensate: Four lectures. 2003, hep-ph/0311028.

[27] Edmond Iancu and Raju Venugopalan. The Color glass condensate and high-energy scattering in QCD. *In *Hwa, R.C. (ed.) et al.: Quark Gluon Plasma**, pages 249–336, 2003, hep-ph/0303204.

[28] Francois Gelis, Edmond Iancu, Jamal Jalilian-Marian, and Raju Venugopalan. The Color Glass Condensate. *Ann.Rev.Nucl.Part.Sci.*, 60:463–489, 2010, 1002.0333.

[29] Sener Ozonder. Determination of the Parameters of a Color Neutral 3D Color Glass Condensate Model. *Phys.Rev.*, D87:045013, 2013, 1210.8107.

[30] P. Jimenez-Delgado and E. Reya. Variable Flavor Number Parton Distributions and Weak Gauge and Higgs Boson Production at Hadron Colliders at NNLO of QCD. *Phys.Rev.*, D80:114011, 2009, 0909.1711.

[31] L.V. Gribov, E.M. Levin, and M.G. Ryskin. Semihard Processes in QCD. *Phys.Rept.*, 100:1–150, 1983.

[32] Bjoern Schenke, Prithwish Tribedy, and Raju Venugopalan. Fluctuating Glasma initial conditions and flow in heavy ion collisions. *Phys.Rev.Lett.*, 108:252301, 2012, 1202.6646.

[33] Bjoern Schenke, Prithwish Tribedy, and Raju Venugopalan. Event-by-event gluon multiplicity, energy density, and eccentricities in ultrarelativistic heavy-ion collisions. *Phys.Rev.*, C86:034908, 2012, 1206.6805.

[34] Sangyong Jeon and Raju Venugopalan. Random walks of partons in SU(N(c)) and classical representations of color charges in QCD at small x. *Phys.Rev.*, D70:105012, 2004, hep-ph/0406169.

[35] Larry D. McLerran and Raju Venugopalan. Computing quark and gluon distribution functions for very large nuclei. *Phys.Rev.*, D49:2233–2241, 1994, hep-ph/9309289.

[36] Larry D. McLerran and Raju Venugopalan. Gluon distribution functions for very large nuclei at small transverse momentum. *Phys.Rev.*, D49:3352–3355, 1994, hep-ph/9311205.

[37] Larry D. McLerran and Raju Venugopalan. Green's functions in the color field of a large nucleus. *Phys.Rev.*, D50:2225–2233, 1994, hep-ph/9402335.

[38] Alejandro Ayala, Jamal Jalilian-Marian, Larry D. McLerran, and Raju Venugopalan. The Gluon propagator in nonAbelian Weizsacker-Williams fields. *Phys.Rev.*, D52:2935–2943, 1995, hep-ph/9501324.

[39] Alejandro Ayala, Jamal Jalilian-Marian, Larry D. McLerran, and Raju Venugopalan. Quantum corrections to the Weizsacker-Williams gluon distribution function at small x. *Phys.Rev.*, D53:458–475, 1996, hep-ph/9508302.

[40] C.S. Lam and Gregory Mahlon. Color neutrality and the gluon distribution in a very large nucleus. *Phys.Rev.*, D61:014005, 1999, hep-ph/9907281.

[41] Jamal Jalilian-Marian, Alex Kovner, Larry D. McLerran, and Heribert Weigert. The Intrinsic glue distribution at very small x. *Phys.Rev.*, D55:5414–5428, 1997, hep-ph/9606337.

[42] Yuri V. Kovchegov. NonAbelian Weizsacker-Williams field and a two-dimensional effective color charge density for a very large nucleus. *Phys.Rev.*, D54:5463–5469, 1996, hep-ph/9605446.

[43] J.D. Jackson. *Classical Electrodynamics*. Wiley, 1998.

[44] F. Halzen and Alan D. Martin. Quarks and Leptons: An Introductory Course In Modern Particle Physics. 1984.

[45] V.N. Gribov and L.N. Lipatov. Deep inelastic e p scattering in perturbation theory. *Sov.J.Nucl.Phys.*, 15:438–450, 1972.

[46] L.N. Lipatov. The parton model and perturbation theory. *Sov.J.Nucl.Phys.*, 20:94–102, 1975.

[47] Yuri L. Dokshitzer. Calculation of the Structure Functions for Deep Inelastic Scattering and e+ e- Annihilation by Perturbation Theory in Quantum Chromodynamics. *Sov.Phys.JETP*, 46:641–653, 1977.

[48] Guido Altarelli and G. Parisi. Asymptotic Freedom in Parton Language. *Nucl.Phys.*, B126:298, 1977.

[49] M. Botje. QCDNUM: Fast QCD Evolution and Convolution. *Comput.Phys.Commun.*, 182:490–532, 2011, 1005.1481.

[50] Jamal Jalilian-Marian and Xin-Nian Wang. Small x gluons in nuclei and hadrons. *Phys.Rev.*, D60:054016, 1999, hep-ph/9902411.

[51] I. Schienbein, J.Y. Yu, K. Kovarik, C. Keppel, J.G. Morfin, F. Olness, and J. Owens. PDF Nuclear Corrections for Charged and Neutral Current Processes. *Phys.Rev.*, D80:094004, 2009, 0907.2357.

[52] Adrian Dumitru, Dmitri E. Kharzeev, Eugene M. Levin, and Yasushi Nara. Gluon Saturation in pA Collisions at the LHC: KLN Model Predictions For Hadron Multiplicities. *Phys.Rev.*, C85:044920, 2012, 1111.3031.

[53] Javier L. Albacete, Adrian Dumitru, Hirotsugu Fujii, and Yasushi Nara. CGC predictions for p+Pb collisions at the LHC. 2012, 1209.2001.

[54] Bjoern Schenke, Sangyong Jeon, and Charles Gale. Anisotropic flow in $\sqrt{s} = 2.76$ TeV Pb+Pb collisions at the LHC. *Phys.Lett.*, B702:59–63, 2011, 1102.0575.

[55] Rainer J Fries and Sener Ozonder. (In preparation) Rapidity-Dependent Initial Energy Density in Heavy-Ion Collisions. August, 2013.

[56] R.J. Fries, J.I. Kapusta, and Y. Li. Near-fields and initial energy density in the color glass condensate model. 2006, nucl-th/0604054.

[57] Alex Kovner, Larry D. McLerran, and Heribert Weigert. Gluon production at high transverse momentum in the McLerran-Venugopalan model of nuclear structure functions. *Phys.Rev.*, D52:3809–3814, 1995, hep-ph/9505320.

[58] Alex Kovner, Larry D. McLerran, and Heribert Weigert. Gluon production from nonAbelian Weizsacker-Williams fields in nucleus-nucleus collisions. *Phys.Rev.*, D52:6231–6237, 1995, hep-ph/9502289.

[59] A. Makhlin. The Wedge form of relativistic dynamics. 2. The Gluons. 1996, hep-ph/9608261.

[60] Alex Krasnitz and Raju Venugopalan. Nonperturbative computation of gluon minijet production in nuclear collisions at very high-energies. *Nucl.Phys.*, B557:237, 1999, hep-ph/9809433.

[61] T. Lappi. Energy density of the glasma. *Phys.Lett.*, B643:11–16, 2006, hep-ph/0606207.

[62] Hirotsugu Fujii, Kenji Fukushima, and Yoshimasa Hidaka. Initial energy density and gluon distribution from the Glasma in heavy-ion collisions. *Phys.Rev.*, C79:024909, 2009, 0811.0437.

[63] M. Gyulassy and Larry D. McLerran. Yang-Mills radiation in ultrarelativistic nuclear collisions. *Phys.Rev.*, C56:2219–2228, 1997, nucl-th/9704034.

[64] J.P. Blaizot and Alfred H. Mueller. The Early Stage of Ultrarelativistic Heavy Ion Collisions. *Nucl.Phys.*, B289:847, 1987.

[65] Bjoern Schenke, Sangyong Jeon, and Charles Gale. (3+1)D hydrodynamic simulation of relativistic heavy-ion collisions. *Phys.Rev.*, C82:014903, 2010, 1004.1408.

Appendix A

Calculation of the Boundary Condition

In this Appendix, we show the derivation of the boundary condition given in Eq. (4.7).

In their seminal paper, Kovner *et al.* [57, 58] dealt with boost-invariant before- and after-fields. Here we will try to see if the existing calculations can be generalized to the case where before- and after-fields depend on the longitudinal coordinate $x_\parallel$ defined in Eq. (3.19). The goal here is to see whether the initial energy density given in Eq. (A.1) [59, 60, 61] could have any use in the non-boost-invariant case, although it was originally derived for the boost-invariant fields. In the $(\tau, \eta, \boldsymbol{x}_\perp)$ coordinate system, we have

$$\varepsilon(\tau = 0) = \lim_{\tau \to 0^+} \frac{1}{\tau} \frac{\mathrm{d}E}{\mathrm{d}^2\boldsymbol{x}_T \mathrm{d}\eta} = \frac{1}{2} \mathrm{Tr}\, F_{ij} F_{ij} + 4\, \mathrm{Tr}(A^\eta)^2. \tag{A.1}$$

Here the first term in Eq. (A.1) corresponds to the energy due to longitudinal magnetic fields whereas the second term corresponds to the energy due to longitudinal electric fields. So, at $\tau = 0$ after the interaction, all the fields are longitudinal and there is no transverse field. Of course, there are transverse fields in the receding nuclei after the collision. However, those fields go away as the nuclei recede from each other. We are only interested in the longitudinal fields that emerge as a result of interaction of the fields from both nuclei, $A^i_{1,2}$. Although both E^a and B^a fields are purely longitudinal right after the collision at $\tau = 0$, when we go to later times, transverse fields will emerge from these longitudinal fields due to the nonlinear nature of the classical Yang-Mills

equation (CYM). However, we are interested in the energy density at $\tau = 0$.

We start with generalizing the original ansatz [57, 58] by adding the $x_\parallel$ coordinate dependence to the before- and after-fields.

$$A^\pm = \pm\theta(x^+)\theta(x^-)\, x^\pm A(\tau, x_\parallel, \boldsymbol{x}_\perp) \tag{A.2}$$

$$A^i = \theta(x^-)\theta(-x^+)A_1^i(x_\parallel, \boldsymbol{x}_\perp) + \theta(x^+)\theta(-x^-)A_2^i(x_\parallel, \boldsymbol{x}_\perp) + \theta(x^+)\theta(x^-)A_\perp^i(\tau, x_\parallel, \boldsymbol{x}_\perp), \tag{A.3}$$

where $A(\tau, x_\parallel, \boldsymbol{x}_\perp)$ and $A_\perp(\tau, x_\parallel, \boldsymbol{x}_\perp)$ are the after-fields whereas $A_{1,2}^i(x_\parallel, \boldsymbol{x}_\perp)$ are the before-fields belonging to nuclei 1 and 2. Due to the $x_\parallel$-dependence, the fields are no longer boost-invariant. We will see whether this modification results in any change in the initial energy given in Eq. (A.1). The $x_\parallel$-dependent ansatz in Eqs. (A.2-A.3) still do satisfy the Schwinger gauge $x^-A^+ + x^+A^- = 0$.

Before- and after-fields are matched at $\tau = 0$ via the equation of motion

$$[D_\mu, F^{\mu\nu}] = J^\nu. \tag{A.4}$$

The sharp hyper-surface $\tau = 0$ refers to the light-cone i.e., $x^+ = 0$, $x^- = 0$ and the vertex $x^+ = x^- = 0$. In the original boost-invariant case, $[D_\mu, F^{\mu j}] = 0$ and $[D_\mu, F^{\mu\pm}] = J^\pm$ give rise to the following boundary conditions, respectively [57, 58]

$$A_\perp^i(\tau = 0, \boldsymbol{x}_\perp) = A_1^i(\boldsymbol{x}_\perp) + A_2^i(\boldsymbol{x}_\perp) \tag{A.5}$$

$$A(\tau = 0, \boldsymbol{x}_\perp) = \frac{ig}{2}[A_1^i(\boldsymbol{x}_\perp), A_2^i(\boldsymbol{x}_\perp)]. \tag{A.6}$$

Here we re-derive Eq. (A.5) for the $x_\parallel$-dependent case.

For regular solutions around the light-cone $\tau = \sqrt{2x^+x^-} = 0$, we have

$$\lim_{\substack{\epsilon\to 0\\ \delta\to 0}} \int_{-\epsilon}^{\epsilon} dx^+ \int_{-\delta}^{\delta} dx^- [D_\mu, F^{\mu j}] = 0, \tag{A.7}$$

or

$$\lim_{\substack{\epsilon\to 0\\ \delta\to 0}} \int_{-\epsilon}^{\epsilon} dx^+ \int_{-\delta}^{\delta} dx^- \Big([D_+, F^{+j}] + [D_-, F^{-j}] + [D_i, F^{ij}] \Big) = 0. \tag{A.8}$$

The identities below will be soon useful:

$$\lim_{\epsilon\to 0} \int_{-\epsilon}^{\epsilon} dx^+ \theta(x^+) = 0, \tag{A.9}$$

and

$$\lim_{\epsilon\to 0}\int_{-\epsilon}^{\epsilon} dx^+ \underbrace{\frac{\partial}{\partial x^+}\theta(x^+)}_{\delta(x^+)} = 1, \tag{A.10}$$

and

$$\frac{\partial}{\partial x}\theta(-x) = -\delta(x). \tag{A.11}$$

Any term in Eq. (A.8) which is not of the form

$$\lim_{\substack{\epsilon\to 0\\ \delta\to 0}}\int_{-\epsilon}^{\epsilon} dx^+ \int_{-\delta}^{\delta} dx^- \delta(x^+)\delta(x^-), \tag{A.12}$$

will vanish due to Eqs. (A.9-A.10). For example, any term such as $\theta(x^+)\theta(x^-)$ and $\theta(x^+)\delta(x^-)$ in Eq. (A.8) will vanish.

Now, the vector fields depending on $(x_\parallel, \boldsymbol{x}_\perp)$ are given as follows (The coefficient that is irrelevant for the calculation here is denoted by c).

$$\begin{aligned} F^{+-} &= \partial^+ A^- - \partial^- A^+ - ig[A^+, A^-] && \text{(A.13)}\\ &= \theta(x^+)A\left(-x^-\delta(x^-) - \theta(x^-)\right) - \theta(x^-)A\left(x^+\delta(x^+) + \theta(x^+)\right)\\ &\quad -c\underbrace{[A, A]}_{=0} + \text{terms including } \partial^\pm A && \text{(A.14)}\\ &= -2\theta(x^+)\theta(x^-)A - \theta(x^+)\delta(x^-)x^- A - \theta(x^-)\delta(x^+)x^+ A\\ &\quad + \text{terms including } \partial^\pm A. && \text{(A.15)} \end{aligned}$$

$$\begin{aligned} F^{+j} &= \partial^+ A^j - \partial^j A^+ - ig[A^+, A^j] && \text{(A.16)}\\ &= \delta(x^-)\theta(-x^+)A_1^j - \delta(x^-)\theta(x^+)A_2^j + \delta(x^-)\theta(x^+)A_\perp^i\\ &\quad \underbrace{-\partial^j A^+ - ig[A^+, A^j]}_{\delta(x^\pm)\text{ independent}} + \text{derivatives of } A \text{ and } A_\perp^i. && \text{(A.17)} \end{aligned}$$

$$\begin{aligned} \partial_+ F^{+j} &= -\delta(x^-)\delta(x^-)A_1^j - \delta(x^-)\delta(x^+)A_2^j + \delta(x^-)\delta(x^+)A_\perp^j\\ &\quad -\partial^j\left(\delta(x^+)\theta(x^-)x^+ A + \theta(x^+)\theta(x^-)A\right) && \text{(A.18)}\\ &\quad -ig\partial_+\left(\theta(x^-)\theta(x^+)x^+[A, A^j]\right)\\ &\quad + \text{derivatives of } A \text{ and } A_\perp^i. && \text{(A.19)} \end{aligned}$$

Note that the lines (A.18-A.19) will vanish when taking the limit $\lim\limits_{\substack{\epsilon\to 0\\ \delta\to 0}} \int_{-\epsilon}^{\epsilon} dx^+ \int_{-\delta}^{\delta} dx^-$.

$$\begin{aligned} F^{-j} &= \partial^- A^j - \partial^j A^- - ig[A^-, A^j] && \text{(A.20)}\\ &= -\delta(x^+)\theta(x^-)A_1^j + \delta(x^+)\theta(-x^-)A_2^j + \theta(x^-)\delta(x^+)A_\perp^i \\ &\quad \underbrace{-\partial^j A^- - ig[A^-, A^j]}_{\delta(x^\pm)\,\text{independent}} + \text{derivatives of } A \text{ and } A_\perp^i. && \text{(A.21)} \end{aligned}$$

$$\begin{aligned} \partial_- F^{-j} &= -\delta(x^+)\delta(x^-)A_1^j - \delta(x^+)\delta(x^-)A_2^j + \delta(x^-)\delta(x^+)A_\perp^j \\ &\quad + \text{terms that will vanish under } \lim_{\substack{\epsilon\to 0\\ \delta\to 0}} \int_{-\epsilon}^{\epsilon} dx^+ \int_{-\delta}^{\delta} dx^-. && \text{(A.22)} \end{aligned}$$

F^{ij} and $\partial_i F^{ij}$ do not include any term like $\delta(x^-)\delta(x^+)$, so we will not write them. Equation (A.8) can be written as

$$\begin{aligned} \lim_{\substack{\epsilon\to 0\\ \delta\to 0}} \int_{-\epsilon}^{\epsilon} dx^+ \int_{-\delta}^{\delta} dx^- \Big(& \partial_+ F^{+j} - \cancel{ig[A_+, F^{+j}]} \\ & + \partial_- F^{-j} - \cancel{ig[A_-, F^{-j}]} \Big) = 0, \end{aligned} \qquad \text{(A.23)}$$

which yields

$$\begin{aligned} \lim_{\substack{\epsilon\to 0\\ \delta\to 0}} \int_{-\epsilon}^{\epsilon} dx^+ \int_{-\delta}^{\delta} dx^- \Big[& -2\delta(x^+)\delta(x^-)\Big(A_1^j(x_\parallel, \boldsymbol{x}_\perp) \\ & + A_2^j(x_\parallel, \boldsymbol{x}_\perp) - A_\perp^j(\tau, x_\parallel, \boldsymbol{x}_\perp)\Big)\Big] = 0. \end{aligned} \qquad \text{(A.24)}$$

Some terms in Eq. (A.23) have been canceled because they did not include a term $\delta(x^-)\delta(x^+)$. Eq. (A.24) gives

$$A_\perp^j(\tau = 0, x_\parallel = 0, \boldsymbol{x}_\perp) = A_1^j(x_\parallel = 0, \boldsymbol{x}_\perp) + A_2^j(x_\parallel = 0, \boldsymbol{x}_\perp), \qquad \text{(A.25)}$$

where $x_\parallel = 0$ when $x^+ = x^- = 0$. Here Eq. (A.25) is actually the same boundary condition as for the boost-invariant case [57, 58]. Although we started with nuclei extended in the longitudinal direction, because of the sharp interaction surface $\tau = 0$ imposed, we found a boundary condition for two partons that interact at $\tau = 0$ rather than a boundary condition for two extended nuclei (see Fig. A.1). The problem actually originates from Eq. (A.24): The limiting procedure destroys the longitudinal dependence.

When nuclei have a longitudinal extent, the delta functions should be smeared and the limits $\epsilon, \delta \to 0$ should not be taken. Despite this subtle point, we will use the boundary condition in Eq. (A.25) as an approximation. See the discussion below Eq. (4.8).

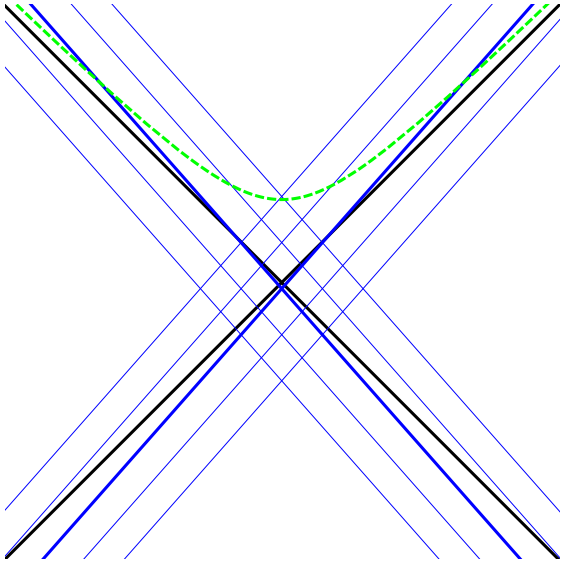

Figure A.1: Light-cone picture of the interaction of two nuclei. The thick black lines show the light-cone coordinates x^+ and x^-. Note that the transverse direction $\boldsymbol{x}_\perp$ does not appear in this two-dimensional plot. The nuclei are comprised of partons shown as blue lines. The partons are not parallel to the light-cone because, in our treatment, the nuclei have speed $\beta < c$. The thick blue lines correspond to the partons exactly at the center of the nuclei ($x_\parallel = 0$). Each parton from a nucleus interacts with all of the partons from the other nucleus, albeit at different times. One such time $\tau' > 0$ is shown with the green dashed line. The latest interaction occurs on the green hyper-surface by the partons from the rear of both the nuclei. The partons in the front of the nuclei interact even before $\tau = 0$. Imposing the $\tau = 0$ as the interaction hyper-surface, we find boundary condition for the partons that interact on $\tau = 0$. These two partons interact at the vertex, and they are shown with thick blue lines.

Appendix B

Derivation of the Initial Energy Density

In this Appendix, we derive the energy density given in Eq. (4.9) as

$$\varepsilon(\tau=0) = \frac{1}{2}\mathrm{Tr}\, F_{ij}F_{ij} + \mathrm{Tr}(E^{\eta})^2, \tag{B.1}$$

and Eq. (4.10)

$$\begin{aligned}\varepsilon(\tau=0) = \frac{1}{2}g^2 f^{abc}f^{ade}[&\langle A_i^b A_i^d\rangle\langle A_j^c A_j^e\rangle \\ &+ \langle A_i^b A_j^e\rangle\langle A_j^c A_i^d\rangle + \langle A_i^b A_j^d\rangle\langle A_i^c A_j^e\rangle].\end{aligned} \tag{B.2}$$

For Eq. (B.1), we follow [59, 60, 61, 62]. The Hamiltonian in $(\tau, \eta, \boldsymbol{x}_\perp)$ coordinates can be written as[1] ($\tau = \sqrt{t^2 - z^2}$ and $\eta = 1/2 \ln((t+z)/t-z)$)

$$H = \int d^2\boldsymbol{x}_\perp\, d\eta\, \tau \left(\frac{1}{4}F_{ij}F_{ij} + \frac{1}{2}p^\eta p^\eta + \frac{1}{2\tau^2}F_{\eta i}F_{\eta i} + \frac{1}{2\tau^2}p^r p^r\right). \tag{B.3}$$

Note that η is a dimensionless coordinate and $d^2\boldsymbol{x}_\perp\,\tau$ is three dimensional. The canonical momenta are

$$p^\tau = 0,\;\; p^\eta = \frac{1}{\tau}F_{\tau\eta} = \frac{1}{\tau}\frac{\partial}{\partial\tau}A_\eta,\;\; p_r = \tau F_{\tau r} = \tau\frac{\partial}{\partial\tau}A_r. \tag{B.4}$$

Also from [62],

$$E^\eta = \frac{1}{\tau}\frac{\partial}{\partial\tau}A_\eta = p^\eta. \tag{B.5}$$

[1] Here η is the space-time rapidity. Elsewhere we use η_s for it.

By using $A_\eta = -\tau^2 A^\eta$, the longitudinal electric field can be written as

$$E^\eta = -\frac{1}{\tau}\left(2\tau A^\eta + \tau^2 \frac{\partial}{\partial \tau} A^\eta\right). \tag{B.6}$$

By using the condition [60]

$$\frac{\partial}{\partial \tau} A^\eta\Big|_{\tau=0} = 0, \tag{B.7}$$

the electric field at $\tau = 0$ can be written as

$$E^\eta = -2A^\eta. \tag{B.8}$$

At $\tau = 0$, there are only longitudinal magnetic and electric fields, so the last two terms in Eq. (B.3) are zero. Hence, the Hamiltonian at $\tau = 0$ becomes

$$H\Big|_{\tau=0} = \int d^2\boldsymbol{x}_\perp \, d\eta \, \tau \left(\frac{1}{4} F_{ij} F_{ij} + \frac{1}{2} E^\eta E^\eta\right). \tag{B.9}$$

So far, the summed color indices have been suppressed. To recover the $SU(3)$ matrices t^a, we can use $1/2 \to \mathrm{Tr}$. This substitution rule can be derived from $\mathrm{Tr}[t^a t^b] = \delta_{ab}/2$. Finally, we find

$$H\Big|_{\tau=0} = \int d^2\boldsymbol{x}_\perp \, d\eta \, \tau \left(\frac{1}{2} \mathrm{Tr} F_{ij} F_{ij} + 4\mathrm{Tr}(A^\eta)^2\right). \tag{B.10}$$

Now we turn to the derivation of Eq. (4.10). Below, we will use the boundary condition

$$A^i_\perp(\tau = 0, \boldsymbol{x}_\perp) = A^i_1(\boldsymbol{x}_\perp) + A^i_2(\boldsymbol{x}_\perp), \tag{B.11}$$

where 1 and 2 refers to different nuclei (The calculations here are done at $\tau = 0$). Let us start with the term $\langle \frac{1}{2}\mathrm{Tr} F_{ij} F_{ij}\rangle = \langle \frac{1}{4} F^a_{ij} F^a_{ij}\rangle$.

The field strength tensor is given by

$$F^a_{ij} = \partial_i(A^a_{1j} + A^a_{2j}) - \partial_j(A^a_{1i} + A^a_{2i}) + g f^{abc}(A^b_{1i} + A^b_{2i})(A^c_{1j} + A^c_{2j}). \tag{B.12}$$

Only the last term with g corresponds to the longitudinal field produced via interaction, so we will omit the first two terms with the derivatives in Eq. (B.12). There is no correlation between the two nuclei prior to collision, so $\langle A_1 A_2\rangle = 0$. As a consequence of this, we have, for example,

$$\langle A_1 A_1 A_1 A_2\rangle \to \langle A_1 A_1\rangle \cancel{\langle A_1 A_2\rangle} = 0. \tag{B.13}$$

Also, any term including three fields averaged vanishes because we are in the Gaussian approximation where $\langle A_{1,2}\rangle = 0$; i.e., $\langle A_1 A_1 A_1\rangle \to \langle A_1 A_1\rangle\cancel{\langle A_1\rangle} = 0$. Now we calculate

$$\begin{aligned}\langle\frac{1}{4}F^a_{ij}F^a_{ij}\rangle &= \frac{1}{4}g^2 f^{abc}f^{ade}(A^b_{i1}A^c_{j1}A^d_{i1}A^e_{j1} + \cancel{A^b_{j2}A^c_{j1}A^d_{i1}A^e_{j1}} + \cancel{A^b_{j1}A^c_{j2}A^d_{i1}A^e_{j1}}\\
&\quad + A^b_{i2}A^c_{j2}A^d_{i1}A^e_{j1} + \cancel{A^b_{i1}A^c_{j1}A^d_{i2}A^e_{j1}} + A^b_{i2}A^c_{j1}A^d_{i2}A^e_{j1}\\
&\quad + A^b_{i1}A^c_{j2}A^d_{i2}A^e_{j1} + \cancel{A^b_{i2}A^c_{j2}A^d_{i2}A^e_{j1}} + \cancel{A^b_{i1}A^c_{j1}A^d_{i1}A^e_{j2}}\\
&\quad + A^b_{i2}A^c_{j1}A^d_{i1}A^e_{j2} + A^b_{i1}A^c_{j2}A^d_{i1}A^e_{j2} + \cancel{A^b_{i2}A^c_{j2}A^d_{i1}A^e_{j2}}\\
&\quad + A^b_{i1}A^c_{j1}A^d_{i2}A^e_{j2} + \cancel{A^b_{i2}A^c_{j1}A^d_{i2}A^e_{j2}} + \cancel{A^b_{i1}A^c_{j2}A^d_{i2}A^e_{j2}}\\
&\quad + A^b_{i2}A^c_{j2}A^d_{i2}A^e_{j2}). \qquad \text{(B.14)}\end{aligned}$$

Here all of fields are functions of only one variable $\boldsymbol{x} = (x_\parallel, \boldsymbol{x}_\perp)$, hence $\varepsilon \equiv \varepsilon(x_\parallel, \boldsymbol{x}_\perp)$.

In the Gaussian approximation, we have

$$\langle 1234\rangle = \langle 12\rangle\langle 34\rangle + \langle 13\rangle\langle 24\rangle + \langle 14\rangle\langle 32\rangle. \qquad \text{(B.15)}$$

Below, we will use abbreviated notation, for example, $\langle b1i\, c1j\rangle \equiv \langle A^b_{1i}A^c_{1j}\rangle$. Some terms, such as $f^{abc}\langle A^b_{1i}A^c_{1j}\rangle$, will vanish since f^{abc} is antisymmetric and

$$\langle A^b_i A^c_j\rangle \propto \delta^{bc}\phi(x, \boldsymbol{q}_\perp), \qquad \text{(B.16)}$$

where $\phi(x, \boldsymbol{q}_\perp)$ is the unintegrated gluon distribution (UGD) given in Eq. (3.23) . So, $\langle\frac{1}{4}F^a_{ij}F^a_{ij}\rangle$ becomes

$$\begin{aligned}\langle\frac{1}{4}F^a_{ij}F^a_{ij}\rangle &= \frac{1}{4}g^2 f^{abc}f^{ade}[\cancel{\langle b1i\, c1j\rangle\langle d1i\, e1j\rangle} + \langle b1i\, d1i\rangle\langle c1j\, e1j\rangle\\
&\quad + \langle b1i\, e1j\rangle\langle c1j\, d1i\rangle + \cancel{\langle b2i\, c2j\rangle\langle d1i\, e1j\rangle}\\
&\quad + \langle b1i\, e1j\rangle\langle c2j\, d2i\rangle + \langle b2i\, e2j\rangle\langle c1j\, d1i\rangle\\
&\quad + \cancel{\langle b1i\, c1j\rangle\langle d2i\, e2j\rangle} + \cancel{\langle b2i\, c2j\rangle\langle d2i\, e2j\rangle}\\
&\quad + \langle b2i\, d2i\rangle\langle c2j\, e2j\rangle + \langle b2i\, e2j\rangle\langle c2j\, d2i\rangle] \qquad \text{(B.17)}\\
&= \frac{1}{4}g^2 f^{abc}f^{ade}[2\langle b1i\, d1i\rangle\langle c1j\, e1j\rangle + \langle b1i\, e1j\rangle\langle c1j\, d1i\rangle]. \qquad \text{(B.18)}\end{aligned}$$

If both nuclei are the same, we get

$$\langle\frac{1}{4}F^a_{ij}F^a_{ij}\rangle = \frac{1}{2}g^2 f^{abc}f^{ade}[\langle A^b_i A^d_i\rangle\langle A^c_j A^e_j\rangle + \langle A^b_i A^e_j\rangle\langle A^c_j A^d_i\rangle]. \qquad \text{(B.19)}$$

Let us turn to the second term (chromo-electric part) of Eq. (B.10). By using the boundary condition given as

$$A^{\eta}(x_{\parallel}, \boldsymbol{x}_{\perp})\Big|_{\tau=0} = \frac{ig}{2}[A_1^i(x_{\parallel}, \boldsymbol{x}_{\perp}), A_2^i(x_{\parallel}, \boldsymbol{x}_{\perp})], \tag{B.20}$$

we find

$$A^{a\,\eta} t^a = \frac{ig}{2} A_1^{b\,i} A_2^{c\,i} \underbrace{[t^b, t^c]}_{if^{abc}t^a}, \tag{B.21}$$

or

$$A^{a\,\eta} = \frac{-g}{2} f^{abc} A_1^{b\,i} A_2^{c\,i}. \tag{B.22}$$

The second part of Eq. (B.10) becomes

$$\begin{aligned}
\langle 4\,\mathrm{Tr}(A^{\eta})^2 \rangle &= 4\mathrm{Tr}[t^a t^b] \langle A^{a\,\eta} A^{b\,\eta} \rangle = 2\langle A^{a\,\eta} A^{a\,\eta} \rangle & \text{(B.23)} \\
&= 2\left(\frac{-g}{2}\right)^2 f^{abc} f^{ade} \langle A_1^{b\,i} A_2^{c\,i} A_1^{d\,j} A_2^{e\,j} \rangle & \text{(B.24)} \\
&= \frac{g^2}{2} f^{abc} f^{ade} \langle A_1^{b\,i} A_1^{d\,j} \rangle \langle A_2^{c\,i} A_2^{e\,j} \rangle & \text{(B.25)} \\
&= \frac{g^2}{2} f^{abc} f^{ade} \langle A_i^b A_j^d \rangle \langle A_i^c A_j^e \rangle, & \text{(B.26)}
\end{aligned}$$

where, in the last line, we assumed nuclei 1 and 2 are the same. Finally, the energy density at $\tau = 0$ becomes

$$\begin{aligned}
\varepsilon(\tau = 0) = \frac{1}{2} g^2 f^{abc} f^{ade} [&\langle A_i^b A_i^d \rangle \langle A_j^c A_j^e \rangle \\
&+ \langle A_i^b A_j^e \rangle \langle A_j^c A_i^d \rangle + \langle A_i^b A_j^d \rangle \langle A_i^c A_j^e \rangle].
\end{aligned} \tag{B.27}$$

Appendix C

Three-Dimensional Ansatz and Energy Density per Unit Rapidity

C.1 Calculation of the Three-Dimensional Ansatz

In this Appendix, we derive the three dimensional (x-dependent) ansatz given in Eq. (4.12).

The correlation function of the vector potential[1] $\langle A_i^a(q_\parallel;\boldsymbol{q}_\perp)A_i^a(-q_\parallel;-\boldsymbol{q}_\perp)\rangle$ is calculated in [6]. Our first goal is finding the most general correlation function with different color and transverse coordinate indices as well as the most general momentum dependency, i.e., $\langle A_i^a(q_\parallel;\boldsymbol{q}_\perp)A_j^b(p_\parallel;\boldsymbol{p}_\perp)\rangle$ Then we will use this ansatz to calculate $\varepsilon(\tau=0)$.

The gluon parton distribution function (PDF) is given by

$$xg_A(x,Q^2)=\int^{Q^2}\mathrm{d}^2\boldsymbol{q}_\perp\left(x\frac{dN}{dx\,d^2\boldsymbol{q}_\perp}\right)=\int^{Q^2}\mathrm{d}^2\boldsymbol{q}_\perp\phi(x,\boldsymbol{q}_\perp^2), \tag{C.1}$$

where $\langle A_i^a(q_\parallel;\boldsymbol{q}_\perp)A_i^a(-q_\parallel;-\boldsymbol{q}_\perp)\rangle$ is proportional to the unintegrated gluon distribution (UGD) $\phi(x,\boldsymbol{q}_\perp)$ (see Eq. 4.3).

In 3dMVn, the charge density ρ and consequently the before- and after-fields A_i^a depend on the longitudinal coordinate $x_\parallel$. The conjugate momentum of the longitudinal coordinate is $q_\parallel$, which is related to x via

$$x\equiv\frac{q_\parallel}{m}, \tag{C.2}$$

[1] Summation over the color and spatial indices are implied.

where m is the nucleon mass. Hence

$$\phi(x,\boldsymbol{q}_\perp^2) = x\frac{dN}{dxd^2\boldsymbol{q}_\perp} = q_\parallel \frac{dN}{dq_\parallel d\boldsymbol{q}_\perp}. \tag{C.3}$$

From Eq. (4.3), we get

$$\frac{dN}{dq_\parallel d^2\boldsymbol{q}_\perp} \equiv \frac{q_\parallel}{4\pi^3}\langle A_i^a(q_\parallel;\boldsymbol{q}_\perp)A_i^a(-q_\parallel;-\boldsymbol{q}_\perp)\rangle, \tag{C.4}$$

from which we obtain (by using $x \equiv q_\parallel/m$)

$$\langle A_i^a(q_\parallel;\boldsymbol{q}_\perp)A_i^a(-q_\parallel;-\boldsymbol{q}_\perp)\rangle = \frac{4\pi^3}{m^2x}\underbrace{\frac{dN}{dxd^2\boldsymbol{q}_\perp}}_{\phi(x,\boldsymbol{q}_\perp^2)/x} = \frac{4\pi^3}{m^2x^2}\,\phi(x,\boldsymbol{q}_\perp^2). \tag{C.5}$$

Let us pause for a moment and look at the dimensions (for $\hbar = c = 1$).

$$[\rho(\boldsymbol{x})] = 1/\mathrm{fm}^3, \tag{C.6}$$

$$[A(\boldsymbol{x})] = [A(x_\parallel,\boldsymbol{x}_\perp)] = 1/\mathrm{fm}\ \text{(see Eqs. (5.5) and (5.7) in [6])}, \tag{C.7}$$

$$[A(\boldsymbol{q})] = [A(q_\parallel,\boldsymbol{q}_\perp)] = 1/\mathrm{GeV}^2 \quad \left(\text{from } A(\boldsymbol{q}) \propto \int d^3x\, A(\boldsymbol{x})\right), \tag{C.8}$$

$$\left[\frac{dN}{dq_\parallel d^2\boldsymbol{q}_\perp}\right] = 1/\mathrm{GeV}^3 \ \text{(from Eq. } (C.4)), \tag{C.9}$$

$$[\phi(x,\boldsymbol{q}_\perp)] = \left[x\frac{dN}{dxd^2\boldsymbol{q}_\perp}\right] = 1/\mathrm{GeV}^2 \ \text{(from Eq. } (C.3)). \tag{C.10}$$

Before constructing the three-dimensional ansatz, we quote the two-dimensional ansatz from [61], which is valid when the colliding nuclei are taken to be infinitely thin and the UGD ($G(\boldsymbol{p}_\perp)$ here) is independent of x

$$\langle A_i^a(\boldsymbol{p}_\perp)A_j^b(\boldsymbol{q}_\perp)\rangle \equiv (2\pi)^2\delta^{ab}\delta^2(\boldsymbol{p}_\perp+\boldsymbol{q}_\perp)\frac{p_{\perp i}p_{\perp j}}{\boldsymbol{p}_\perp^2}G(\boldsymbol{p}_\perp). \tag{C.11}$$

Our goal here is constructing a similar ansatz which would be valid when the nuclei have thickness in the longitudinal direction and consequently when the UGDs depend on x. There are two things to be dealt with: i) The MV and 3dMVn UGDs have different dimensions, so one needs to be cautious. ii) The ansatz in [61] is for the 2D case. In the 3D case, we need to have another delta function for the longitudinal coordinate.

Let us make an ansatz for $\delta(p_\parallel+q_\parallel)\delta^2(\boldsymbol{p}_\perp+\boldsymbol{q}_\perp)$ dependence. The delta function of the form $\delta(\boldsymbol{p}_\perp+\boldsymbol{q}_\perp)$ implies translational invariance on the transverse plane, in other

words, $\boldsymbol{x}_\perp$ independence. This may not be obvious. Here is why this is true: If we think of the Fourier transform of the fields in Eq. (B.27), we get $\delta^2(\boldsymbol{p}_\perp+\boldsymbol{q}_\perp)\delta^2(\boldsymbol{k}_\perp+\boldsymbol{l}_\perp)$ and upon integration, these delta functions kill the term $\exp[i\,(\boldsymbol{p}_\perp+\boldsymbol{q}_\perp+\boldsymbol{k}_\perp+\boldsymbol{l}_\perp)\cdot\boldsymbol{x}_\perp]$, hence the $\boldsymbol{x}_\perp$-dependence is lost. As a result, the translational invariance comes in and we get homogeneity in the transverse plane.

Note that the 2D ansatz in Eq. (C.11) does not include $\delta(p_\parallel+q_\parallel)$; this term is special to the 3D case. The $\delta(p_\parallel+q_\parallel)$ should be justified in the case of the cylindrical nucleus because there is translational invariance also in the longitudinal direction, in the rest frame coordinate $x_\parallel$.

Therefore, we postulate that

$$\langle A_i^a(q_\parallel;\boldsymbol{q}_\perp)A_i^a(p_\parallel;\boldsymbol{p}_\perp)\rangle=\delta_{p_\parallel,-q_\parallel}\delta_{p_x,-q_x}\delta_{p_y,-q_y}\underbrace{\langle A_i^a(q_\parallel;\boldsymbol{q}_\perp)A_i^a(-q_\parallel;-\boldsymbol{q}_\perp)\rangle}_{\frac{4\pi^3}{m^2x^2}\,\phi(x,\boldsymbol{q}_\perp^2)}. \tag{C.12}$$

Note that the Kronecker delta is dimensionless, hence the dimensions of both sides of Eq. (C.12) is correct. Now, let's use the well-known relation

$$\delta^3(\boldsymbol{p}-\boldsymbol{q})\Leftrightarrow\frac{V}{(2\pi)^3}\delta_{\boldsymbol{p},\boldsymbol{q}}, \tag{C.13}$$

where V is volume and $\boldsymbol{p}=(p_\parallel,\boldsymbol{p}_\perp)$. Equation (C.12) becomes

$$\langle A_i^a(q_\parallel;\boldsymbol{q}_\perp)A_i^a(p_\parallel;\boldsymbol{p}_\perp)\rangle=\frac{1}{V}(2\pi)^3\delta(p_\parallel+q_\parallel)\delta^2(\boldsymbol{p}_\perp+\boldsymbol{q}_\perp)\langle A_i^a(q_\parallel;\boldsymbol{q}_\perp)A_i^a(-q_\parallel;-\boldsymbol{q}_\perp)\rangle, \tag{C.14}$$

where $V=\pi R_A^2h$ is the volume of the nucleus, R_A is the nuclear radius and h is the length of the cylindrical nucleus in its rest frame. Dimensions of both sides of Eq. (C.14) match since the dimension of $(2\pi)^3\delta(p_\parallel+q_\parallel)\delta^2(\boldsymbol{p}_\perp+\boldsymbol{q}_\perp)$ is $1/\mathrm{GeV}^3$ and the dimension of $1/V$ is GeV^3. Both $\langle A_i^a(q_\parallel;\boldsymbol{q}_\perp)A_i^a(p_\parallel;\boldsymbol{p}_\perp)\rangle$ and $\langle A_i^a(q_\parallel;\boldsymbol{q}_\perp)A_i^a(-q_\parallel;-\boldsymbol{q}_\perp)\rangle$ are of the same dimensions. One may raise an objection saying that $1/V$ term did not arise in the 2D ansatz in Eq. (C.11). This is true, there isn't any $1/\pi R_A^2$ in the 2D ansatz. On the other hand, the area πR_A^2 is included in the definition of the PDF in the 2D case [61]

$$xg_A(x,Q^2)=R_A^2(N_\mathrm{c}^2-1)\int^{Q^2}\frac{d^2\boldsymbol{k}_\perp}{(2\pi)^2}G(\boldsymbol{k}_\perp), \tag{C.15}$$

where the subscript A in xg_A is to emphasize that this is the PDF of the whole nucleus. However, in the 3D case, the definition of PDF does not include any area/volume factor [40, 6]

$$xg_A(x,Q^2) = \int^{Q^2} d^2\boldsymbol{k}_\perp \underbrace{x\frac{dN}{dxd^2\boldsymbol{k}_\perp}}_{\phi(x,\boldsymbol{k}_\perp)}, \tag{C.16}$$

where $\phi(x,\boldsymbol{k}_\perp)$ is the 3dMVn UGD here. So, the 2D UGD $G(\boldsymbol{p}_\perp)$ defined in [61] is actually the UGD per unit area. The correspondence between these two UGDs roughly goes like

$$G(\boldsymbol{k}_\perp) \leftrightarrow \frac{1}{\pi R_A^2}\phi(x,\boldsymbol{k}_\perp). \tag{C.17}$$

Now we shall establish the most general color index structure of the 3D ansatz. Suppose $A^aA^b = c\delta^{ab}$, then,

$$\delta^{ab}A^aA^b = A^aA^a = c\delta^{ab}\delta^{ab} = c(N_c^2-1), \tag{C.18}$$

where $\delta^{ab}\delta^{ab} = N_c^2 - 1 = 8$. Hence,

$$A^aA^b = c\delta^{ab} = \frac{\delta^{ab}}{N_c^2-1}A^dA^d. \tag{C.19}$$

Equation (C.14) now turns into

$$\begin{aligned}\langle A_i^a(q_\parallel;\boldsymbol{q}_\perp)A_i^b(p_\parallel;\boldsymbol{p}_\perp)\rangle &= \frac{\delta^{ab}}{N_c^2-1}\frac{1}{V}(2\pi)^3\delta(p_\parallel+q_\parallel)\delta^2(\boldsymbol{p}_\perp+\boldsymbol{q}_\perp)\\ &\quad\times\langle A_i^a(q_\parallel;\boldsymbol{q}_\perp)A_i^a(-q_\parallel;-\boldsymbol{q}_\perp)\rangle,\end{aligned} \tag{C.20}$$

which can be written in terms of the UGD as

$$\langle A_i^a(q_\parallel;\boldsymbol{q}_\perp)A_i^b(p_\parallel;\boldsymbol{p}_\perp)\rangle = \frac{\delta^{ab}}{N_c^2-1}\frac{1}{V}(2\pi)^3\delta(p_\parallel+q_\parallel)\delta^2(\boldsymbol{p}_\perp+\boldsymbol{q}_\perp)\frac{4\pi^3}{m^2x^2}\,\phi(x,\boldsymbol{q}_\perp^2). \tag{C.21}$$

Finally, we found an ansatz that would give $\langle A_i^a(q_\parallel;\boldsymbol{q}_\perp)A_i^b(p_\parallel;\boldsymbol{p}_\perp)\rangle$ in terms of $\langle A_i^a(q_\parallel;\boldsymbol{q}_\perp)A_i^a(-q_\parallel;-\boldsymbol{q}_\perp)\rangle$, or $\phi(x,\boldsymbol{q}_\perp^2)$. However, we are not done yet. We need the

most general correlator with i,j indices, i.e., $\langle A_i^a(q_\parallel;\boldsymbol{q}_\perp)A_j^b(p_\parallel;\boldsymbol{p}_\perp)\rangle$. Based on the existing rotational symmetry[2] on the transverse plane of the nucleus, we make the ansatz

$$\begin{aligned}\langle A_i^a(q_\parallel;\boldsymbol{q}_\perp)A_j^b(p_\parallel;\boldsymbol{p}_\perp)\rangle &= \frac{\delta^{ab}}{N_{\rm c}^2-1}\frac{1}{V}(2\pi)^3\delta(p_\parallel+q_\parallel)\delta^2(\boldsymbol{p}_\perp+\boldsymbol{q}_\perp)\\ &\quad\times\frac{4\pi^3}{m^2x^2}\phi(x,p_T)\frac{p_ip_j}{\boldsymbol{p}_\perp^2},\end{aligned}\tag{C.22}$$

where the i,j coordinates correspond to the transverse coordinates. Here $p_{i,j}$ are actually $p_{\perp i,j}$, but we dropped "$\perp$" for convenience. By using $x=p_\parallel/m$, we finally obtain

$$\begin{aligned}\langle A_i^a(q_\parallel;\boldsymbol{q}_\perp)A_j^b(p_\parallel;\boldsymbol{p}_\perp)\rangle &= \frac{\delta^{ab}}{N_{\rm c}^2-1}\frac{1}{V}(2\pi)^3\delta(p_\parallel+q_\parallel)\delta^2(\boldsymbol{p}_\perp+\boldsymbol{q}_\perp)\\ &\quad\times\frac{4\pi^3}{p_\parallel^2}\phi(p_\parallel,\boldsymbol{p}_\perp)\frac{p_ip_j}{\boldsymbol{p}_\perp^2}.\end{aligned}\tag{C.23}$$

This is the *the* 3D ansatz.

C.2 Calculation of Energy Density per Rapidity

In this section we shall derive Eq. (4.15). For that purpose, let us substitute the 3D ansatz given in Eq. (C.23) in the energy expression given in Eq. (4.10) as

$$\varepsilon(\tau=0)=\frac{1}{2}g^2f^{abc}f^{ade}\left[\langle A_i^bA_i^d\rangle\langle A_j^cA_j^e\rangle+\langle A_i^bA_j^e\rangle\langle A_j^cA_i^d\rangle+\langle A_i^bA_j^d\rangle\langle A_i^cA_j^e\rangle\right].\tag{C.24}$$

Before the substitution, let us list the identities we will need soon. Repeating Eq. (C.21) here (also using $x=p_\parallel/m$)

$$\langle A_i^a(q_\parallel;\boldsymbol{q}_\perp)A_i^b(p_\parallel;\boldsymbol{p}_\perp)\rangle=\frac{\delta^{ab}}{N_{\rm c}^2-1}\frac{1}{V}(2\pi)^3\delta(p_\parallel+q_\parallel)\delta^2(\boldsymbol{p}_\perp+\boldsymbol{q}_\perp)\frac{4\pi^3}{p_\parallel^2}\,\phi(p_\parallel,\boldsymbol{p}_\perp).\tag{C.25}$$

Contracting Eq. (C.25) with δ^{ab}

$$\langle A_i^a(q_\parallel;\boldsymbol{q}_\perp)A_i^a(p_\parallel;\boldsymbol{p}_\perp)\rangle=\frac{1}{V}(2\pi)^3\delta(p_\parallel+q_\parallel)\delta^2(\boldsymbol{p}_\perp+\boldsymbol{q}_\perp)\frac{4\pi^3}{p_\parallel^2}\,\phi(p_\parallel,\boldsymbol{p}_\perp),\tag{C.26}$$

[2] Note for the pedant: The most general rotationally invariant tensor is $c_1\delta_{ij}+c_2p_ip_j/\boldsymbol{p}_\perp^2$ The results, however, are independent of whether one uses this full structure or simply $p_ip_j/\boldsymbol{p}_\perp^2$. In the 2D case in [61] also only $p_ip_j/\boldsymbol{p}_\perp^2$ is used.

where $\delta^{ab}\delta^{ab} = N_c^2 - 1$. Also contracting Eq. (C.23) with δ^{ab}

$$\langle A_i^a(q_\parallel;\boldsymbol{q}_\perp)A_j^a(p_\parallel;\boldsymbol{p}_\perp)\rangle = \frac{1}{V}(2\pi)^3\delta(p_\parallel+q_\parallel)\delta^2(\boldsymbol{p}_\perp+\boldsymbol{q}_\perp) \times\frac{4\pi^3}{p_\parallel^2}\phi(p_\parallel,\boldsymbol{p}_\perp)\frac{p_ip_j}{\boldsymbol{p}_\perp^2}. \tag{C.27}$$

Now we are ready for the calculation. The three-dimensional momentum vector is defined as $\boldsymbol{p} = (p_\parallel, \boldsymbol{p}_\perp)$.

The first term in Eq. (C.24)

$$f^{abc}f^{ade}\langle A_i^bA_i^d\rangle\langle A_j^cA_j^e\rangle = f^{abc}f^{ade}\int\frac{d^3\boldsymbol{p}}{(2\pi)^3}\frac{d^3\boldsymbol{q}}{(2\pi)^3}\frac{d^3\boldsymbol{k}}{(2\pi)^3}\frac{d^3\boldsymbol{l}}{(2\pi)^3}e^{i(\boldsymbol{p}+\boldsymbol{q}+\boldsymbol{k}+\boldsymbol{l})\cdot\boldsymbol{x}} \times\langle A_i^b(p_\parallel,\boldsymbol{p}_\perp)A_i^d(q_\parallel,\boldsymbol{q}_\perp)\rangle\langle A_j^c(k_\parallel,\boldsymbol{k}_\perp)A_j^e(l_\parallel,\boldsymbol{l}_\perp)\rangle \tag{C.28}$$

$$= \underbrace{f^{abc}f^{ade}\delta^{bd}\delta^{ce}}_{N_c(N_c^2-1)}\frac{1}{(N_c^2-1)^2}\frac{1}{V^2}\int\frac{d^3\boldsymbol{p}}{(2\pi)^3}\frac{d^3\boldsymbol{q}}{(2\pi)^3}\frac{d^3\boldsymbol{k}}{(2\pi)^3}\frac{d^3\boldsymbol{l}}{(2\pi)^3}\,e^{i(\boldsymbol{p}+\boldsymbol{q}+\boldsymbol{k}+\boldsymbol{l})\cdot\boldsymbol{x}} \times(2\pi)^3\delta(p_\parallel+q_\parallel)\delta^2(\boldsymbol{p}_\perp+\boldsymbol{q}_\perp)(2\pi)^3\delta(k_\parallel+l_\parallel)\delta^2(\boldsymbol{k}_\perp+\boldsymbol{l}_\perp) \times\frac{4\pi^3}{p_\parallel^2}\phi(p_\parallel,\boldsymbol{p}_\perp)\,\frac{4\pi^3}{k_\parallel^2}\phi(k_\parallel,\boldsymbol{k}_\perp) \tag{C.29}$$

$$= \frac{N_c}{(N_c^2-1)}\frac{1}{V^2}\int\frac{d^2\boldsymbol{p}_\perp}{(2\pi)^2}\frac{d^2\boldsymbol{k}_\perp}{(2\pi)^2}\frac{dp_\parallel}{(2\pi)}\frac{dk_\parallel}{(2\pi)} \times\frac{4\pi^3}{p_\parallel^2}\phi(p_\parallel,\boldsymbol{p}_\perp)\,\frac{4\pi^3}{k_\parallel^2}\phi(k_\parallel,\boldsymbol{k}_\perp). \tag{C.30}$$

The second term in Eq. (C.24)

$$f^{abc}f^{ade}\langle A_i^bA_j^e\rangle\langle A_j^cA_i^d\rangle = f^{abc}f^{ade}\int\frac{d^3\boldsymbol{p}}{(2\pi)^3}\frac{d^3\boldsymbol{q}}{(2\pi)^3}\frac{d^3\boldsymbol{k}}{(2\pi)^3}\frac{d^3\boldsymbol{l}}{(2\pi)^3}e^{i(\boldsymbol{p}+\boldsymbol{q}+\boldsymbol{k}+\boldsymbol{l})\cdot\boldsymbol{x}} \times\langle A_i^b(p_\parallel,\boldsymbol{p}_\perp)A_j^e(q_\parallel,\boldsymbol{q}_\perp)\rangle\langle A_j^c(k_\parallel,\boldsymbol{k}_\perp)A_i^d(l_\parallel,\boldsymbol{l}_\perp)\rangle \tag{C.31}$$

$$= \underbrace{f^{abc}f^{ade}\delta^{be}\delta^{cd}}_{-N_c(N_c^2-1)}\frac{1}{(N_c^2-1)^2}\frac{1}{V^2}\int\frac{d^3\boldsymbol{p}}{(2\pi)^3}\frac{d^3\boldsymbol{q}}{(2\pi)^3}\frac{d^3\boldsymbol{k}}{(2\pi)^3}\frac{d^3\boldsymbol{l}}{(2\pi)^3}\,e^{i(\boldsymbol{p}+\boldsymbol{q}+\boldsymbol{k}+\boldsymbol{l})\cdot\boldsymbol{x}} \times(2\pi)^3\delta(p_\parallel+q_\parallel)\delta^2(\boldsymbol{p}_\perp+\boldsymbol{q}_\perp)(2\pi)^3\delta(k_\parallel+l_\parallel)\delta^2(\boldsymbol{k}_\perp+\boldsymbol{l}_\perp) \times\frac{4\pi^3}{p_\parallel^2}\phi(p_\parallel,\boldsymbol{p}_\perp)\frac{p_ip_j}{\boldsymbol{p}_\perp^2}\,\frac{4\pi^3}{k_\parallel^2}\phi(k_\parallel,\boldsymbol{k}_\perp)\frac{k_ik_j}{\boldsymbol{k}_\perp^2} \tag{C.32}$$

$$= -\frac{N_c}{(N_c^2-1)}\frac{1}{V^2}\int\frac{d^2p_T}{(2\pi)^2}\frac{d^2k_T}{(2\pi)^2}\frac{dp_\parallel}{(2\pi)}\frac{dk_\parallel}{(2\pi)} \times\frac{4\pi^3}{p_\parallel^2}\phi(p_\parallel,\boldsymbol{p}_\perp)\frac{p_ip_j}{\boldsymbol{p}_\perp^2}\,\frac{4\pi^3}{k_\parallel^2}\phi(k_\parallel,\boldsymbol{k}_\perp)\frac{k_ik_j}{\boldsymbol{k}_\perp^2}. \tag{C.33}$$

The third term in Eq. (C.24)

$$
\begin{aligned}
f^{abc}f^{ade}\langle A_i^b A_j^d\rangle\langle A_i^c A_j^e\rangle &= f^{abc}f^{ade}\int \frac{d^3\boldsymbol{p}}{(2\pi)^3}\frac{d^3\boldsymbol{q}}{(2\pi)^3}\frac{d^3\boldsymbol{k}}{(2\pi)^3}\frac{d^3\boldsymbol{l}}{(2\pi)^3}e^{i(\boldsymbol{p}+\boldsymbol{q}+\boldsymbol{k}+\boldsymbol{l})\cdot\boldsymbol{x}} \\
&\quad\times\langle A_i^b(p_\parallel,\boldsymbol{p}_\perp)A_j^d(q_\parallel,\boldsymbol{q}_\perp)\rangle\langle A_i^c(k_\parallel,\boldsymbol{k}_\perp)A_j^e(l_\parallel,\boldsymbol{l}_\perp)\rangle \qquad \text{(C.34)} \\
&= \underbrace{f^{abc}f^{ade}\delta^{bd}\delta^{ce}}_{N_\mathrm{c}(N_\mathrm{c}^2-1)}\frac{1}{(N_\mathrm{c}^2-1)^2}\frac{1}{V^2}\int \frac{d^3\boldsymbol{p}}{(2\pi)^3}\frac{d^3\boldsymbol{q}}{(2\pi)^3}\frac{d^3\boldsymbol{k}}{(2\pi)^3}\frac{d^3\boldsymbol{l}}{(2\pi)^3}\,e^{i(\boldsymbol{p}+\boldsymbol{q}+\boldsymbol{k}+\boldsymbol{l})\cdot\boldsymbol{x}} \\
&\quad\times(2\pi)^3\delta(p_\parallel+q_\parallel)\delta^2(\boldsymbol{p}_\perp+\boldsymbol{q}_\perp)(2\pi)^3\delta(k_\parallel+l_\parallel)\delta^2(\boldsymbol{k}_\perp+\boldsymbol{l}_\perp) \\
&\quad\times\frac{4\pi^3}{p_\parallel^2}\phi(p_\parallel,\boldsymbol{p}_\perp)\frac{p_ip_j}{\boldsymbol{p}_\perp^2}\,\frac{4\pi^3}{k_\parallel^2}\phi(k_\parallel,\boldsymbol{k}_\perp)\frac{k_ik_j}{\boldsymbol{k}_\perp^2} \qquad \text{(C.35)} \\
&= \frac{N_\mathrm{c}}{(N_\mathrm{c}^2-1)}\frac{1}{V^2}\int\frac{d^2\boldsymbol{p}_\perp}{(2\pi)^2}\frac{d^2\boldsymbol{k}_\perp}{(2\pi)^2}\frac{dp_\parallel}{(2\pi)}\frac{dk_\parallel}{(2\pi)} \\
&\quad\times\frac{4\pi^3}{p_\parallel^2}\phi(p_\parallel,\boldsymbol{p}_\perp)\frac{p_ip_j}{\boldsymbol{p}_\perp^2}\,\frac{4\pi^3}{k_\parallel^2}\phi(k_\parallel,\boldsymbol{k}_\perp)\frac{k_ik_j}{\boldsymbol{k}_\perp^2}. \qquad \text{(C.36)}
\end{aligned}
$$

Combining all these three, the energy density can be written as

$$
\begin{aligned}
\varepsilon(\tau=0) =& \frac{g^2}{2}\frac{N_\mathrm{c}}{(N_\mathrm{c}^2-1)}\frac{1}{V^2} \\
&\times\left[\int^{\Lambda_\mathrm{UV}}\frac{d^2\boldsymbol{p}_\perp}{(2\pi)^2}\frac{d^2\boldsymbol{k}_\perp}{(2\pi)^2}\frac{dp_\parallel}{(2\pi)}\frac{dk_\parallel}{(2\pi)}\frac{4\pi^3}{p_\parallel^2}\phi(p_\parallel,\boldsymbol{p}_\perp)\frac{4\pi^3}{k_\parallel^2}\phi(k_\parallel,\boldsymbol{k}_\perp)\right]. \qquad \text{(C.37)}
\end{aligned}
$$

The integrals over the transverse coordinates are divergent and they need to be cut off at the saturation scale $\Lambda_\mathrm{UV}\sim Q_\mathrm{s}$.

Appendix D

Derivation of the Integration Measure

Equation (4.13) is given as

$$\begin{aligned}\varepsilon(\tau=0) &= \frac{g^2}{2}\frac{N_{\rm c}}{(N_{\rm c}^2-1)}\frac{1}{V^2} \\ &\quad\times\int^{\Lambda_{\rm UV}}\frac{d^3\boldsymbol{p}}{(2\pi)^3}\frac{d^3\boldsymbol{q}}{(2\pi)^3}\frac{4\pi^3}{p_\parallel^2}\phi(x_1,\boldsymbol{p}_\perp^2)\frac{4\pi^3}{q_\parallel^2}\phi(x_2,\boldsymbol{q}_\perp^2).\end{aligned} \tag{D.1}$$

where $p_\parallel = mx_1$, $q_\parallel = mx_2$ and $\boldsymbol{p} = (p_\parallel, \boldsymbol{p}_\perp)$. By going from $(p_\parallel, q_\parallel)$ space to (x_1, x_2) space, we obtain

$$\begin{aligned}\varepsilon(\tau=0) &= \frac{g^2}{2}\frac{N_{\rm c}}{(N_{\rm c}^2-1)}\frac{1}{V^2}(4\pi^3)^2\int^{\Lambda_{\rm UV}}\frac{d^2\boldsymbol{p}_\perp}{(2\pi)^2}\frac{d^2\boldsymbol{q}_\perp}{(2\pi)^2} \\ &\quad\times\frac{1}{m^2}\int\frac{dx_1}{2\pi}\frac{dx_2}{2\pi}\frac{\phi(x_1,\boldsymbol{p}_\perp^2)}{x_1^2}\frac{\phi(x_2,\boldsymbol{q}_\perp^2)}{x_2^2}.\end{aligned} \tag{D.2}$$

A parallel can be drawn between Eq. (D.2) and Eq. (17.40) in [7]. Let us recall

$$x_{1,2} = \frac{m_{\rm T}}{\sqrt{s}}e^{\pm y}. \tag{D.3}$$

Note that Eq. (D.3) does not put any constraint on the two independent variables x_1 and x_2; Eq. (D.3) is merely a coordinate transformation to go from the parton momentum fraction space (x_1, x_2) to the transverse mass and rapidity space $(m_{\rm T}, y)$. The Jacobian of this coordinate transformation is $\partial(m_{\rm T}, y)/\partial(x_1, x_2) = s$, which yields

$$dx_1 dx_2 \to dm_{\rm T}^2 dy\,\frac{1}{s}. \tag{D.4}$$

Let us rewrite the energy in these new coordinates

$$\begin{aligned}\varepsilon(\tau=0) &= \frac{g^2}{2}\frac{N_{\rm c}}{(N_{\rm c}^2-1)}\frac{1}{V^2}(4\pi^3)^2\int^{\Lambda_{\rm UV}}\frac{d^2\boldsymbol{p}_\perp}{(2\pi)^2}\frac{d^2\boldsymbol{q}_\perp}{(2\pi)^2} \\ &\quad\times\frac{1}{m^2}\int\frac{dm_{\rm T}^2}{2\pi}\frac{dy}{2\pi}\frac{1}{s}\frac{\phi(x_1,\boldsymbol{p}_\perp^2)}{\left(\frac{m_{\rm T}}{\sqrt{s}}e^{y}\right)^2}\frac{\phi(x_2,\boldsymbol{q}_\perp^2)}{\left(\frac{m_{\rm T}}{\sqrt{s}}e^{-y}\right)^2} \qquad \text{(D.5)} \\ &= \frac{g^2}{2}\frac{N_{\rm c}}{(N_{\rm c}^2-1)}\frac{1}{V^2}(4\pi^3)^2\int^{\Lambda_{\rm UV}}\frac{d^2\boldsymbol{p}_\perp}{(2\pi)^2}\frac{d^2\boldsymbol{q}_\perp}{(2\pi)^2} \\ &\quad\times\frac{1}{m^2}\frac{1}{(2\pi)^2}\int dm_{\rm T}^2 dy\frac{s}{m_{\rm T}^4}\phi(x_1,\boldsymbol{p}_\perp^2)\phi(x_2,\boldsymbol{q}_\perp^2). \qquad \text{(D.6)}\end{aligned}$$

Let us put dy to the left hand side

$$\begin{aligned}\frac{d\varepsilon}{dy} &= \frac{g^2}{2}\frac{N_{\rm c}}{(N_{\rm c}^2-1)}\frac{1}{V^2}(4\pi^3)^2\int^{\Lambda_{\rm UV}}\frac{d^2\boldsymbol{p}_\perp}{(2\pi)^2}\frac{d^2\boldsymbol{q}_\perp}{(2\pi)^2} \\ &\quad\times\frac{1}{m^2}\frac{1}{(2\pi)^2}\int dm_{\rm T}^2\frac{s}{m_{\rm T}^4}\phi(x_1,\boldsymbol{p}_\perp^2)\phi(x_2,\boldsymbol{q}_\perp^2). \qquad \text{(D.7)}\end{aligned}$$

So far, no assumptions has been made. Now we shall assume that all the produced gluons have average momentum $\langle m_{\rm T}^2\rangle$ instead of integrating over $m_{\rm T}$ (Henceforth, $\langle m_{\rm T}\rangle$ instead of $m_{\rm T}$ has to be used with the definition of $x_{1,2}$ given in Eq. (D.3)). For that purpose, we add $\langle m_{\rm T}^2\rangle\delta(m_{\rm T}^2-\langle m_{\rm T}^2\rangle)$ to the integral in Eq. (D.7). We need the factor $\langle m_{\rm T}^2\rangle$ in addition to the delta function so that $\langle m_{\rm T}^2\rangle\delta(m_{\rm T}^2-\langle m_{\rm T}^2\rangle)$ is dimensionless. This average momentum assumption is to skip possible complications that may arise due to the $dm_{\rm T}^2$ integration. Finally, we obtain

$$\begin{aligned}\frac{d\varepsilon}{dy} &= \frac{g^2}{2}\frac{N_{\rm c}}{(N_{\rm c}^2-1)}\frac{1}{V^2}\frac{(4\pi^3)^2}{(2\pi)^2}\int^{\Lambda_{\rm UV}}\frac{d^2\boldsymbol{p}_\perp}{(2\pi)^2}\frac{d^2\boldsymbol{q}_\perp}{(2\pi)^2} \\ &\quad\times\frac{1}{m^2}\frac{s}{\langle m_{\rm T}\rangle^2}\phi(x_1,\boldsymbol{p}_\perp^2)\phi(x_2,\boldsymbol{q}_\perp^2). \qquad \text{(D.8)}\end{aligned}$$

Appendix E

Numerical Calculations

The UGD $\phi(x, \boldsymbol{p}_\perp)$ is given by

$$\phi(x, \boldsymbol{p}_\perp) = x \frac{dN}{dx d^2\boldsymbol{p}_\perp}. \tag{E.1}$$

An explicit form of $dN/dxd^2\boldsymbol{p}_\perp$ is given in Eq. (3.24). Multiplying it by x, we obtain

$$\begin{aligned} \phi(x, \boldsymbol{p}_\perp) &= x \frac{dN}{dx d^2\boldsymbol{p}_\perp}, \\ &= 3AC_{\rm F}\frac{2\alpha_{\rm s}}{\pi^2} \underbrace{\int d^2\boldsymbol{\Delta}_\perp}_{\int d\phi \int d\Delta_\perp \Delta_\perp} \underbrace{e^{i\boldsymbol{p}_\perp\cdot\boldsymbol{\Delta}_\perp}}_{\exp[ip_\perp\Delta_\perp\cos(\phi)]} \mathcal{L}(x;\boldsymbol{\Delta}_\perp)\mathcal{E}(v^2L(\boldsymbol{\Delta}_\perp)), \end{aligned} \tag{E.2}$$

where $C_{\rm F} = \frac{N_{\rm c}^2-1}{2N_{\rm c}}$, $p_\perp = |\boldsymbol{p}_\perp|$ and $\Delta_\perp = |\boldsymbol{\Delta}_\perp|$. Using

$$\int_0^{2\pi} d\phi \exp[ip_\perp\Delta_\perp\cos(\phi)] = 2\pi {\rm J}_0(p_\perp\Delta_\perp), \tag{E.3}$$

where ${\rm J}_0(p_\perp\Delta_\perp)$ is the Bessel function. Hence

$$\phi(x, \boldsymbol{p}_\perp) = 3AC_{\rm F}\frac{2\alpha_{\rm s}}{\pi^2}\int_0^\infty d\Delta_\perp\Delta_\perp 2\pi {\rm J}_0(p_\perp\Delta_\perp)\mathcal{L}(x;\Delta_\perp)\mathcal{E}(v^2L(\Delta_\perp)). \tag{E.4}$$

We repeat Eq. (D.8) here

$$\begin{aligned} \frac{d\varepsilon(\tau=0)}{dy} &= \frac{g^2}{2}\frac{N_{\rm c}}{(N_{\rm c}^2-1)}\frac{1}{V^2}\frac{(4\pi^3)^2}{(2\pi)^2}\left(\frac{\sqrt{s}}{\langle m_{\rm T}\rangle m}\right)^2 \\ &\quad \times \left[\underbrace{\int^{\Lambda_{\rm UV}} \frac{d^2\boldsymbol{p}_\perp}{(2\pi)^2}\phi(x_1,\boldsymbol{p}_\perp)}_{\mathcal{I}_+}\right]\left[\underbrace{\int^{\Lambda_{\rm UV}} \frac{d^2\boldsymbol{q}_\perp}{(2\pi)^2}\phi(x_2,\boldsymbol{q}_\perp)}_{\mathcal{I}_-}\right]. \end{aligned} \tag{E.5}$$

Let us compute the integral $\mathcal{I}_+$

$$\mathcal{I}_+ = \int^{\Lambda_{\rm UV}} \frac{d^2\boldsymbol{p}_\perp}{(2\pi)^2} \left[3AC_{\rm F}\frac{2\alpha_{\rm s}}{\pi^2}\int_0^\infty d\Delta_\perp \Delta_\perp 2\pi {\rm J}_0(p_\perp\Delta_\perp)\mathcal{L}(\underbrace{\frac{\langle m_{\rm T}\rangle}{\sqrt{s}}e^y}_{x_1};\Delta_\perp)\mathcal{E}(v^2L(\Delta_\perp)) \right]. \tag{E.6}$$

Considering

$$\begin{aligned} \int^{\Lambda_{\rm UV}} \frac{d^2\boldsymbol{p}_\perp}{(2\pi)^2} 2\pi {\rm J}_0(p_\perp\Delta_\perp) &= \int^{\Lambda_{\rm UV}} \frac{dp_\perp p_\perp 2\pi}{(2\pi)^2} 2\pi {\rm J}_0(p_\perp\Delta_\perp), & \text{(E.7)} \\ &= \frac{\Lambda_{\rm UV}}{\Delta_\perp}{\rm J}_1(\Lambda_{\rm UV}\Delta_\perp), & \text{(E.8)} \end{aligned}$$

we find

$$\begin{aligned} \mathcal{I}_+ &= 3AC_{\rm F}\frac{2\alpha_{\rm s}}{\pi^2}\int_0^\infty d\Delta_\perp\Delta_\perp \left(\frac{\Lambda_{\rm UV}}{\Delta_\perp}{\rm J}_1(\Lambda_{\rm UV}\Delta_\perp)\right) \\ &\quad \times\mathcal{L}(\frac{\langle m_{\rm T}\rangle}{\sqrt{s}}e^y;\Delta_\perp)\mathcal{E}(v^2L(\Delta_\perp)), & \text{(E.9)} \\ &= \int_0^\infty d\Delta_\perp 3AC_{\rm F}\frac{2\alpha_{\rm s}}{\pi^2}\Lambda_{\rm UV}{\rm J}_1(\Lambda_{\rm UV}\Delta_\perp)\mathcal{L}(\frac{\langle m_{\rm T}\rangle}{\sqrt{s}}e^y;\Delta_\perp)\mathcal{E}(v^2L(\Delta_\perp)). \end{aligned}$$

Hence, the energy density is given as

$$\begin{aligned} \frac{d\varepsilon(\tau=0)}{dy} &= \frac{g^2}{2}\frac{N_{\rm c}}{(N_{\rm c}^2-1)}\frac{1}{V^2}\frac{(4\pi^3)^2}{(2\pi)^2}\left(\frac{\sqrt{s}}{\langle m_{\rm T}\rangle m}\right)^2 & \text{(E.10)} \\ &\quad \times\left[\int_0^\infty d\Delta_\perp 3AC_{\rm F}\frac{2\alpha_{\rm s}}{\pi^2}\Lambda_{\rm UV}{\rm J}_1(\Lambda_{\rm UV}\Delta_\perp)\mathcal{L}(\frac{\langle m_{\rm T}\rangle}{\sqrt{s}}e^y;\Delta_\perp)\mathcal{E}(v^2L(\Delta_\perp))\right] \\ &\quad \times\left[\int_0^\infty d\Delta_\perp 3AC_{\rm F}\frac{2\alpha_{\rm s}}{\pi^2}\Lambda_{\rm UV}{\rm J}_1(\Lambda_{\rm UV}\Delta_\perp)\mathcal{L}(\frac{\langle m_{\rm T}\rangle}{\sqrt{s}}e^{-y};\Delta_\perp)\mathcal{E}(v^2L(\Delta_\perp))\right]. \end{aligned}$$

Using $g^2 = 4\pi\alpha_{\rm s}$ and $C_{\rm F} = N_{\rm c}^2 - 1/2N_{\rm c}$, we find

$$\begin{aligned} \frac{d\varepsilon(\tau=0)}{dy} &= \frac{4\pi\alpha_{\rm s}}{2}\frac{N_{\rm c}}{(N_{\rm c}^2-1)}\frac{1}{V^2}\frac{(4\pi^3)^2}{(2\pi)^2}\left(\frac{\sqrt{s}}{\langle m_{\rm T}\rangle m}\right)^2\left(3A\frac{N_{\rm c}^2-1}{2N_{\rm c}}\frac{2\alpha_{\rm s}}{\pi^2}\Lambda_{\rm UV}\right)^2 \\ &\quad \times\left[\int_0^\infty d\Delta_\perp {\rm J}_1(\Lambda_{\rm UV}\Delta_\perp)\mathcal{L}(\frac{\langle m_{\rm T}\rangle}{\sqrt{s}}e^y;\Delta_\perp)\mathcal{E}(v^2L(\Delta_\perp))\right] \\ &\quad \times\left[\int_0^\infty d\Delta_\perp {\rm J}_1(\Lambda_{\rm UV}\Delta_\perp)\mathcal{L}(\frac{\langle m_{\rm T}\rangle}{\sqrt{s}}e^{-y};\Delta_\perp)\mathcal{E}(v^2L(\Delta_\perp))\right]. & \text{(E.11)} \end{aligned}$$

Let us define

$$f[\Delta,\Lambda_{\rm UV},y,\langle m_{\rm T}\rangle,s,m,\lambda,A,\Lambda_{\rm QCD},\alpha_{\rm s}] \equiv {\rm J}_1(\Lambda_{\rm UV}\Delta)\mathcal{L}(\frac{\langle m_{\rm T}\rangle}{\sqrt{s}}e^y;\Delta)\mathcal{E}(v^2L(\Delta)). \tag{E.12}$$

Hence

$$\frac{d\varepsilon(\tau=0)}{dy} = \frac{4\pi\alpha_{\rm s}}{2}\frac{N_{\rm c}}{(N_{\rm c}^2-1)}\frac{1}{V^2}\frac{(4\pi^3)^2}{(2\pi)^2}\left(\frac{\sqrt{s}}{\langle m_{\rm T}\rangle m}\right)^2\left(3A\frac{N_{\rm c}^2-1}{2N_{\rm c}}\frac{2\alpha_{\rm s}}{\pi^2}\Lambda_{\rm UV}\right)^2 \times\left[\int_0^\infty d\Delta_1 f[\Delta_1,+y]\right]\left[\int_0^\infty d\Delta_2 f[\Delta_2,-y]\right]. \quad \text{(E.13)}$$

For a cylindrical nucleus, $V = h\pi R_A^2$

$$\frac{d\varepsilon(\tau=0)}{dy} = \frac{72A^2(N_{\rm c}^2-1)\,s\,\pi\alpha_{\rm s}^3\,\Lambda_{\rm UV}^2}{m^2N_{\rm c}\,\langle m_{\rm T}\rangle^2\,\underbrace{\pi^2h^2R_A^4}_{V^2}} \times\left[\int_0^\infty d\Delta_1 f[\Delta_1,+y]\right]\left[\int_0^\infty d\Delta_2 f[\Delta_2,-y]\right]. \quad \text{(E.14)}$$

In the numerical calculations, we shall use units such that $\hbar = c = 1$. The integrations $d\Delta_{1,2}$ are over distance $\Delta_\perp = |\boldsymbol{x}_\perp - \boldsymbol{x}'_\perp|$ and all distances including λ (the correlation length, intrinsic parameter of the 3dMVn) will be in units of fm. All the energy values shall be in units of fm^{-1}, where we use ($\hbar = c = 1$)

$$5.08 = \text{GeV}\cdot\text{fm}. \quad \text{(E.15)}$$

For example, the nucleon mass will be taken to be $m = 1\,\text{GeV} = 5.08\,\text{fm}^{-1}$. The final result of Eq. (E.38) will be in fm^{-4}. To convert this to GeV/fm^3, we need to multiply the final result with

$$\hbar c = 0.197\,\text{GeV}\cdot\text{fm}. \quad \text{(E.16)}$$

E.1 Interlude: Resurrecting $\hbar$ and c

If we recover $\hbar$ and c, the definitions change as follows.

Eq. (C.1) becomes

$$\underbrace{xg_A(x,Q^2)}_{\dim=0} = \int^{Q^2/c^2}\underbrace{\frac{d^2\boldsymbol{q}_\perp}{\hbar^2}}_{\dim=\text{fm}^{-2}}\underbrace{x\overbrace{\frac{dN}{dxd^2\boldsymbol{q}_\perp}}^{\phi(x,\boldsymbol{q}_\perp)}}_{\dim=\text{fm}^2}. \quad \text{(E.17)}$$

Also,

$$[\phi(x,\boldsymbol{q}_\perp)] = \left[x\frac{dN}{dxd^2\boldsymbol{q}_\perp}\right] = \text{fm}^2, \tag{E.18}$$

$$[\phi(q_\parallel,\boldsymbol{q}_\perp)] = \left[q_\parallel\frac{dN}{dq_\parallel d^2\boldsymbol{q}_\perp}\right] = \text{fm}^2. \tag{E.19}$$

The dimensions of the vector potential are ($\boldsymbol{q}=(q_\parallel,\boldsymbol{q}_\perp)$ and $\boldsymbol{x}=(x_\parallel,\boldsymbol{x}_\perp)$)

$$[A(\boldsymbol{x})] = \text{fm}^{-1} \text{ (see Eqs. (5.5) and (5.7) in [6])}, \tag{E.20}$$

$$[A(\boldsymbol{q})] = \text{fm}^2 \left(\text{from } A(\boldsymbol{q}) \propto \int d^3\boldsymbol{x}\, A(\boldsymbol{x})\right). \tag{E.21}$$

Then Eq. (C.5) becomes

$$\underbrace{\langle A_i^a(q_\parallel;\boldsymbol{q}_\perp)A_i^a(-q_\parallel;-\boldsymbol{q}_\perp)\rangle}_{\text{fm}^4} = \frac{4\pi^3}{m^2x}\frac{\hbar^2}{c^2}\frac{dN}{dxd^2\boldsymbol{q}_\perp} \tag{E.22}$$

$$= \frac{4\pi^3}{m^2x^2}\frac{\hbar^2}{c^2}\underbrace{x\frac{dN}{dxd^2\boldsymbol{q}_\perp}}_{\phi(x,\boldsymbol{q}_\perp)} \tag{E.23}$$

$$= \underbrace{\frac{4\pi^3}{m^2x^2}\frac{\hbar^2}{c^2}}_{\text{fm}^2}\underbrace{\phi(x,\boldsymbol{q}_\perp)}_{\text{fm}^2}, \tag{E.24}$$

or

$$\langle A_i^a(q_\parallel;\boldsymbol{q}_\perp)A_i^a(-q_\parallel;-\boldsymbol{q}_\perp)\rangle = \underbrace{\frac{4\pi^3}{q_\parallel^2}\hbar^2}_{\text{fm}^2}\underbrace{q_\parallel\frac{dN}{dq_\parallel d^2\boldsymbol{q}_\perp}}_{\phi(q_\parallel,\boldsymbol{q}_\perp)\quad\text{fm}^2}. \tag{E.25}$$

Also,

$$\delta^3(\boldsymbol{p}-\boldsymbol{q}) \Leftrightarrow \frac{V}{(2\pi)^3}\delta_{\boldsymbol{p},\boldsymbol{q}} \quad\longrightarrow \delta^3(\boldsymbol{p}-\boldsymbol{q}) \Leftrightarrow \frac{V}{(2\pi\hbar)^3}\delta_{\boldsymbol{p},\boldsymbol{q}}. \tag{E.26}$$

The ansatz in Eq. (C.23) becomes

$$\langle A_i^a(q_\parallel;\boldsymbol{q}_\perp)A_j^b(p_\parallel;p_\perp)\rangle_{1,2} = \frac{\delta^{ab}}{N_c^2-1}\underbrace{\frac{1}{V}}_{\text{fm}^{-3}}\underbrace{(2\pi\hbar)^3\delta(p_\parallel+q_\parallel)\delta^2(p_\perp+\boldsymbol{q}_\perp)}_{\text{fm}^3}$$
$$\times\underbrace{\frac{4\pi^3}{p_\parallel^2}\hbar^2\phi(p_\parallel,m_\mathrm{T})}_{\text{fm}^4}\frac{p_ip_j}{\boldsymbol{p}_\perp}. \tag{E.27}$$

and the momentum integrations pick up $\hbar$ and c as well

$$\int^{\Lambda_{\rm UV}} \frac{d^3\boldsymbol{p}}{(2\pi)^3} \to \int^{\Lambda_{\rm UV}/c} \frac{d^3\boldsymbol{p}}{(2\pi\hbar)^3}. \tag{E.28}$$

Substituting the ansatz in Eq. (E.27) in Eq. (C.24), the energy given in Eq. (C.37) becomes

$$\begin{aligned}\varepsilon(\tau=0) &= \frac{g^2}{2}\frac{N_{\rm c}}{(N_{\rm c}^2-1)}\frac{1}{V^2} \\ &\times\left[\int^{\Lambda_{\rm UV}/c}\frac{d^2\boldsymbol{p}_\perp}{(2\pi\hbar)^2}\frac{d^2\boldsymbol{k}_\perp}{(2\pi\hbar)^2}\frac{dp_\parallel}{(2\pi\hbar)}\frac{dk_\parallel}{(2\pi\hbar)}\frac{4\pi^3}{p_\parallel^2}\hbar^2\phi(x_1,\boldsymbol{p}_\perp)\frac{4\pi^3}{k_\parallel^2}\hbar^2\phi(x_2,\boldsymbol{k}_\perp)\right],\end{aligned} \tag{E.29}$$

where

$$p_\parallel = x_1 m/c = \frac{\langle m_{\rm T}\rangle m/c}{\sqrt{s}}e^y. \tag{E.30}$$

The energy per rapidity becomes (also see Eq. (D.8)

$$\begin{aligned}\frac{d\varepsilon}{dy} &= \frac{g^2}{2}\frac{N_{\rm c}}{(N_{\rm c}^2-1)}\frac{1}{V^2}\frac{(4\pi^3)^2}{(2\pi)^2}\int^{\Lambda_{\rm UV}}\frac{d^2\boldsymbol{p}_\perp}{(2\pi)^2}\frac{d^2\boldsymbol{q}_\perp}{(2\pi)^2} \\ &\times\frac{c^2}{\hbar^2}\frac{1}{m^2}\frac{s}{\langle m_{\rm T}\rangle^2}\phi(x_1,\boldsymbol{p}_\perp^2)\phi(x_2,\boldsymbol{q}_\perp^2).\end{aligned} \tag{E.31}$$

Or

$$\frac{d\varepsilon(\tau=0)}{dy} = \frac{g^2}{2}\frac{N_{\rm c}}{(N_{\rm c}^2-1)}\frac{1}{V^2}\left(\frac{4\pi^3}{2\pi}\right)^2\frac{c^2}{\hbar^2}\left(\frac{\sqrt{s}}{\langle m_{\rm T}\rangle m}\right)^2 \tag{E.32}$$

$$\times\underbrace{\int^{\Lambda_{\rm UV}/c}\frac{d^2\boldsymbol{p}_\perp}{(2\pi)^2}\phi(x_1,\boldsymbol{p}_\perp)}_{\mathcal{I}_+}\underbrace{\int^{\Lambda_{\rm UV}/c}\frac{d^2\boldsymbol{q}_\perp}{(2\pi)^2}\phi(x_2,\boldsymbol{q}_\perp)}_{\mathcal{I}_-}. \tag{E.33}$$

The UGD becomes

$$\phi(x,\boldsymbol{p}_\perp) = 3AC_{\rm F}\frac{2\alpha_{\rm s}}{\pi^2}\int_0^\infty d\Delta_\perp\Delta_\perp 2\pi {\rm J}_0(\frac{1}{\hbar}p_\perp\Delta_\perp)\mathcal{L}(x;\Delta_\perp)\mathcal{E}(v^2L(\Delta_\perp)), \tag{E.34}$$

and

$$\mathcal{I}_+ = \int^{\Lambda_{\rm UV}/c}\frac{d^2\boldsymbol{p}_\perp}{(2\pi)^2}\left[3AC_{\rm F}\frac{2\alpha_{\rm s}}{\pi^2}\int_0^\infty d\Delta_\perp\Delta_\perp 2\pi {\rm J}_0(\frac{1}{\hbar}p_\perp\Delta_\perp)\mathcal{L}(\underbrace{\frac{\langle m_{\rm T}\rangle c}{\sqrt{s}}e^y}_{x_1};\Delta_\perp)\mathcal{E}(v^2L(\Delta_\perp))\right]. \tag{E.35}$$

Using

$$\int^{\Lambda_{\rm UV}/c}\frac{d^2\boldsymbol{p}_\perp}{(2\pi)^2}2\pi {\rm J}_0(\frac{1}{\hbar}p_\perp\Delta_\perp)=\int^{\Lambda_{\rm UV}/c}\frac{dp_\perp p_\perp 2\pi}{(2\pi)^2}2\pi {\rm J}_0(\frac{1}{\hbar}p_\perp\Delta_\perp)=\frac{\hbar\Lambda_{\rm UV}}{\Delta_\perp c}{\rm J}_1(\Lambda_{\rm UV}\Delta_\perp), \tag{E.36}$$

we get

$$\begin{aligned}\mathcal{I}_+ &= 3AC_{\rm F}\frac{2\alpha_{\rm s}}{\pi^2}\int_0^\infty d\Delta_\perp\Delta_\perp\left(\frac{\hbar\Lambda_{\rm UV}}{\Delta_\perp c}{\rm J}_1(\frac{1}{\hbar}\Lambda_{\rm UV}\Delta_\perp)\right)\mathcal{L}(\frac{\langle m_{\rm T}\rangle c}{\sqrt{s}}e^y;\Delta_\perp)\mathcal{E}(v^2L(\Delta_\perp)),\\ &= \int_0^\infty d\Delta_\perp 3AC_{\rm F}\frac{2\alpha_{\rm s}}{\pi^2}\frac{\hbar}{c}\Lambda_{\rm UV}{\rm J}_1(\frac{1}{\hbar}\Lambda_{\rm UV}\Delta_\perp)\mathcal{L}(\frac{\langle m_{\rm T}\rangle c}{\sqrt{s}}e^y;\Delta_\perp)\mathcal{E}(v^2L(\Delta_\perp)).\end{aligned} \tag{E.37}$$

Plugging this into Eq. (E.33), we obtain

$$\begin{aligned}\frac{d\varepsilon(\tau=0)}{dy} &= \frac{g^2}{2}\frac{N_{\rm c}}{(N_{\rm c}^2-1)}\frac{1}{V^2}\left(\frac{4\pi^3}{2\pi}\right)^2\frac{c^2\!\!\!/}{\hbar^2}\left(\frac{\sqrt{s}}{\langle m_{\rm T}\rangle m}\right)^2\left(3A\frac{N_{\rm c}^2-1}{2N_{\rm c}}\frac{2\alpha_{\rm s}}{\pi^2}\right)^2\\ &\quad\times\int_0^\infty d\Delta_\perp 3AC_{\rm F}\frac{2\alpha_{\rm s}}{\pi^2}\frac{\hbar\!\!\!/}{c}\Lambda_{\rm UV}{\rm J}_1(\frac{1}{\hbar}\Lambda_{\rm UV}\Delta_\perp)\mathcal{L}(\frac{\langle m_{\rm T}\rangle c}{\sqrt{s}}e^y;\Delta_\perp)\mathcal{E}(v^2L(\Delta_\perp))\\ &\quad\times\int_0^\infty d\Delta_\perp 3AC_{\rm F}\frac{2\alpha_{\rm s}}{\pi^2}\frac{\hbar\!\!\!/}{c}\Lambda_{\rm UV}{\rm J}_1(\frac{1}{\hbar}\Lambda_{\rm UV}\Delta_\perp)\mathcal{L}(\frac{\langle m_{\rm T}\rangle c}{\sqrt{s}}e^{-y};\Delta_\perp)\mathcal{E}(v^2L(\Delta_\perp)).\end{aligned} \tag{E.38}$$

This is precisely the Eq. (E.11); so, no $\hbar$ and c appeared in the final result as expected.